Doctoral Dissertation
Doctoral Program in Electrical, Electronics and Communications Engineering
(XXXIII cycle)

Human exposure to low-frequency magnetic field: new methodologies for numerical dosimetry

Alice Conchin Gubernati

* * * * *

Supervisors
Prof. Fabio Freschi, Supervisor
Prof. Aldo Canova, Co-supervisor

Doctoral Examination Committee:
Ing. Emma Chiaramello, Referee, IEIIT CNR
Prof. Lionel Pichon, Referee, University of Paris Saclay
Prof. Luca Giaccone, Politecnico di Torino
Prof. Maurizio Repetto, Politecnico di Torino
Prof. Riccardo Scorretti, Université Lyon 1

Politecnico di Torino
May 8, 2022

I hereby declare that, the contents and organisation of this dissertation constitute my own original work and does not compromise in any way the rights of third parties, including those relating to the security of personal data.

. . . .
Alice Conchin Gubernati
Turin, May 8, 2022

Summary

Nowadays, human beings are inevitably exposed to electromagnetic fields due to the large diffusion of electric and electronic devices. When electromagnetic fields come into contact with human bodies, an interaction occurs and adverse health effects depending on the field intensity and the exposure time may happen.

In recent years the main world organizations, including the International Commission on Non-Ionizing Radiation Protection (ICNIRP) and the Institute of Electrical and Electronics Engineers (IEEE), which are involved in research regarding human exposure to electromagnetic fields, have defined guidelines and standards for human protection. These guidelines and standards are based on scientific studies carried out by researchers who, through numerical dosimetry, are able to perform numerical simulations and to evaluate the dosimetric quantities inside the human body. Threshold values are established to ensure a safe human exposure and a protection against the possible adverse effects that would arise in the exposed individual.

In this thesis the assessment of human exposure to low-frequency electromagnetic fields is taken into account. Some of the main problems related to the numerical dosimetry are discussed and different approaches are proposed.

A comparison between two different methods that allow to evaluate the magnetic vector potential starting from the knowledge of the magnetic flux density is described and the pros and cons of both methods are analyzing by solving a numerical dosimetry problem performed with virtual and real measurements.

Subsequently, shifting the attention to the voxelized realistic human models used in numerical simulations, the stair-casing approximation error due to the voxel-based discretization of these models is analyzed and tetrahedral models are introduced. The studies show that tetrahedral human models are able to eliminate numerical artifacts produced by stair-casing effects. However, other sources of computational artifacts are still present in real exposure scenarios and post-processing techniques are still needed.

Finally, the posturing problem related to human models is taken into account. Although the posture of the human body plays a fundamental role in numerical dosimetry problem, posture modeling takes a long time and some approximation errors are inevitably introduced. In this thesis, a new approach based on performing computations by using a non-postured human model is analyzed. The source term is modified through appropriate geometric transformations to avoid the posturing step in the numerical simulations.

Several numerical simulations on 2D and 3D domains are performed by using simplified phantom and realistic human body in order to validate the new approach. The potentiality of this new approach is highlighted and the possible applications are presented.

Acknowledgements

I would like to acknowledge the examination board members for their contribution in the improvement of the manuscript and for their time spent discussing my PhD work.

Vorrei ringraziare tutti i professori e colleghi del gruppo CADEMA per questi anni trascorsi insieme. In particolar modo vorrei ringraziare il Professor Aldo Canova per aver creduto in me e per avermi dato la possibilità di prendere parte a questa bellissima esperienza che mi ha permesso di crescere non solo intellettualmente, ma soprattutto umanamente.

Ringrazio il Professor Fabio Freschi per avermi trasmesso in questi anni la sua passione per la ricerca e per l'insegnamento, facendomi capire quale fosse la mia vera strada una volta terminato il mio dottorato. Ma lo ringrazio soprattutto per non avermi mai dovuto far scegliere tra lavoro e famiglia, per essere stato paziente e avermi lasciato mettere Alessandro sempre al primo posto, e per esserci sempre stato nei momenti belli e quelli un pochino più difficili.

Ringrazio il Professor Luca Giaccone per avermi insegnato l'ordine e il rigore da applicare non solo nel metodo scientifico ma soprattutto nella vita di tutti i giorni, per avermi fatto capire l'importanza del significato delle parole e che... una schermata nera sul computer non mi deve spaventare!

Un grazie speciale è dedicato a tutta la mia famiglia, senza la quale non potrei essere qui oggi a scrivere queste poche righe. Se questa mia tesi ha visto la luce è solo per merito vostro, per credere in me, per avermi spronato ad andare avanti quando mi sembrava impossibile farcela, per non avermi fatto mollare quando invece avrei voluto, per avermi sostenuto e aiutato nei momenti di sconforto, e soprattutto per avermi sopportato in questi ultimi mesi. Avevate ragione e ve ne sono davvero grata. A voi dedico questo mio lavoro!

Voglio ringraziare mia mamma e mio papà per l'amore che mi dimostrate in ogni istante, per esserci sempre, per il supporto e l'aiuto che da sempre mi date. Grazie per avermi insegnato i valori e i principi che porto sempre con me e che ora sto cercando di trasmettere ai miei figli: siete il mio punto di riferimento e la mia fonte d'ispirazione. Vi voglio un mondo di bene, non sapete quanto!

Voglio ringraziare Stefano per avermi supportato e sopportato tantissimo in questi mesi, per i sacrifici che anche tu hai dovuto fare per permettermi di arrivare fin qui. Grazie per credere in me più di quanto ci creda io stessa. Ma il grazie più grande che ti voglio dedicare è per la nuova famiglia che stiamo costruendo insieme: un nuovo capitolo

della nostra vita è iniziato circa due anni fa quando siamo diventati mamma e papà, e insieme stiamo cercando di scriverlo nel migliore dei modi, sbagliando e imparando dai nostri errori, sostenendoci a vicenda, ma ciò che è più importante è che lo stiamo facendo insieme.

Voglio ringraziare mia sorella per il legame profondo che ci lega, per il fatto che molte volte tra di noi non servono parole ma basta uno sguardo per capirsi, per i momenti che abbiamo condiviso, per il supporto reciproco che da sempre ci diamo e per i tuoi silenzi che spesso valgono più di mille parole.

E infine voglio ringraziare i miei due bambini, Alessandro e Amedeo, che con i suoi calcetti mi ha tenuto compagnia in questi mesi e non mi ha mai fatta sentire sola nelle lunghe notti di scrittura. Vedere la vita attraverso i tuoi occhi, Alessandro, mi ha fatto riscoprire la bellezza di tutto ciò che ci circonda e mi ha fatto capire quali siano le cose che realmente contano e per le quali vale la pena lottare. Siete la mia fonte di energia!

Alla mia famiglia, senza la quale non ce l’avrei mai fatta.
Ai miei due bambini, che mi hanno tenuto compagnia nelle ultime tappe di questo viaggio.

Contents

List of Tables

List of Figures

Chapter 1

Introduction

In recent years there has been an increase of the so-called phenomenon of electromagnetic pollution, caused by electric, magnetic and electromagnetic fields not generated by the natural terrestrial background or by the natural events such as the electric field due to the lightning.

Electromagnetic fields propagate in the space at light speed in a wavelike manner by producing electromagnetic radiation. They are classified in the electromagnetic spectrum according to their frequency or wavelength, through which electromagnetic radiation are divided into two categories: Ionizing Radiation (IR) and Non-Ionizing Radiation (NIR) [1]. They differ from each other due to their different ability to interact with materials atoms and molecules.

- Ionizing radiation is provided with an amount of energy capable of directly ionizing atoms and molecules. In this case, the term ionization refers to the process by removing electrons from atoms and molecules of materials that include air, water, and living tissue. Ionizing radiation can travel unseen and pass through these materials. The electromagnetic spectrum in Fig. 1.1 [2] shows that the electromagnetic waves with frequency higher than 3000 THz are include in IR, i.e. ultraviolet light, X-rays and gamma-rays. X-rays, for example, can penetrate our body and reveal pictures of our bones, because they have the unique capability to remove electrons from atoms and molecules in the matter through which they pass. However ionizing activity can alter molecules within the cells of our body and may cause eventual harm (such as cancer).

- Non-Ionizing Radiation is not able to ionize atoms and molecules. Depending on their frequency they are subdivided in Optical Radiation (300 GHz - 3000 THz) and Non-optical Radiation (0 Hz - 300 GHz). As Tab. 1.1 the Optical Radiation includes ultraviolet and visible light, and infrared radiations, while the Non-optical Radiation includes microwaves (MV), radio-frequency (RF), electric and magnetic field at low-frequency (LF), in turn divided into very-low frequency (VLF) and extremely low-frequency (ELF), and static electric and magnetic fields.

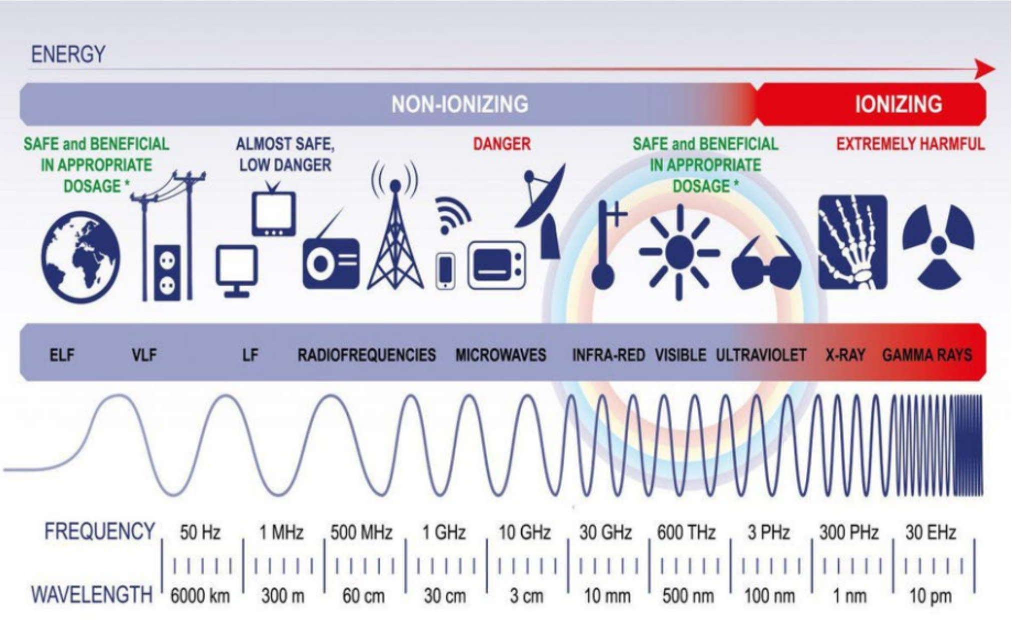

Figure 1.1: Electromagnetic field spectrum [2].

It is worth noting that the NIR subdivision suggested in [3], [4] and reported in Tab. 1.1 is only one of the possible subdivision: the different ranges into which the non-ionizing radiation can be divided depend on the context. In the classical literature the LF range is between 0.1 Hz and 300 kHz, while in the numerical dosimetry, the main topic of this thesis, the subdivision depends on the different effects caused by electromagnetic fields inside the human body. For example, the International Commission on Non-Ionizing Radiation Protection (ICNIRP), which is one of the international organizations responsible for giving indications on the risks concerning human exposure to non-ionizing electromagnetic fields, in [5] considers the LF range between 0 Hz and 100 kHz and according to [6] the RF and microwaves have frequency higher than 100 kHz. In our treatment we will follow this latter subdivision.

Several scientific studies on human exposure to ionizing and non-ionizing electromagnetic fields have been carried out in these years and the possible adverse effects on human health have been studied. In fact, as said before, when the electromagnetic fields come into contact with a biological system, they interact with it due to the electrical tissue conductivity. According to their intensity, these fields can cause different effects inside the human body.

An intense exposure to IR is not recommended because it is extremely harmful: it may produce, for example, skin or tissue damage. Instead, when the human body is exposed to NIR, two main effects (induced currents and heating of exposed tissues) have been detected, whose harmfulness depends on the intensity of the external field.

Low-frequency electromagnetic fields generate induced currents which interact with

Type	Subdivision	Name		Frequency range
Static field				0 Hz
NIR	Non-optical frequency	Low-frequency	ELF	0.1 Hz - 3 kHz
			VLF	3 kHz - 30 kHz
			LF	30 kHz - 300 kHz
		RF		300 kHz - 300 MHz
		MV		300 MHz - 300 GHz
	Optical frequency	Infrared Visible light Ultraviolet light		300 GHz - 3000 THz
IR		Ultraviolet light X-rays Gamma-rays		≥ 3000 THz

Table 1.1: Frequency range of electromagnetic field radiation.

the currents already present in the human body (e.g. the electric signals sent from the nervous system to the whole body to ensure the physiological activities), and stimulate the tissues whose cells are electrically excitable, such as muscle fibres or neurons. This can cause nerve and muscle stimulation, tingling in the skin, dizziness or nausea, or an annoying auditive perceptions of impulses.

On the other hand, when the frequency increases, the only substantiated effect of exposure relevant to human health and safety is heating of exposed tissue. It is caused by the rapid oscillatory movement of ions and water molecules that transforms the electromagnetic energy into the thermal one causing the heating in the tissues. In this case, the body can tolerate a small increase in heat, because it has a strong ability to regulate its internal temperature. However, above a certain level depending on the duration of exposure, RF electromagnetic fields can provoke serious health effects, such as heatstroke and tissue damage (burns).

All these effects fall into the category of short-term effects and they occur when a certain exposure threshold is exceeded. These effects are the more dangerous and evident the higher is the intensity of the electromagnetic field.

Potential health effects associated with long-term exposure have been extensively studied over the last few decades. It is widespread idea that long-term low-level exposure to 50 - 60 Hz magnetic fields might be associated with an increased risk of childhood leukemia, but the currently existing scientific evidence does not lead to this conclusion [7]. Evidence for cancer in adults from LF exposure is very weak [8]. At the same time there is no substantial scientific evidence for an association between LF exposure and Parkinson's disease, multiple sclerosis, developmental and reproductive effects, and cardiovascular diseases, as well as a relationship between RF exposure and headaches, concentration difficulty, sleep quality, cognitive function or cardiovascular effects [9].

About the risk of tumours in close proximity to the ear where the phone is held, e.g. brain tumours, several studies have not reported a relation between the use of mobile telephony and cancer [10]. This is an important consideration due to the widespread and significant increase in the use of mobile phones in the general population during the last few decades.

It can therefore be concluded that overall research on possible adverse effects deriving from long-term human exposure to LF and RF electromagnetic fields has not shown to date detrimental effects on health. However, many studies continue to be conducted.

Safety regulations that regulate human exposure to electromagnetic fields and define the restrictions to be respected to ensure a correct and safe exposure have been developed. In order to evaluate the risks deriving from human exposure to electromagnetic fields and to be able to define the respective guidelines, it is necessary to perform numerical simulations that give reliable results. This is the starting point of this thesis. In Chapter 2 an general overview about what is numerical dosimetry and why it is important is done. Dosimetric quantities are introduced and the guidelines and standards which guarantee a safe human exposure are described. The available realistic whole-body human models to be used in numerical simulations are described and the numerical artifacts related to the use of these models are analyzed together with the post-processing techniques to try to reduce them.

Subsequently, in Chapter 3 the importance of numerical simulations able to reproduce real exposure scenarios is underlined and the scalar potential finite difference (SPFD) method with its algebraic formulation is presented, formulation that will be used in this thesis to solve the numerical dosimetry problems of studied cases.

The research activities start from Chapter 4 in which the different methods able to evaluate the magnetic vector potential starting from the knowledge of the magnetic flux density are analyzed and a comparison between two numerical techniques for the evaluation of human exposure from measurement data is done. Through the analysis of test cases performed with virtual and real measurements, these methods are compared and the possibility of carrying out studies on human exposure starting from real measurements is highlighted.

Since in a numerical simulation not only an accurate modeling of the source is important, but also a human model which best reproduces the human shapes and the various tissues and organs of the human body is fundamental, in Chapter 5 the use of tetrahedral human models is proposed in order to eliminate the stair-casing approximation errors due to voxelized ones. Several exposure scenarios exposed to uniform and localized magnetic fields are analyzed starting from simplified models (e.g. a multilayered sphere) up to more complex ones (e.g. head human model).

Finally, in Chapter 6 a new approach which allows to perform numerical simulations by using a non-postured phantom is proposed. As it will be seen, in fact, the human model posture is important to ensure a correct human exposure evaluation to electromagnetic fields. However, the posturing activity is time-consuming and it always introduces approximation errors. This new approach allows to avoid the posturing step by applying specific geometric transformations to the source term. A human body transformations analysis is carried out and the Jacobian matrix is introduced. The approach reliability is validated through the analysis of test cases exposed to localized magnetic fields.

In Chapter 7 the contributions to numerical dosimetry deriving from the studies carried out in this thesis are highlighted.

Chapter 2

The importance of numerical dosimetry for limiting human exposure to low-frequency electromagnetic fields

In recent years, the growth in demand for electricity, the continuous advancement of technologies and the changes in social behaviour have increased the number of artificial sources and, consequently, also the human exposure to electromagnetic fields is increased. Being able to study the interaction between electromagnetic fields and human bodies has become important because of the need to know whether these electromagnetic fields have adverse effects on human health.

Electromagnetic dosimetry is the technical-scientific discipline that establishes the physical laws which govern the interactions between the electromagnetic fields and the human body. In particular, numerical dosimetry makes use of computational techniques to solve problems of human exposure to electromagnetic fields by means of numerical simulations.

In order to solve a numerical dosimetry problem it is important to be able to numerically reproduce a real exposure scenario. This means that it is necessary to have a model of the electromagnetic field sources that reproduces as much as possible the real one and a model of the human body exposed to that field which can be comparable to a real one.

2.1 Dosimetric quantities

Whenever an electromagnetic field interacts with a human body, an exchange of energy takes place, whose intensity and effects vary according to the field frequency and the exposure time. This interaction can be defined by four steps [11], which are described in Table 2.1.

Low-frequency electromagnetic fields generate induced currents inside the human

Step	**Description**
Exposure	A biological object is immersed in an electromagnetic field.
Matching	The electromagnetic field induces some physical phenomena, characterized by certain physical quantities (dosimetric quantities), in the tissues of the exposed body; these phenomena originate from the action of the field forces on the charges and electric currents present in the tissues.
Biological effect	The physical phenomena, induced by the electromagnetic field, cause some noticeable or detectable physiological change in a biological system which is not necessarily hazardous.
Adverse health effect	A biological effect does not necessarily constitute an adverse health effect; it becomes so if it is outside the normal range that the body is able to endure, becoming for this reason detrimental to health or well-being.

Table 2.1: Steps regarding the interaction between an electromagnetic field and a biological object (e.g. the human body).

body, whose intensity depends on the field one, while in high-frequency the main biological effect is the increase of tissues temperature (e.g. this effect is exploited by microwave ovens to heat food), as Tab. 2.2 shown. This heating can affect only a localized area of the human body or, at higher frequencies, it can cause a general increase in the body temperature. For this reason, in numerical dosimetry the quantities, called dosimetric quantities, that allow to study the phenomena that occur inside the human body during an interaction with an electromagnetic field, are extremely important.

The low-frequency dosimetric quantity was identified with the current density $\mathbf{J}$ ($\mathrm{A/m^2}$) (2004/40/EC) [12] until 2013, year in which the EU Directive 2013/35/EU [13] suggests to take the induced electric field $\mathbf{E}$ (V/m) as dosimetric quantity. The current density and the electric field are linked to each other by the constitutive equation

$$\mathbf{J} = \sigma \mathbf{E},$$

where σ is the electrical tissue conductivity.

The European Directive, which establishes the minimum health and safety requirements regarding the exposure of workers to electromagnetic fields, has recommended to take $\mathbf{E}$ as dosimetric quantity because the electrical tissues conductivity is determined with a very high level of uncertainty [14]. For this reason, since dosimetric quantities are used to establish the basic restrictions to ensure a safe human exposure, the use of $\mathbf{J}$ as

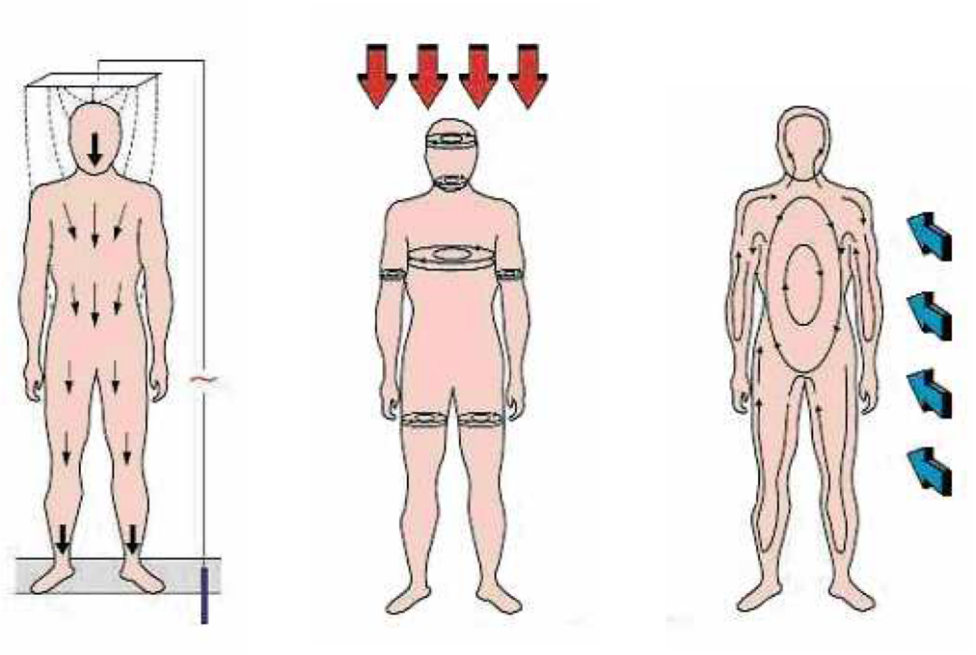

(a) Electric field. (b) Longitudinal magnetic field. (c) Frontal magnetic field.

Figure 2.1: Induced currents inside the human body generated by electric and magnetic fields.

dosimetric quantity is not recommended due to the uncertainties about σ.

As shown in Fig. 2.1 taken from [15], the currents induced inside the human body by the electric fields follow different paths from those induced by the magnetic fields. In the case of electric fields (Fig. 2.1a) the currents have the same direction as the electric field, while in the case of magnetic fields (Fig. 2.1b and Fig. 2.1c) they make circular trajectories on planes perpendicular to the direction of the magnetic field.

Otherwise, the high-frequency dosimetric quantity is the specific absorption rate (SAR), which measures the absorption of energy in the tissues.

It is worth pointing out that the dosimetric quantities are not directly measurable as it happens for external field values. For this reason, numerical dosimetry plays a fundamental role in the evaluation of the dosimetric quantities because, through numerical simulations, it is able to compute their values (with a certain degree of uncertainty) and it helps to define the human exposure thresholds.

Non-Ionizing Radiation						**Ionizing Radiation**		
Extremely Low Frequency	**Low Frequency**	**Radio Frequency**	**Microwaves**	**Infrared**	**VL**	**Ultra-violet**	**Soft X-ray**	**Hard X-ray/ Gamma Rays**
Power lines Hydro lines Computer terminals Electric appliance Telephones Mobile phones Cell phones	Navigation Computer terminals Pagers Mobile phones Cell phones	Radio/CB Television Computer terminals Mobile phones Pagers Cell phones	Radar Computer terminals Microwave ovens Mobile phones (@2.5 GHz) Cell phones	Sunlight Computer terminals		Sunlight Computer terminals	Medical X-rays Television Computer terminals	Nuclear fall out
Possible Health Effects Associated with Overexposure based on Scientific Studies								
Blood disorders Leukemia Cancer Cell growth Embryonic effect	CNS effects Immune System Cell Membrane effects	Cataracts Miscarriages Birth-defects Blood-disorders Embryonic effect CNS effects	Cataracts Miscarriages Birth-defects Genetic damage Birth defects CNS effects	Cataracts		Skin cancer Cataracts	Cancer Genetic damage Premature ageing	

Table 2.2: Scheme of the possible health effects associated with overexposure to electromagnetic fields.

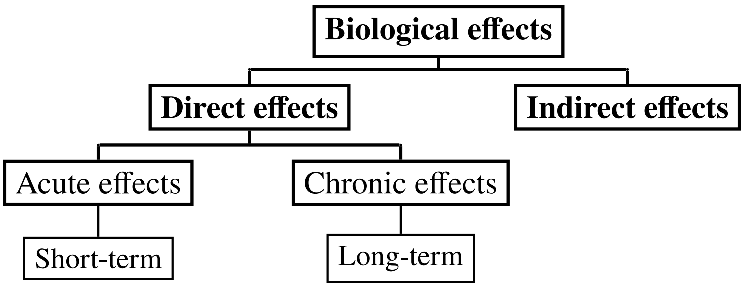

Figure 2.2: Scheme of classification of the possible biological effects deriving from human exposure to electromagnetic fields.

2.1.1 Health effects deriving from human exposure to low-frequency electromagnetic fields

Hereinafter, it is worth pointing out that when we will talk about numerical dosimetry, we will refer to low-frequency numerical dosimetry. Brief references to high-frequency electromagnetic fields will still be made, but without going into too much details.

Inside the human body there are, even in the absence of external electromagnetic fields, currents due to chemical reactions of the normal physiological functions: for example, the nervous system exchanges signals with the whole-body through electrical impulses, the heart is an electrically active muscle , and so on. We have seen that when a low-frequency electromagnetic field comes into contact with a human body, it generates induced currents inside it. These currents interact with the currents already inside the human body and, if sufficiently high, they can trigger the stimulation of nerves or muscles, or influence other biological processes. These effects depend on the external field intensity and they occur only when a certain threshold is exceeded: for example, when the induced currents reach an intensity comparable to the one of the currents already present in the human body, involuntary nerve impulses may appear. In fact, the nervous system is the main target of the low-frequency interaction and the effects vary from the perception of faint light flickering in the periphery of the visual field (called phospehenes) to cardio-vascular effects or tissue burn. Tab. 2.2 shows some possible effects in low- and high-frequency.

Generally, these effects disappear when the stimulation ceases and, therefore, also the external electromagnetic field disappears. For this reason these effects are called short-term effects and they are widely analyzed by the scientific community. Potential health effects associated with long-term low-level exposure have been extensively studied over the last few decades and no diseases caused by prolonged exposure have been discovered. However, many studies continue to be conducted.

It is worth highlighting that these biological effects become dangerous for human health only if a certain level of exposure is exceeded.

Finally, these effects can be direct, when the human body comes into direct contact with the electromagnetic field or indirect, when the human body comes into contact with an object on which an electromagnetic field acts.

The classification of the biological effects deriving from human exposure to electromagnetic fields is summarized in Fig. 2.2.

2.2 Guidelines and standards

Various national and international institution deal with the scientific research about radiation to ensure a safe human exposure to electromagnetic fields without adverse health effects. The world health organization (WHO) is the main organization responsible for studying the possible health risks and effects deriving from exposure to electromagnetic fields. In doing this it relies on the publications of other institutions such as the International Agency for Research on Carcer (IARC), which is specialized in cancer research, the National Radiological Protection Board (NRPB) and the Bundesamt für Strahlenschutz (BfS), which deal with research on radiological protection, the International Commission on Non-Ionizing Radiation Protection (ICNIRP), which develops and disseminates science-based advice on limiting exposure to non-ionizing radiation, and the Istituto Superiore della Sanità (ISS), which does health research in Italy. They are summarized in Fig. 2.3. This scheme can be read in two ways: vertically organizations belonging to different levels but dealing with the same research sector are presented; horizontally, institutions belonging to the same level but having different areas of competence are shown. We can see that in Italy the Consiglio Nazionale delle Ricerche (CNR) deals with national scientific research including the one related to low-frequency electromagnetic fields, while the rules related to electrical safety are issued by the Comitato Elettronico Italiano (CEI), who takes into account the international guidelines and standards. In fact, to ensure a safe human exposure to electromagnetic fields without having adverse health effects, each country establishes its own regulations based on international guidelines and standards.

Among the international organizations that are responsible for giving indications on the risks concerning human exposure to electromagnetic fields, the ICNIRP [6], [5] and the Institute of Electrical and Electronics Engineers (IEEE) [16], [17] are the most important. They have respectively defined guidelines and standards to be respected in order to protect both the population and the workers from the possible adverse health effects. They maintains close links and contacts with some scientific and technical institutions such as the International Electrotechnical Commission (IEC) and the European Electrotechnical Committee for Standardization (CELENEC), responsible for standardization in the area of electrical engineering at international and European level respectively.

Thanks to scientific studies, that are constantly updated, it is possible to define the thresholds below which human exposure to electromagnetic fields is safe. However, guidelines and standards do not use the limit values indicated in the scientific studies, but they apply to these values an additional reduction factor in order to be sure to guarantee a safe human exposure. Exceeding this limit does not automatically lead to an exposure

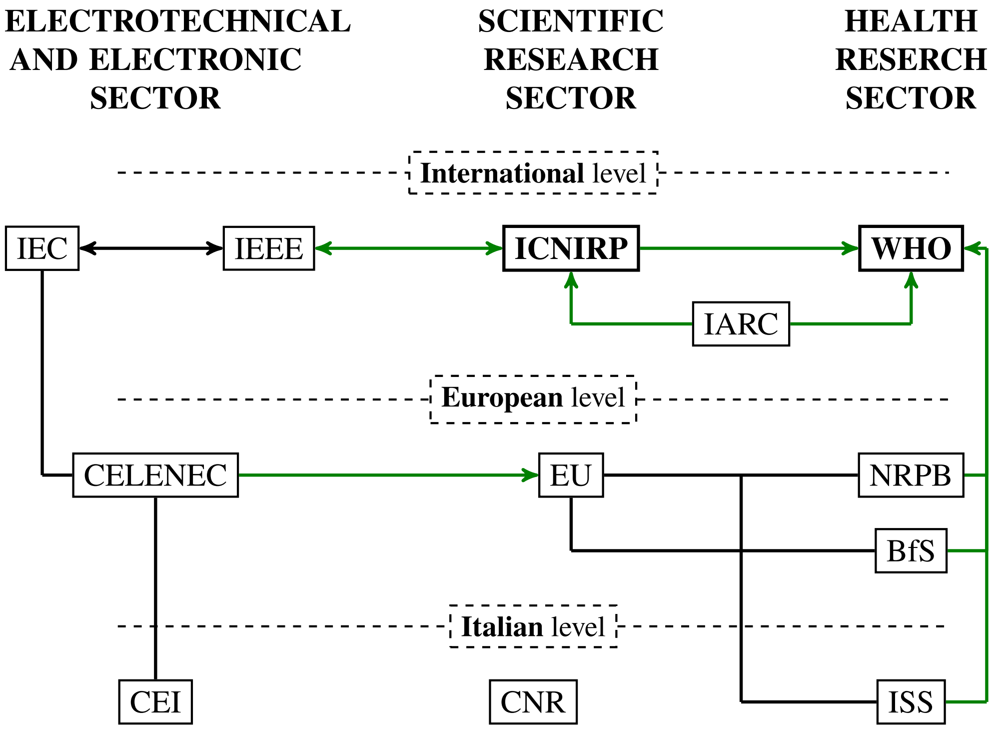

Figure 2.3: Scheme of national and international institutions that deal with scientific research about electromagnetic radiation. The black lines link together organizations that collaborate closely to each other, while the green lines indicate an indirect relationship based on the exchange of results and opinions. The arrows direction indicate the confluence of publications. The two-way arrows mean that the publications of the two institutions are comparable to each other.

with adverse health effects.

These limits vary depending on the context and on the reference guideline. Fig. 2.4a shows that IEEE standards have limit values different from those of the ICNIRP guidelines. The ICNIRP itself has different limit values if we compare the guidelines of 1998 (now dated) with those of 2010 (which will soon be updated). These differences are due to the evolution of scientific studies which, thanks to new technologies, are able to be more and more precise.

Fig. 2.4 shows that both the ICNIRP guidelines and the IEEE standards have different thresholds if they refer to the population (defined as public in the ICNIRP guidelines and as general in the IEEE standards) or to the workers (defined respectively as occupational and controlled). This is due to the fact that workers are usually exposed to electromagnetic fields under known conditions. On the contrary, the population is made up of individuals of all ages and different health states, and in many cases these people are unaware to be exposed to electromagnetic fields. For this reason the limits for the population are more stringent than those for workers. For example, the guidelines ensure that the level of

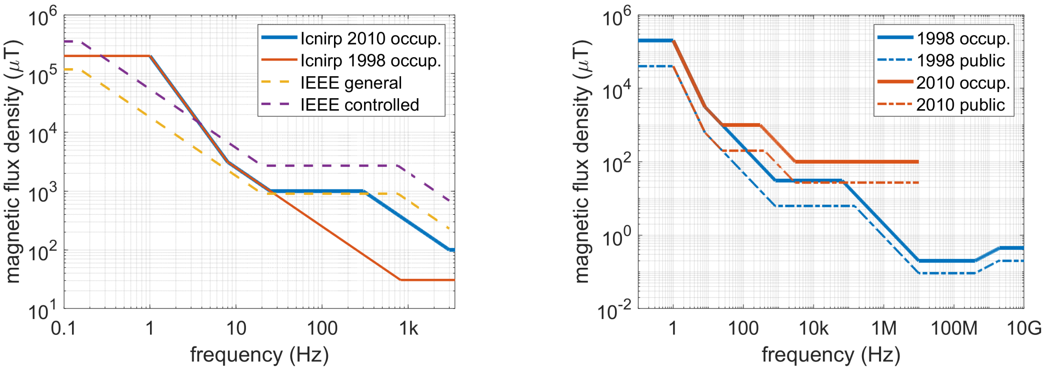

(a) (b)

Figure 2.4: Comparison between the limit values of ICNIRP guidelines and IEEE standards referring to workers (occupational and controlled), and of IEEE standards referring to the population (general) (a). Comparison between the limit values of ICNIRP guidelines of 1998 and 2010 referring both to workers (occupational) and population (public) (b).

the currents induced inside the human body exposed to a low-frequency electromagnetic field is below than the level of the electric currents already present in the human body.

However, as mentioned above, the guidelines do not comment on possible long-term health effects. Scientific studies have shown a lack of correlation between prolonged human exposure to electromagnetic fields and the onset of long-term effects, such as cancer, but a large number of studies are still carried out.

Finally, a specific European Directive for the protection of workers in an occupational exposure context exists [13].

Since the ICNIRP guidelines are perceived by all the European Union member states, including Italy, and national regulations are based on them, in the next paragraph the difference between the basic restrictions and the reference levels described in these guidelines is analyzed. It is worth underlying that the IEEE's equivalent terms for these limits are respectively dosimetric reference limits and exposure reference levels.

2.2.1 Basic restrictions and reference levels

To prevent adverse health effects deriving from the interactions between human bodies and external electric and magnetic fields, the guidelines establish some exposure limits. These limits refer both to the dosimetric quantities and to the external field values, and they are respectively called basic restrictions and reference levels.

The basic restrictions are limits for personal protection, which specify the maximum exposure allowed in the whole body or in parts of the body with respect to the emissions from field generated by devices and systems. They are based on proven biological effects and they are related to the threshold showing adverse effects with an additional reduction factor in order to consider scientific uncertainties pertaining to the determination of that threshold. Since they refer to the dosimetric quantities inside the human body, they are difficult to be directly evaluated.

The reference levels refer to the exposure limits outside the body and they are derived from the basic restrictions using the worst-case exposure assumption. They ensure compliance with the recommended basic restrictions. Unlike the latter, they can be verified by direct measurements and/or by computational methods. However, if a measured value exceeds the reference level, it does not necessarily mean that the basic restriction is exceeded. By computer simulations it is possible to evaluate the dosimetric quantity and to verify if its values are in compliance with the basic restriction. This can happen in localized exposure because the ICNIRP guidelines define the reference levels considering a human body exposed to a uniform field. In these cases the compliance with the local basic restriction should be directly assessed [18].

Table 2.3 shows the physical quantities used to specify the basic restrictions and the reference levels at the different electromagnetic field frequencies.

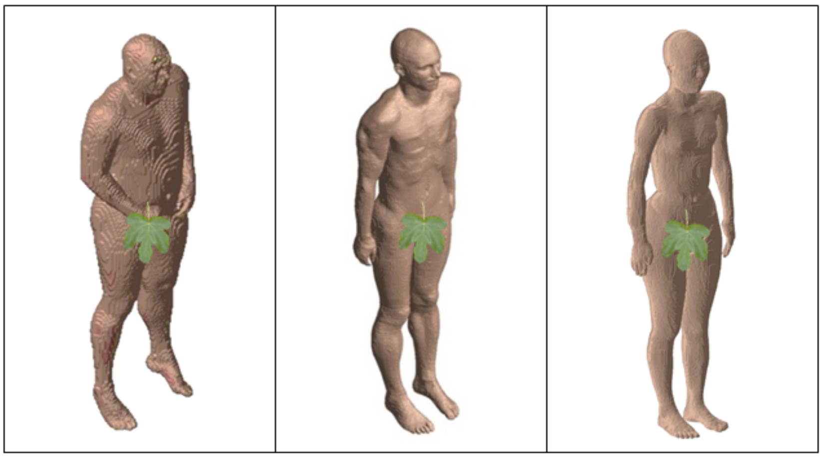

Figure 2.5: Example of voxelized realistic whole-body human models. From left to right there are Visible Human Male, Duke and Hanako

2.3 Human models

In order to evaluate human exposure to electromagnetic fields by solving a numerical dosimetry problem, a model of the human body on which to perform numerical simulations is required. Depending on the type of problem to solve and the degree of precision to achieve, simplified human models or realistic whole-body human models can be used.

Simplified human models do not reproduce anatomical human shape in details and they are usually used in numerical simulations as homogeneous models (i.e. they are

Frequency	**Basic restrictions**	**Reference levels**
0 Hz - 1 Hz	Magnetic flux density (T) Current density (A/m^2)	Magnetic flux density (T) Magnetic field strength (A/m)
protection goal:	to avoid effects on the cardiovascular and nervous system.	
1 Hz - 10 MHz	Current density (A/m^2) Internal electric field (V/m) SAR (W/kg)	Magnetic flux density (T) Electric field strength (V/m) Magnetic field strength (A/m)
protection goal:	to avoid effects on nervous system functions, whole-body heat stress, and excessive localized heating of tissues.	
10 MHz - 10 GHz	SAR (W/kg)	Magnetic flux density (T) Electric field strength (V/m) Magnetic field strength (A/m) Power density (W/m^2)
protection goal:	to avoid whole-body heat stress and excessive localized heating of tissues.	
10 GHz - 300 GHz	Power density (W/m^2)	Magnetic flux density (T) Electric field strength (V/m) Magnetic field strength (A/m) Power density (W/m^2)
protection goal:	to avoid heating in tissue at or near the body surface.	

Table 2.3: Physical quantities used in the ICNIRP basic restrictions and reference levels depending on the frequency (from 0 Hz (static fields) to 300 GHz (RF)). The respective protection goals are highlighted.

constituted by a single tissue), when it is not required to study what happens in each single tissue, but the global vision of the dosimetry problem is important. They also require less computation time than the realistic human models because they consist of fewer elements. Among the simplified models we can mention the disk and the homogeneous axial-symmetric human model, which are also adopted in some standards [19], [20].

Nowadays several realistic whole-body human models are available to perform numerical simulations for the evaluation of human exposure to electromagnetic fields. Human body has a very complex internal structure and the outer surfaces of most organs are very complicated to reproduce. In the last few years, the rapid advancement of technologies and the increase in the computational capabilities of the machines have allowed the development of realistic anatomical whole-body human models of different age, gender, size and height to be used in numerical simulations. Most of these models were created starting from computed tomography (CT) scans or magnetic resonance images (MRI) of patients, volunteers or cadavers. Thanks to the increased use of the medical imaging technologies, high-resolution cross-sectional digital images of internal anatomy are provided. These data can be used to create a three-dimensional digital representation of the shape, volume and composition of human organs. Starting from the two-dimensional pixel data of such images and extending them into the third dimension by extruding them along z-axis, in fact, a voxel-based discretization is obtained. A voxel is the three-dimensional counterpart of the two-dimensional pixel and has the shape of a cube (regular hexahedron). An ID number, that represents the name of the tissue or the organ to which it belongs, is assigned to each voxel and the biological properties of the respective tissue/organ are attributed. Several studies are carried out to continue to improve the tissue material parameter values, which have a degree of uncertainty because they can be measured only numerically. The most famous material parameter database continuously updated which contains information about the biological tissue properties is the IT'IS Foundation Database [14].

In this way the virtual anatomical whole-body model reproduces the real one as likely as possible and it can be used in the numerical simulations to measure the dosimetric quantities and to see if the basic restrictions are respected. The presence of different tissues, in fact, allows the researchers to perform realistic simulations of what happens inside human body in a real exposure scenario, such as the tissue contrast effect caused by the currents that pass through tissues with very different electrical conductivities.

The first human models discretized with voxels were unable to accurately reproduce the smoothness of tissues boundaries due to the too large voxel dimensions. The increase of the images resolution together with the more sophisticated reconstruction techniques has allowed to improve the meshes discretization, managing to obtain models with $0.5 \times 0.5 \times 0.5$ mm^3 voxel dimensions. However, if on one side the domain resolution and discretization have improved, on the other the number of voxels and, consequently, of unknowns to be solved in numerical problems has considerably increased. For this reason the models with $2 \times 2 \times 2$ mm^3 or $1 \times 1 \times 1$ mm^3 voxel discretization can be considered a good compromise between discretization and computational cost.

Among the whole-body anatomical realistic human models used in the scientific studies of human exposure to electromagnetic fields, the IT'IS Foundation has developed different models of different age, gender, size and height [21], [22], like Duke, a 34-years-old male, Ella, a 26-years-old female, and Billie and Thelonius, an 11-years-old girl and a 6-years-old boy respectively. Others available models are those built from the data of the Virtual Human Project [23], [24] and the Japan's whole-body human models (Taro and Hanako) developed by the National Institute of Information and Communications Technology (NICT) (see Tab. 2.4).

Since these voxel-based human models are constructed from cadavers, volunteers and patients CT scans or MRI images, they are arranged to stand on the ground or lie on an experimental table with their arms along their sides. These two positions limit the research activities since in the simulation of a realistic scenario the posture must be taken into account.

Some postured voxel-based models started to be developed from the upright-posture

Organization (Phantom name)	Sex	Height (cm)	Weight (kg)	Voxel size (mm)
NICT (TARO)	M	173.2	65	$2\times2\times2$
NICT (HANAKO)	F	160.8	53	$2\times2\times2$
HPA (NORMAN)	M	176.0	73	$2\times2\times2$
HPA (NAOMI)	F	163.0	60	$2\times2\times2$
ITIS (ELLA)	F	160.0	58	CAD MESH (arbitrary)
ITIS (DUKE)	M	174.0	70	CAD MESH (arbitrary)
ITIS (BILLIE)	F	148.0	34	CAD MESH (arbitrary)
ITIS (THELONIUS)	M	106.0	17	CAD MESH (arbitrary)

Table 2.4: Some characteristics of the main whole-body human models used in numerical dosimetry problems.

models. Among them there are the sitting human models developed by [25], [26], [27], [28], [29], the deformed human model with outstretched or forward stretched arms developed by [25], [30], [28], and the deformed human models with several different postures developed by [31]. At the same time, posturing software have been created, even if posturing a human model through a software is a cumbersome task both for time-consuming and the difficulty with which these models can be exported and then used in other software.

The importance of posture in numerical simulations of human exposure is one of the topics covered in this thesis and it will be analyzed in chapter 6, where a new approach to avoid the posturing step will be proposed.

At the same time, in this thesis, some shortcomings of the voxel-based human models will be analyzed and some alternatives will be proposed. Among these, we can underline:

- the voxel are not able to reproduce carefully smooth surfaces and this causes numerical artifacts, such as stair-casing errors (as we will see in Chapter 5);
- voxelized models are created using MRI images of patient, volunteers or cadavers, but the internal anatomy of an individual can differ from that of another individual with similar size; moreover, the internal structures of the human body having dimensions less than the dimensions of the voxel cannot be accurately segmented (e.g. the skin thickness [32]).

2.4 Numerical artifacts

When numerical simulations are performed, attention must be paid to numerical artifacts. In numerical dosimetry the raw solution is subject to these artifacts coming from different sources [33]. In low-frequency dosimetry, these artifacts may include

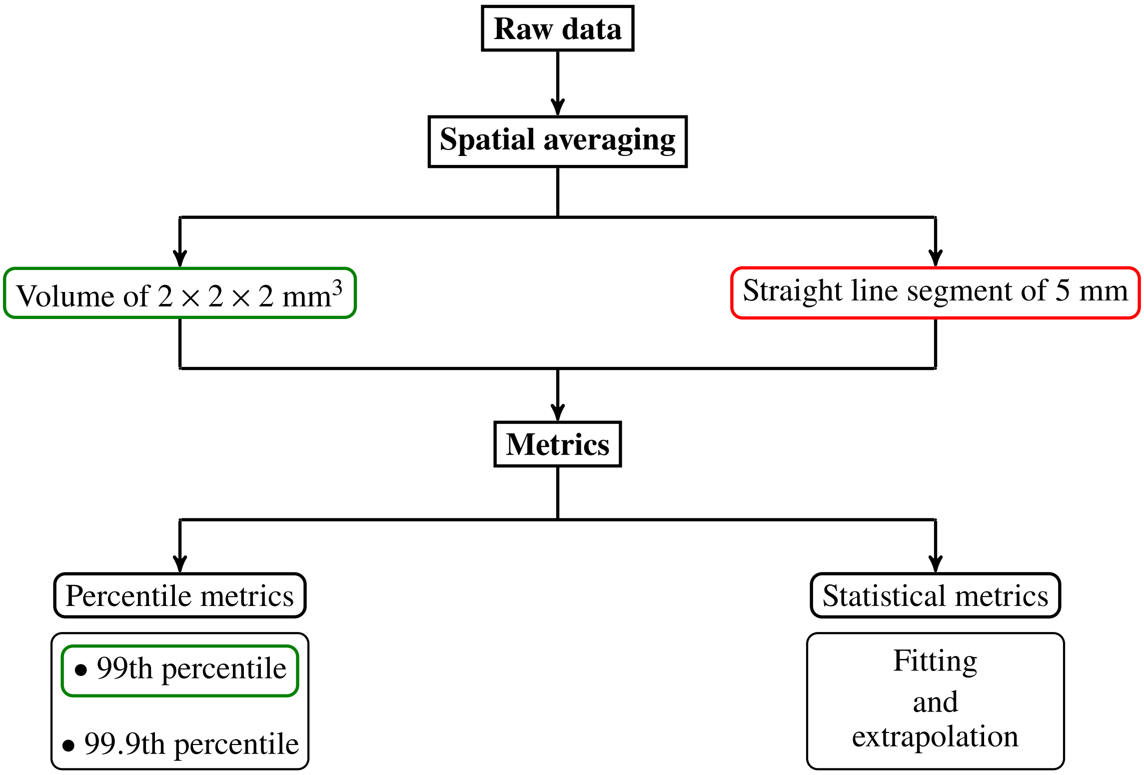

Figure 2.6: Scheme of different ways to reduce numerical artifacts. The ICNIRP approach is highlighted in green, while the IEEE one in red. The statistical metrics correspond to the method proposed by [36] and then improved by [37].

- segmentation error in an anatomical model, which may include the quality of medical images acquired in millimeter resolution [34];
- discretization error in modelling tissue, especially when the tissues have dimensions less than the grid resolution [32];
- computational errors themselves [35].

In Chapter 5 we will analyzed one of them, i.e the stair-casing approximation error typical of the voxelized human models and due to the attempt to reproduce the curved boundaries of tissues and organs with cubic elements.

Numerical artifacts cause an overestimation of the exposure and therefore must be filtered out with suitable methods proposed in standards, guidelines, and literature [6], [5], [16] and [17].

2.4.1 Post-processing methods to eliminate numerical artifacts

Because of these numerical artifacts, the maximum value in each tissue of the raw solution overestimates the real exposure. If the raw solution is compared with the basic restrictions without being filtered out, the maximum electric field value in each tissue can exceed the threshold imposed by the basic restrictions to ensure a safe human exposure. However these maximum values do not represent the real values due to the exposure because they are subject to numerical artifacts. For this reason post-processing techniques are required. Fig. 2.6 shows all the post-processing techniques that can be used and we are going to analyze below.

In order to filter out the raw solution, ICNIRP guidelines [5] and IEEE standards [16], [17] propose two different post-processing methods based on carrying out a spatially averaging of the *in situ* electric field: the first method prescribes a cubic averaging scheme over $2 \times 2 \times 2$ mm^3 volume, the second one a linear averaging over a 0.5 cm line.

In particular, ICNIRP recommends "determining the induced electric field as a vector average of the electric field in a small contiguous tissue volume of $2 \times 2 \times 2$ mm^3". However, several studies have shown that the maximum electric field value of each tissue obtained after this spatially averaging is still subject to computational artifacts. For this reason the ICNIRP suggests to compare with the basic restrictions the 99th percentile value and not the maximum one. Considering the 99th percentile as the electric field value to be compared with the basic restrictions means considering that electric field value for which the 99% of the voxels are characterized by a electric field value lower than the 99th percentile. All values above the 99th percentile are rejected because they are still subject to computational artifacts.

For IEEE, instead, "the basic restrictions on the *in situ* electric field apply to an arithmetic average determined over a straight line segment of 0.5 cm length oriented in any direction within the tissue".

Recent scientific studies have shown that these two methods have some limits. First of all neither approach explains how to deal with voxel that have one or more edges or faces in common with other tissues or air, in which spatially averaging would include two different electrical conductivities. Because it is not specified, two different ways can be used: 1) doing the spatially averaging by using all voxels inside the $2 \times 2 \times 2$ mm^3 volume or along the 0.5 cm line segment, or 2) giving weight 0 to the voxels with a different tissue respect to the one of the voxel considered and then doing the spatially averaging in order to not include different electrical conductivities. A recent study [33] has investigated this issue and it has found that there is a maximum percentage of air/tissue that can be included in the averaging without affecting the results.

At the same time the 99th percentile proposed by the ICNIRP guidelines is acceptable when the magnetic field is uniform across a tissue situated within a confined volume (e.g. heart, liver, kidney) [38]. However, in a localized exposure with a strong gradient it underestimates the exact induced electric field value especially in the distributed tissues (e.g. skin, fat, peripheral nerve) [36].

Regarding to the IEEE approach, no metrics are introduced in order to further filter out the solution. It is assumed that the orientation of the straight line in "any direction" ensures that the electric field values obtained after the linear averaging are free of numerical artifacts. The main problem of this approach is the high computational cost due to line orientation in any directions. Some scientific studies [39], [40] suggest to use the line direction parallel to the one of the induced electric field of the voxel under examination in order to try to reduce the computational cost.

Recently several studies have been conducted on the limits of the post-processing techniques proposed by the ICNIRP and IEEE and some alternatives to try to solve them have been analyzed. In [36] and [41] pre-processing and post-processing methods to reduce numerical artifacts are proposed. The pre-processing method consists of making the electrical conductivity smoother in order to reduce the contrast between neighbouring tissues; the post-processing method suggests to compare the 99.9th percentile with the basic restrictions in the localized exposures. In [35], the authors not only confirm that the 99th percentile underestimates the real exposure values, but they even suggest to use the 99.99th percentile.

It is clear that if on one side all the recent studies agree in declaring that the 99th percentile proposed by the ICNIRP tends to underestimate the real induced electric field values in localized exposures, on the other the choice of which percentile higher than the 99th one has to be used is completely arbitrary and it depends on the exposure scenario. To address this arbitrariness, a post-processing method based on the elimination of the outliers on statistical basis have been developed [36]. In this method the magnitude of the induced electric field values is sort in ascending order despite their spatial distribution. The "gradient", evaluated as the difference between two adjacent values divide by their mean, of the last percentile of the sorted values is then evaluated. The frequency distribution of the logarithm of the gradient is plotted and, if its shape is symmetric and with one local maximum only, the detection point (DP) of the outliers is determined by adding to the mean of the distribution a positive shift, corresponding to three times the standard deviation. So the detection point represent the point after which the numerical artifacts arise and it varies from simulation to simulation because it depends on the induced electric field values distribution calculated in that specific scenario. Once the detection point is evaluated, [36] proposed to fit the no outliers induced electric field sorted values with a polynomial function of order 2 and replacing the outliers with the extrapolation of this trend. However, a discontinuity in the DP between the replaced values and the ones that do not undergo the correction may occur. This discontinuity does not cause any particular problems, but it could continue to underestimate the exact values. To avoid this discontinuity, [37] improves this method by suggesting that the interpolating polynomial is extrapolated on a number of points previous the DP equal to the number of the outliers to be corrected.

Summarizing what has been said, the post-processing methods used in numerical dosimetry studies to reduce numerical artifacts can be related to the percentile use or they can base on statistical studies to find the outliers. It is worth to underline that these metrics can be directly applied to the raw solution, without the spatially averaging need, especially when a $2 \times 2 \times 2$ mm^3 discretized models is used.

Chapter 3

Algebraic formulation of low-frequency numerical dosimetry methods for the evaluation of human exposure

In the previous chapter, we have seen that when a measured field value exceeds a reference level, the human exposure in that realistic scenario does not necessarily produce adverse health effects. In fact, the basic restrictions defined on the dosimetric quantities can still be satisfied. However, as previously said, these quantities are not directly measurable and they can be computed only through numerical simulations that reproduce the real scenario as faithfully as possible. In this chapter, the mathematical process leading to the algebraic formulation of the scalar potential finite difference method is described and the relation between the differential and topological operators is analyzed.

3.1 A general mathematical overview

In standard mathematical approaches, physical laws are described by partial differential equations (PDEs) which involves the use of local variables, i.e. point-wise scalar or vector quantities. However, rarely an exact solution to the problem is obtained by solving partial differential equation systems: in fact, the variables which describe a physical problem are integral quantities and not local ones treated by differential operators. To solve these physical problems, the partial differential equations have to be numerically integrated in order to obtain an algebraic system of equations. For this reason several numerical methods have been developed, like for example FEM (Finite Element Method), FDM (Finite Difference Method)or BEM (Boundary Element Method), which always allow to compute an approximate solution. Most of these numerical methods are based on the discretization of the domain through the creation of a mesh, which in the three-dimensional case is usually composed of hexahedra or tetrahedra.

However, thanks to the theory developed by Tonti [42], the domain discretization

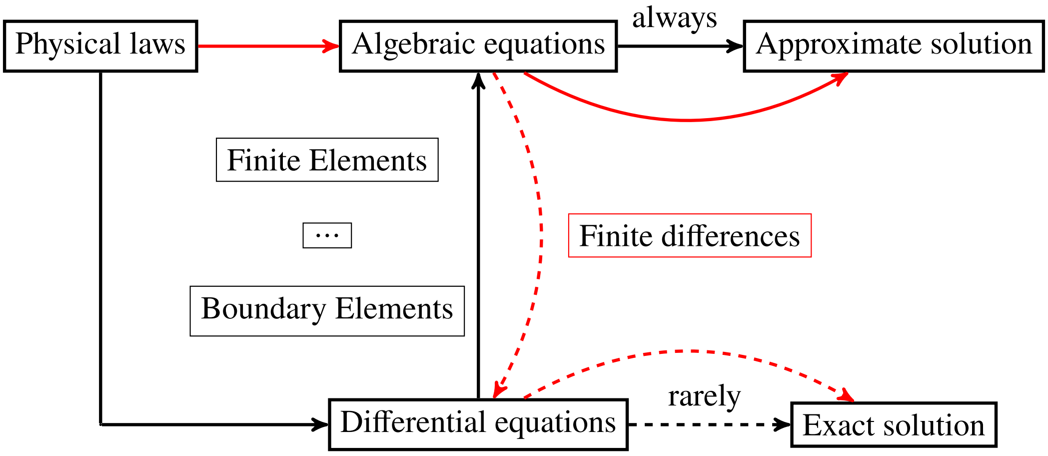

Figure 3.1: Representation of the possible paths to find the numerical solution of physical problems: the black arrows show the classical approach, while the red ones the cell method approach.

allows to analyze the equations which governs these physical problems directly in their algebraic formulation and in terms of global variables, i.e. quantities associated to a space and/or time entity. The algebraic formulation, in fact, links the physical quantities to the elements of the mesh. The framework provided by Tonti diagrams for the description of physical laws can be directly translated into a numerical procedure which is used by the cell method (CM) to obtain an approximate solution directly to the algebraic equations.

3.1.1 The cell method

The cell method is a numerical method based on the direct finite formulation of physical equations [43]. The method allows to directly write in algebraic form the system of equations capable of providing the approximate solution of the studied problem, without using the partial differential equations, as Fig. 3.1.

One fundamental aspect of the CM is the tessellation of space (and time, depending on the specific implementation), called cell complex. The cell complexes are characterized by the presence of a pair of intertwined grids [44]: the primal mesh made by generic polygons (usually triangles or quadrilaterals) or polyhedra (usually tetrahedra or hexahedra) depending on considering a two-dimensional or three-dimensional space respectively, and a secondary dual grid obtained from the primal one using a barycentric subdivision [45]. Since in this thesis we work on three-dimensional space, we focus our discussion on it.

Each polyhedron is made of connected elements of different dimensions: nodes (0-cell), edges (1-cell), faces (2-cell) and volumes (3-cell) (see Fig. 3.2). Each element of the primal structure is one-to-one associated to an element of the dual grid: if N, E, F and V are respectively the nodes, edges, faces and volumes of the primal mesh and $\tilde{N}$, $\tilde{E}$,

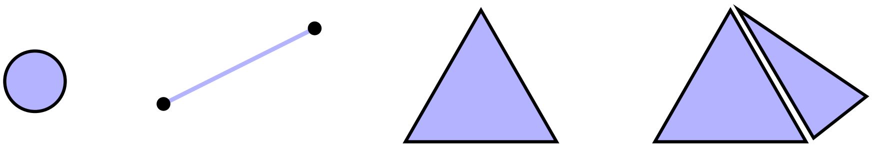

(a) 0-cell (b) 1-cell (c) 2-cell (d) 3-cell

Figure 3.2: Elements of different dimensions: nodes (0-cell) (a), edges (1-cell) (b), faces (2-cell) (c), and volumes (3-cell) (d).

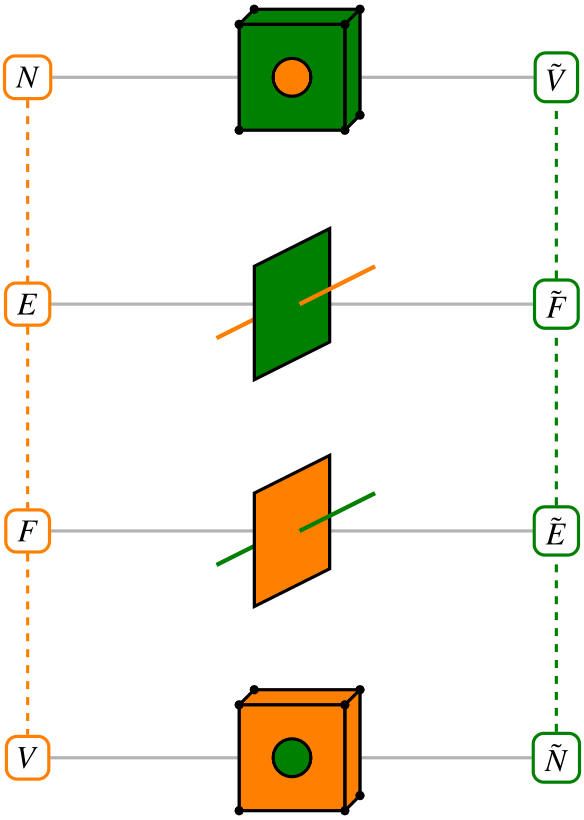

Figure 3.3: Duality relation between primal elements (orange) and dual ones(green).

$\tilde{F}$ and $\tilde{V}$ the ones of the dual grid, the N are associated to the $\tilde{V}$, the E to the $\tilde{F}$, the F to the $\tilde{E}$ and the V to the $\tilde{N}$, as Fig. 3.3 shows. An example of hexahedra (voxel-based) domain discretization is represented in Fig. 3.4.

Furthermore, the geometric elements of the primal mesh are endowed with orientation, which induces the orientation of the dual grid elements.

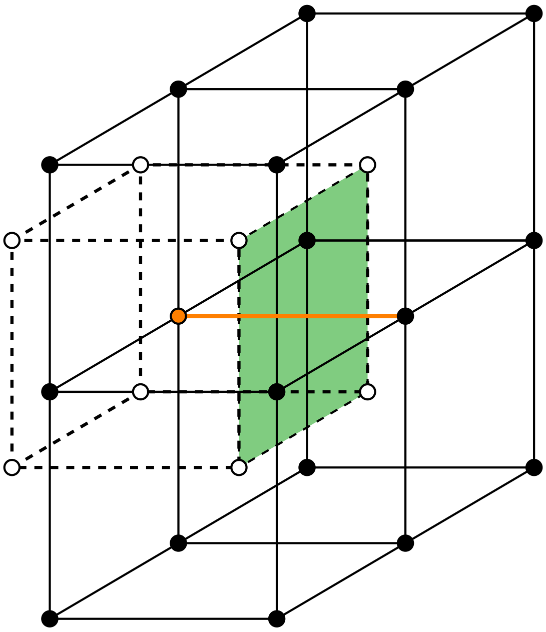

Figure 3.4: Example of domain discretization in two intertwined grids through the use of hexahedra: the primal mesh is represents with continuous lines, while the dual one with dashed lines. The duality relation between primal edges and dual faces is underlined.

3.1.2 Incidence matrices

From a mathematical point of view, the relation between the elements of cell complexes, shown in Fig. 3.3, can be described by continuous differential operators (gradient, curl and divergence), discrete operators and topological operators according to the problem formulation. All these operators are equivalent to their respective counterpart.

The topological operators are represented by the incidence matrices which link each element of n dimension to the one of $(n-1)$ dimension in the following way: edges-nodes, faces-edges and volumes-faces. Fig. 3.5 shows the construction of the primal and dual discrete operators incidence matrices. These figures are taken from [43]. According to Fig. 3.5, it can be seen that the possible values of the incidence matrices are 1, 0, -1, which depends on the topological element to which they refer and on its orientation in the primal or dual structure. These matrices are locally computed on each element and then are assembled in domain-based matrices [43]. In particular,

- $\mathbf{G}$ and $\tilde{\mathbf{G}}$ are the edge-to-node matrices of the primal and dual complex respectively (discrete gradient);
- $\mathbf{C}$ and $\tilde{\mathbf{C}}$ are the face-to-edge matrices of the primal and dual complex respectively (discrete curl);
- $\mathbf{D}$ and $\tilde{\mathbf{D}}$ are the volume-to-face matrices of the primal and dual complex respectively (discrete divergence).

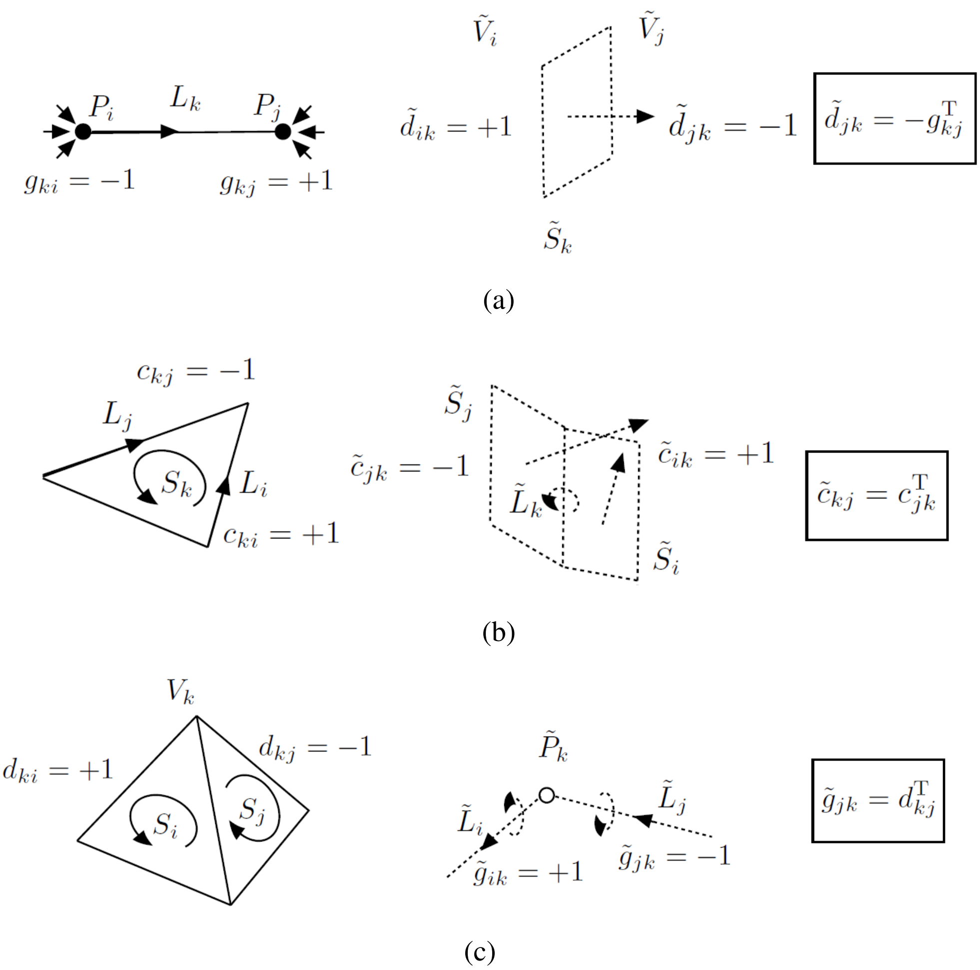

Figure 3.5: Primal gradient and dual divergence (a). Primal and dual curl (b). Primal divergence and dual curl (c).

Thanks to Fig. 3.3 and Fig. 3.5, it can easily be seen that there exist simple equations that link the incidence matrices of the primal complex to those of the dual one, which are:

$$\tilde{\mathbf{D}} = -\mathbf{G}^{\mathrm{T}}$$
$$\tilde{\mathbf{C}} = \mathbf{C}^{\mathrm{T}}$$
$$\tilde{\mathbf{G}} = \mathbf{D}^{\mathrm{T}}.$$

Finally, Tab. 3.1 shows the algebraic equivalence between the incidence matrices and the differential operators, by giving the chance to translate a differential equation that characterizes a physical problem into the algebraic equivalent one through accurate passages. Thanks to the equations, which link the incidence matrices of the primal complex to those of the dual one, it is possible to obtain the topological matrices associated

Differential operator	**Discrete operator**	**Topological operator**	**Relation**
gradient ∇	g_{en}	**G**	edge-to-node
curl $\nabla\times$	c_{fe}	**C**	face-to-edge
divergence $\nabla\cdot$	d_{vf}	**D**	volume-to-face

Table 3.1: Equivalence between various operator.

with the dual grid.

3.1.3 Topological and constitutive equations

Fig. 3.6 shows that, as in the differential form, also in the algebraic one there are equations that use the topological operators to link together elements belonging to the same mesh and to their correspondents on the dual one. These equations are called topological equations (vertical red lines) and constitutive equations (horizontal blue lines).

Topological equations link quantities in the same column of a Tonti diagram to each other and represent the link between the global variables referring to an oriented space-time element with others referring to its oriented boundary. They are expressed in terms of incidence matrices. However, topological equations are not sufficient to find the solution of a physical problem because they do not take into account the characteristics of the media. These characteristics are defined by the constitutive equations, which constrain the behaviour of physical phenomena to the characteristics of the media involved in the domain. Together (topological and constitutive equations) provide a unique solution of the physical problem.

Constitutive equations link quantities defined on the primal mesh to their dual ones along the horizontal line of the Tonti diagram. The construction of constitutive matrix, usually called $\mathbf{M}_i$, where i represents the media characteristic, is necessary for linking every quantity to its dual and for translating the point-wise information of media characteristics in terms of global variables.

Constitutive matrix construction according to the mesh

The type of polyhedra used in the discretization of the computational domain plays a fundamental role in the computation of the constitutive matrix. Here we report the most significant information to understand the numerical methods used in this thesis to solve low-frequency numerical dosimetry problems.

If the primal and dual grids are discretized with hexahedra, the orthogonality of the

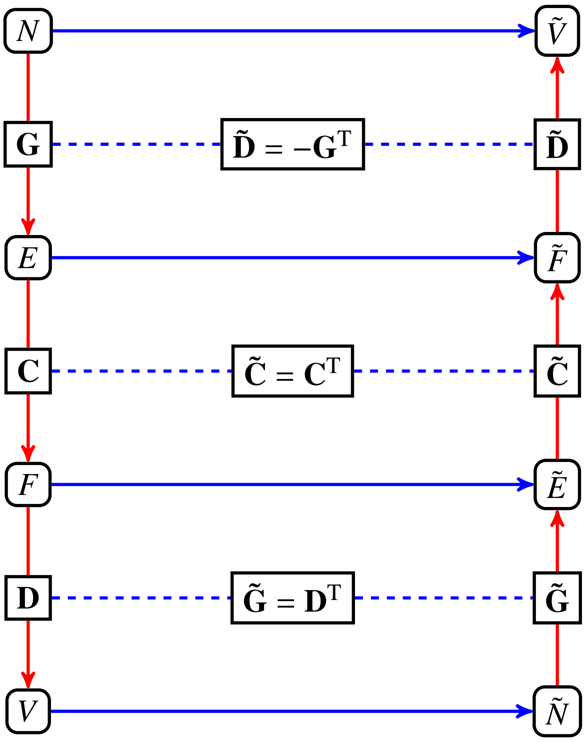

Figure 3.6: Relations between primal and dual grid in Tonti diagram through topological operators: the vertical red lines represent the topological equations, while the blu horizontal lines the constitutive equations. The blue dashed lines show the correspondences between topological operators belonging to the two different grids.

mesh allows to perform the computation running a loop along a primal quantity and storing the corresponding parameters on the diagonal of the matrix. Attention must be paid in the presence of material interfaces, where it is necessary to split the computation of the material coefficient into sub-portions of the space entity and then the various contributions can be summed in the proper matrix position.

When a tetrahedral grids is used, the lack of geometric orthogonality between dual entities makes the computation of constitutive parameters more complex than in the previous case. Two main different approaches can be highlighted in the computation of constitutive matrices on tetrahedra:

- a geometrical approach based on the application of simple geometric rules to the tetrahedron;
- the definition of local interpolation functions on the tetrahedron.

Under the hypothesis of a uniform field inside the tetrahedra, the first approach is the simplest one, while the other approach can be more convenient in case of more complex field patterns. In our computer program, to define material operators and constitutive

Global variables	Definition	Local variables	Definition
$\mathbf{A}$	Magnetic vector potential	a_k	Circulation
$\mathbf{B}$	Magnetic flux density	b_m	Magnetic flux
$\mathbf{E}$	Electric field	e_k	Electric voltage
$\mathbf{J}$	Current density	i_k	Electric current
φ	Electric scalar potential	φ_j	Electric potential

Table 3.2: Relation between global and local variables used in low-frequency numerical dosimetry problems.

equations for the algebraic formulation of the SPFD method we use Whitney elements (or, more precisely, Whitney forms) [46], [45], which interpolates functions inside the tetrahedron. Their use in the 3d magnetostatics is analyzed in [47]. In the context of the CM, Whitney elements are used as interpolators of point-wise physical quantities which have the corresponding global variables as degrees of freedom.

A deeply treatment of this topic can be found in [43].

3.2 The scalar potential finite difference (SPFD) method: from its differential form to its algebraic formulation

To solve a low-frequency numerical dosimetry problem by using the algebraic formulation of the scalar potential finite difference (SPFD) method, the discretization of the computational domain in a primal mesh and a dual grid is required. Let's suppose to work on a voxel-based discretization and that the primal mesh has N_N nodes, N_E edges, N_F faces and N_V volumes (the same reasoning can be applied to a tetrahedral mesh). As we have seen, each elements of the primal mesh is one-to-one associated to an element of the dual grid in order that there are exactly $N_{\tilde{N}} = N_V$ nodes, $N_{\tilde{E}} = N_F$ edges, $N_{\tilde{F}} = N_E$ faces and $N_{\tilde{V}} = N_N$ volumes. Tab. 3.2 shows the point-wise field quantities and their corresponding global variables that we will use in the formulas below and what they represent from a physics point of view. In particular, the electric voltage e_k and the circulation of the magnetic vector potential a_k are global variables obtained by integration of the point-wise electric field $\mathbf{E}$ and the magnetic vector potential $\mathbf{A}$ associated to the edges L_k with $k = 1, ..., N_E$, while the magnetic flux b_m is calculated from the magnetic

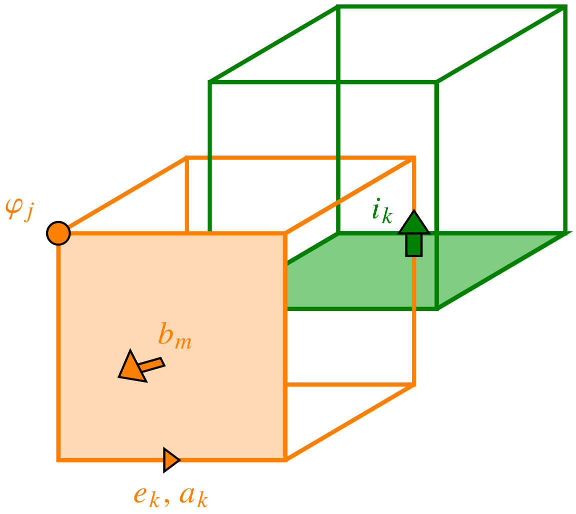

Figure 3.7: Global variables associated to spatial elements in the primal mesh (in orange) and dual mesh (in green) for on orthogonal mesh [49].

flux density **B** associated to the faces S_m with $m = 1, ..., N_F$ of the primal mesh:

$$e_k = \int_{L_k} \mathbf{E} \cdot \mathrm{d}\mathbf{L} \tag{3.1}$$

$$a_k = \int_{L_k} \mathbf{A} \cdot \mathrm{d}\mathbf{L} \tag{3.2}$$

$$b_m = \int_{S_m} \mathbf{B} \cdot \mathrm{d}\mathbf{S}. \tag{3.3}$$

The electric current i_k is obtained by integration of the current density **J** associated to the dual faces $\tilde{S}_k$ with $k = 1, ..., N_{\tilde{F}}$ [48]:

$$i_k = \int_{\tilde{S}_k} \mathbf{J} \cdot \mathrm{d}\mathbf{S} \tag{3.4}$$

Fig. 3.7 shows the primal and dual discretizations for an orthogonal mesh along with the global variables association to spatial entities. Hereinafter, the bold letters will refer to both vector quantities and matrices.

3.2.1 Differential form of the SPFD method

A low-frequency numerical dosimetry problem is governed by Maxwell's equations. Initially we consider their differential form.

The Gauss' law for magnetism states that the magnetic flux across any closed surface is equal to zero, in other words, that it is a solenoidal vector field. This is expressed as

$$\nabla \cdot \mathbf{B} = 0. \tag{3.5}$$

Due to the Helmholtz decomposition theorem, there exists a magnetic vector potential such that

$$\mathbf{B} = \nabla \times \mathbf{A}. \tag{3.6}$$

By considering (3.6) and the linear property of the curl operator, the Faraday's law becomes

$$\nabla \times \mathbf{E} = -\frac{\partial \mathbf{B}}{\partial t} \xrightarrow{\mathbf{B}=\nabla\times\mathbf{A}} \nabla \times \mathbf{E} = -\frac{\partial}{\partial t}(\nabla \times \mathbf{A}) \xrightarrow{\text{linear property}} \nabla \times \mathbf{E} = -\nabla \times \left(\frac{\partial \mathbf{A}}{\partial t}\right)$$

and, after collecting everything at first member, we obtain

$$\nabla \times \left(\mathbf{E} + \frac{\partial \mathbf{A}}{\partial t}\right) = 0.$$

From the curl operator properties, we can assert that there exists a scalar potential φ such that

$$\mathbf{E} + \frac{\partial \mathbf{A}}{\partial t} = -\nabla\varphi,$$

from which the electric field can be written

$$\mathbf{E} = -\nabla\varphi - \frac{\partial \mathbf{A}}{\partial t}. \tag{3.7}$$

Furthermore, since in low-frequency range the current density $\mathbf{J}$ is a solenoidal vector field and $\mathbf{J} = \sigma\mathbf{E}$, where σ is the electric tissue conductivity, keeping in mind (3.7), we find out that

$$\nabla \cdot \mathbf{J} = 0 \xrightarrow{\mathbf{J}=\sigma\mathbf{E}} \nabla \cdot (\sigma\mathbf{E}) = 0 \xrightarrow{(3.7)} \nabla \cdot \left(\sigma\nabla\varphi + \sigma\frac{\partial \mathbf{A}}{\partial t}\right) = 0$$

Since the low-frequency electromagnetic field is quasi-stationary, the displacement currents can be neglected. Moreover, in this range, the induced currents inside the human body do not modify the source field thanks to the very low electrical tissue conductivities. Therefore because the external field is unperturbed by the induced currents inside the human body, the external magnetic flux density $\mathbf{B}$ is known and, as we will see in the next chapter, thanks to (3.6) also the magnetic vector potential $\mathbf{A}$ is known and it is imposed by the current sources. Looking at the previous equation, the only unknown becomes the electric scalar potential φ and, for this reason, the scalar potential finite difference (SPFD) method can be formulated [50] as

$$\nabla \cdot (\sigma\nabla\varphi) = -\nabla \cdot \left(\sigma\frac{\partial \mathbf{A}}{\partial t}\right). \tag{3.8}$$

(3.8) is a partial differential equation defined in the time domain, but in the low-frequency range, the quasi-static approximation can be used [51], [52], [53]

$$\nabla \cdot (\sigma\nabla\varphi) = -\nabla \cdot (\mathrm{j}\omega\sigma\mathbf{A}).$$

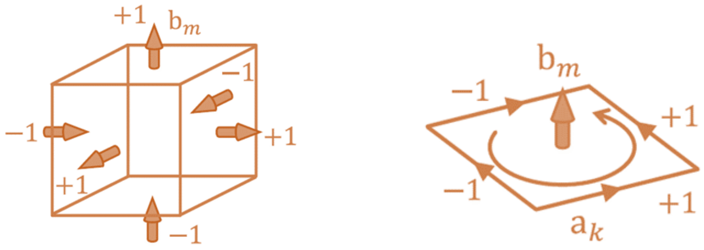

(a) (b)

Figure 3.8: Construction of discrete divergence and curl for magnetic equations. Magnetic discrete divergence (a). Magnetic discrete curl (b) [49].

3.2.2 Discrete form of the magnetic and electric equations

Since **B** is associated to the faces S_m with $m = 1, ..., N_F$ of the primal mesh, (3.5) can be integrated over the nth primal volume and, using the divergence theorem and definition (3.3), can be written in terms of global variables [49]:

$$\begin{aligned}\int_V \nabla\cdot\mathbf{B}d\mathbf{V} &= \oint_{S=\partial V}\mathbf{B}\cdot d\mathbf{S} = \sum_{m=1}^{N_F} d_{nm}\int_{S_m}\mathbf{B}\cdot d\mathbf{S}\\ &= \sum_{m=1}^{N_F} d_{nm}b_m = 0\end{aligned}\tag{3.9}$$

The summation operator in (3.9) sums the magnetic flux b_m of all faces in the primal mesh whose orientation is given by $d_{nm} \in \{-1,0,+1\}$ as Fig. 3.8a shown. d_{nm} represents the incidence number of the mth faces with respect to the nth volume. According to table Tab. 3.1, by collecting the equations corresponding to all primal volumes, in matrix form (3.9) becomes

$$\mathbf{Db} = \mathbf{0}$$

where **D** is the $N_V \times N_F$ volume-to-face incidence matrix in the primal mesh.

In the same way, the magnetic flux density b_m through the mth primal face can be linked to the line integral of the magnetic vector potential. In fact, considering (3.6), applying the Stoke's theorem to the mth face of the primal mesh and the definition (3.2), b_m can be written as [49]

$$b_m = \int_{S_m}\nabla\times\mathbf{A}\cdot d\mathbf{S} = \oint_{L_m=\partial S_m}\mathbf{A}\cdot d\mathbf{L} = \sum_{k=1}^{N_E} c_{mk}a_k$$

where $c_{mk} \in \{-1,0,+1\}$ is the incidence number of the kth edge with respect to the mth face of the primal mesh (see Fig. 3.8b). In matrix form it becomes

$$\mathbf{b} = \mathbf{Ca}$$

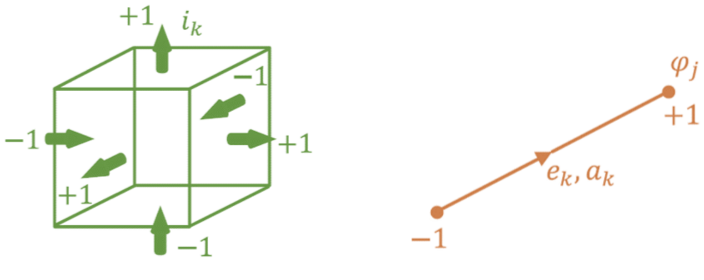

(a) (b)

Figure 3.9: Construction of discrete divergence and gradient for electric equations. Electric discrete divergence (a). Electric discrete gradient (b) [49].

where **C** is the $N_F \times N_E$ face-to-edge incidence matrix in the primal mesh.

Following the same steps used for the magnetic Gauss' law and using the definition (3.4), in discrete form the charge conservation equation in case of quasi-static conditions becomes [49]

$$\int_{\tilde{V}} \nabla \cdot \mathbf{J} \mathrm{d}\mathbf{V} = \oint_{\tilde{S}_j = \partial \tilde{V}_j} \mathbf{J} \cdot \mathrm{d}\mathbf{S} = \sum_{k=1}^{N_{\tilde{F}}} \tilde{d}_{jk} i_k = 0 \tag{3.10}$$

where $\tilde{d}_{jk} \in \{-1, 0, +1\}$ is the incidence number of the kth face with respect to the jth volume in the dual grid (see Fig. 3.9a). Collecting all $\tilde{d}_{jk}$ coefficients in the $N_{\tilde{V}} \times N_{\tilde{F}}$ volume-to-face incidence matrix $\tilde{\mathbf{D}}$ on the dual mesh, (3.10) becomes

$$\tilde{\mathbf{D}}\mathbf{i} = \mathbf{0} \tag{3.11}$$

Finally, considering the electric field equation (3.7) expressed in the frequency domain, it can be integrated by using definition (3.1) (see Fig. 3.9b) [49]

$$\begin{aligned} e_k = \int_{L_k} \mathbf{E} \cdot \mathrm{d}\mathbf{L} &= \int_{L_k} (-\nabla \varphi - j\omega \mathbf{A}) \cdot \mathrm{d}\mathbf{L} \\ &= -\sum_{j=1}^{N_N} g_{kj} \varphi_j - j\omega a_k \end{aligned} \tag{3.12}$$

where $g_{kj} \in \{-1, 0, +1\}$ is the incidence number of the jth node with respect to the kth edge in the primal mesh. Collecting all g_{kj} coefficients in the $N_E \times N_N$ edge-to-node incidence matrix **G**, (3.12) in matrix form becomes

$$\mathbf{e} = -\mathbf{G}\varphi - j\omega \mathbf{a}. \tag{3.13}$$

Differential form	**Algebraic form**
$\nabla \cdot (\sigma \nabla \varphi) = -\nabla \cdot (\mathrm{j}\omega\sigma\mathbf{A})$	$\mathbf{G}^{\mathrm{T}}\mathbf{M}_\sigma\mathbf{G}\varphi = -\mathrm{j}\omega\mathbf{G}^{\mathrm{T}}\mathbf{M}_\sigma\mathbf{a}_{\mathrm{s}}$
$\mathbf{E} = -\nabla\varphi - \mathrm{j}\omega\mathbf{A}$	$\mathbf{e} = -\mathbf{G}\varphi - \mathrm{j}\omega\mathbf{a}_{\mathrm{s}}$
$\mathbf{J} = \sigma\mathbf{E}$	$\mathbf{i} = \mathbf{M}_\sigma\mathbf{e}$

Table 3.3: Comparison between differential and topological form of the SPFD method in the frequency domain.

3.2.3 Constitutive equation and algebraic formulation of the SPFD method

The constitutive equations link the electric current with the electric voltage. Keeping in mind what was analyzed in paragraph 3.1.3, a constitutive matrix is built according to the type of polyhedra used in the domain discretization and for a low-frequency numerical dosimetry problem the equation expressed in matrix form becomes

$$\mathbf{i} = \mathbf{M}_\sigma\mathbf{e} \tag{3.14}$$

where $\mathbf{M}_\sigma$ is the conductance constitutive matrix.

Thanks to the relation between differential and topological operators, as shown in Tab. 3.1 and also highlighted by the computations made in paragraph 3.2.2, considering the links between the incidence matrices of the primal and dual grid, we can substitute (3.13) and (3.14) in (3.11), and obtain

$$\mathbf{G}^{\mathrm{T}}\mathbf{M}_\sigma\mathbf{G}\varphi + \mathrm{j}\omega\mathbf{G}^{\mathrm{T}}\mathbf{M}_\sigma\mathbf{a} = \mathbf{0}. \tag{3.15}$$

Finally, as said before, because the external magnetic flux density is not perturbed by the magnetic field due to the induced current within the human body, the line integral of the magnetic vector potential $\mathbf{a}_{\mathrm{s}}$ is known and imposed by the current sources. The only unknown of (3.15) is the electric scalar potential φ computed on each node of the primal mesh (Fig. 3.7). The algebraic formulation of the SPFD method becomes

$$\mathbf{G}^{\mathrm{T}}\mathbf{M}_\sigma\mathbf{G}\varphi = -\mathrm{j}\omega\mathbf{G}^{\mathrm{T}}\mathbf{M}_\sigma\mathbf{a}_{\mathrm{s}}. \tag{3.16}$$

The low-frequency numerical dosimetry problems studied in this work are solved by using (3.16) with the electric scalar potential as nodal unknowns. Subsequently, the knowledge of the electric scalar potential allows to evaluate the electric field in the barycenter of each element by using (3.13).

In the next chapter we will see the possible ways to calculate $\mathbf{a}_{\mathrm{s}}$ starting from the knowledge of the external magnetic flux density and we will compare two different methods based on the curl inversion of (3.6).

3.3 Conclusion

Tab. 3.3 compares the differential and topological formulation of the SPFD method in the frequency domain, underling the relation between differential and topological operators. In this thesis, the numerical dosimetry problem formulated for the evaluation of human exposure to low-frequency electromagnetic fields will be studied by using the algebraic formulation.

Keeping in mind what has been said, the most relevant fact is that the induced currents inside the human body do not modify the source fields and for this reason they can be studied separately. This allows to divide a numerical dosimetry problem into two steps:

- simulation of the source field without the human body, since the magnetic vector potential is unperturbed by the presence of the biological tissues;
- resolution of the dosimetric problem by considering only the human body.

Chapter 4

Comparison of numerical techniques used to compute the magnetic vector potential starting from measurement data

The interest of performing numerical dosimetry starting from data coming from general purpose software or real measurements is constantly growing. A low-frequency numerical dosimetry problem can be formulated with the scalar potential finite difference (SPFD) method as nodal unknowns [50]. Solving this kind of problem require the knowledge of the magnetic vector potential **A** (or, in its algebraic formulation, the circulation of the magnetic vector potential a_k along the edges of the primal mesh), knowledge that is not straightforward when: a) the software used to model the source does not provide the magnetic vector potential as output; b) the model of the geometrical and the electrical layout of the source is very complex; c) no information is available about the source but only magnetic flux density **B** measurements. In all these cases **A** can be computed starting from the knowledge of **B** [54],[49], [55].

Recently, [55] proposed a method that encloses the magnetic field source in a virtual box. The approach starts from the knowledge of **B** on the external surface of this box. No real measurements have been considered but a huge number of virtual measurements have been used to estimate the uncertainty propagation. It is shown that this method has advantages over an alternative approach that starts from measurements inside the volume including the human body. If the magnetic field source is small (e.g. transcranical magnetic stimulation (TMS)) the proposed approach is definitely a good option, however, for other sources its application can be difficult (e.g. a power system substation) or impossible (e.g. an overhead power line).

In this chapter a comparison between two methods [49], [54] that allow to evaluate **A** starting from the knowledge of **B** in a volume including the human body is done. These methods are both based on the curl inversion of (3.6), i.e. $\mathbf{B} = \nabla \times \mathbf{A}$, but two different

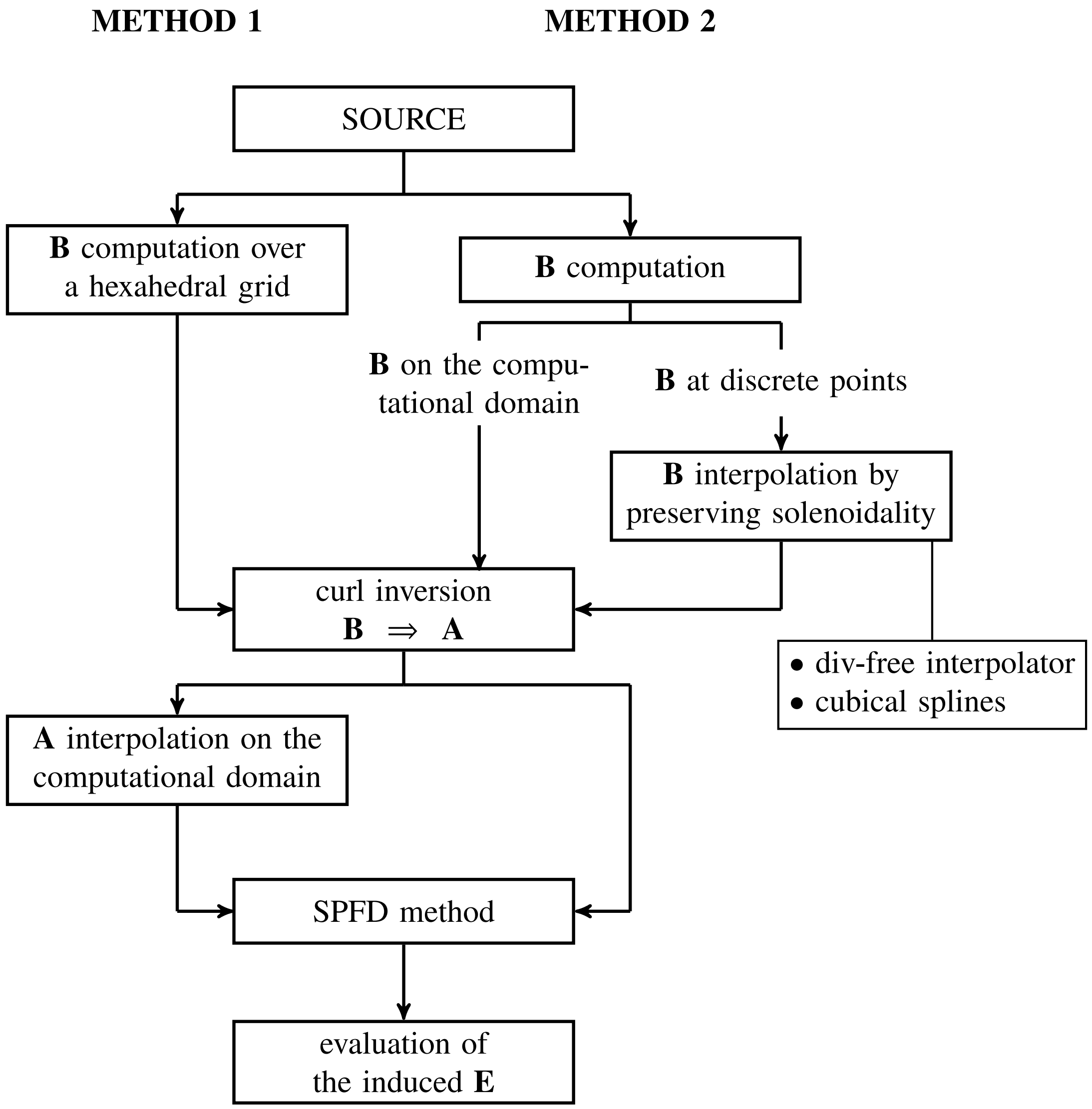

Figure 4.1: Scheme of the two uncurl methods: the method 1 approach [54] is described on the left side of the scheme, while the method 2 approach [49] is summarized on the right side of the scheme.

approaches are proposed: [54] proposes an analytical approach, while [49] a topological one. These results have been published in [56].

4.1 Uncurl methods description

We have seen that the magnetic flux density and the magnetic vector potential are linked to each other by the formula $\mathbf{B} = \nabla \times \mathbf{A}$. Therefore, if we want to calculate $\mathbf{A}$

starting from the knowledge of **B**, we have to invert this formula. We will see in the next paragraphs the two methods proposed by [49] and [54] to carry out this inversion. Hereinafter, we will refer to method 1 and method 2 to identify the approaches described in [54] and [49], respectively. Fig. 4.1 summarizes the two methods steps.

4.1.1 Uncurl inversion problem

The main problem behind curl inversion is that **A** is unique up to a gradient of a scalar function f. In fact, if $\mathbf{A}' = \mathbf{A} + \nabla f$ is a second magnetic vector potential and remembering that the curl of a gradient is the zero vector field, we can write

$$\nabla \times \mathbf{A}' = \nabla \times (\mathbf{A} + \nabla f) = \nabla \times \mathbf{A} + \underbrace{\nabla \times \nabla f}_{\mathbf{0}} = \nabla \times \mathbf{A},$$

which means that

$$\mathbf{B} = \nabla \times \mathbf{A} = \nabla \times \mathbf{A}'. \tag{4.1}$$

Therefore an infinity number of possible magnetic vector potentials that satisfy (4.1) exists. This arbitrariness of **A** is called gauge freedom.

This curl inversion problem can be also seen from a topological point of view. In Chapter 3 we have seen that (4.1) can be expressed in matrix form as

$$\mathbf{b} = \mathbf{C}\mathbf{a}, \tag{4.2}$$

where **C** is the $N_F \times N_E$ face-to-edge incidence matrix. It is a rectangular matrix and for this reason the solution of (4.2) is not unique. In order to make the problem solvable, the discrete curl matrix **C** must be restricted to the set of independent circulations and independent fluxes.

Method 1 and method 2 are based on two different approaches to solve this uncurl inversion problem.

4.1.2 Method 1

In [54] a general analytical formulation and numerical implementation for calculating **A** from **B** in Cartesian coordinates is presented. They have validated their method analytically on a circular current loop placed over a homogeneous half space and by simulating a TMS of the hand motor area of the brain featuring realistic magnetic coil and head models.

Method 1 is based on the knowledge of the magnetic flux density $\mathbf{B} = (B_x, B_y, B_z)$ at discrete points in a bounded hexahedral grid, which will contain the human model. The components of $\mathbf{A} = (A_x, A_y, A_z)$ are first obtained on the same grid by means of analytic

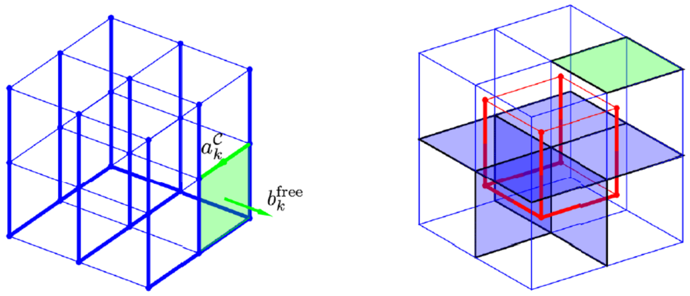

(a) (b)

Figure 4.2: The independent cotree circulations $\mathbf{a}^c$ are highlighted together with the fundamental loop (a). Identification of independent fluxes: in red a tree of the internal dual edges; in blue the corresponding primal faces; in green the additional boundary face (b). These figures are taken from [49].

formulas, which derive from the formulas presented in [57]

$$\begin{aligned}
A_x = & -\int_0^y \left(\frac{1}{3}B_z(x,y',z) + \frac{1}{6}B_z(x,y',0)\right) dy' \\
& + \int_0^z \left(\frac{1}{3}B_y(x,y,z') + \frac{1}{6}B_y(x,0,z')\right) dz' \\
A_y = & -\int_0^z \left(\frac{1}{3}B_x(x,y,z') + \frac{1}{6}B_x(0,y,z')\right) dz' \\
& + \int_0^x \left(\frac{1}{3}B_z(x',y,z) + \frac{1}{6}B_z(x',y,0)\right) dx' \\
A_z = & -\int_0^x \left(\frac{1}{3}B_y(x',y,z) + \frac{1}{6}B_y(x',0,z)\right) dx' \\
& + \int_0^y \left(\frac{1}{3}B_x(x,y',z) + \frac{1}{6}B_x(0,y',z)\right) dy'.
\end{aligned} \tag{4.3}$$

Then **A** is interpolated on the computational domain to proceed with the classical SPFD scheme. A simple tri-linear interpolation of **A** is sufficient to get very stable results. As a last remark, it is worth noting that the gauge applied to the magnetic vector potential coming from (4.3) is not known a priori because it depends on the arbitrary selection of the coordinate system (x, y, z) and its origin. This is not an issue because every compatible magnetic vector potential can be used in (3.16).

4.1.3 Method 2

Method 2 is a topological approach defined within the algebraic framework. In [49] it is tested on a benchmark problem and on a real exposure scenario where the magnetic field due to a power transformer was measured.

The method is based on the computation of the circulation of the magnetic vector potential by solving the following system:

$$\begin{aligned} \mathbf{C}_R \mathbf{a}^c &= \mathbf{b}^{\text{free}} \\ \mathbf{a}^\tau &= 0 \end{aligned} \tag{4.4}$$

where $\mathbf{b}^{\text{free}}$ is a set of independent magnetic fluxes flowing through the faces, $\mathbf{C}_R$ is the discrete curl incidence matrix restricted to the independent fluxes, and $\mathbf{a}^c$ and $\mathbf{a}^\tau$ are the cotree and tree circulations, respectively. One of the possible vector of circulations $\mathbf{a}$ can be obtained by joining $\mathbf{a}^\tau \cup \mathbf{a}^c$. $\mathbf{b}^{\text{free}}$, $\mathbf{a}^c$ and $\mathbf{a}^\tau$ are defined using the tree-cotree decomposition (a tree is a set of branches that connect all nodes with no loops, while a cotree is the set of branches that does not belong to a tree). [58].

The equation $\mathbf{a}^\tau = 0$ of the system (4.4) is obtained by set to zero the $N_N - 1$ circulations associated to the tree edges, while the remaining $N_E - N_N + 1$ edges constitute the set of independent circulations $\mathbf{a}^c$. These independent circulations are one-to-one associated to $N_E - N_N + 1$ independent fluxes $\mathbf{b}^{\text{free}}$ that pass through the fundamental loops constructed from the cotree edges (Fig. 4.2a). In order to find these independent fluxes, it is necessary to note that, because of the Gauss' law $\mathbf{Db} = \mathbf{0}$, not all fluxes are linearly independent. In fact, the flux through one of the boundary faces is linearly dependent to the others. This dependent flux can be selected randomly among the boundary faces. The remaining $N_V - 1$ dependent fluxes are selected using the following procedure (Fig. 4.2b):

- a tree $\tilde{\tau}$ is formed on the dual mesh. This tree is made of $N_{\tilde{N}} - 1 = N_V - 1$ edges;
- the primal faces $F_{\tilde{\tau}}$ associated to the dual tree edges are selected.

This set of dependent fluxes (union of one random flux through a boundary face and the internal fluxes through $F_{\tilde{\tau}}$) is removed from the right-hand side in (4.2) and the discrete curl incidence matrix $\mathbf{C}_R$ restricted to the independent fluxes and circulations is found.

Method 2 is strictly related to the computational domain and this can be an advantage when the source magnetic flux density comes from simulations. In this case one can directly compute $\mathbf{b}^{\text{free}}$ at the voxel faces. It is a disadvantage when the source magnetic flux density is known at discrete points. In this case one must interpolate it to get $\mathbf{b}^{\text{free}}$ at the voxel faces. The interpolation of $\mathbf{B}$ requires more attention to preserve the solenoidality. In the original study [49] a divergence-free interpolator based on Gaussian radial basis functions is proposed. In the next paragraphs, more details are given about the uncertainty propagation depending on the interpolation method and the type of input data.

4.2 Exposure scenario

Fig. 4.3a shows the exposure scenario used to compare the two different methods. A five-turn coil with inner radius of 70 mm and wire radius of 3 mm is located 200 mm

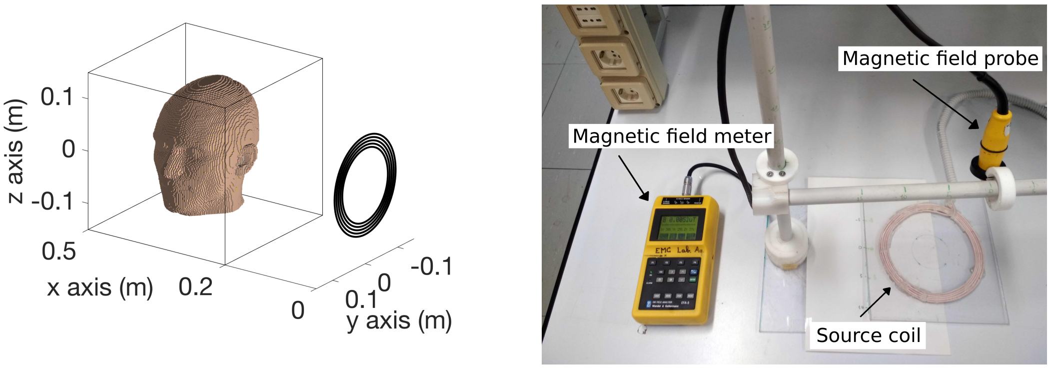

(a) (b)

Figure 4.3: Exposure scenario (a). Laboratory setup (b).

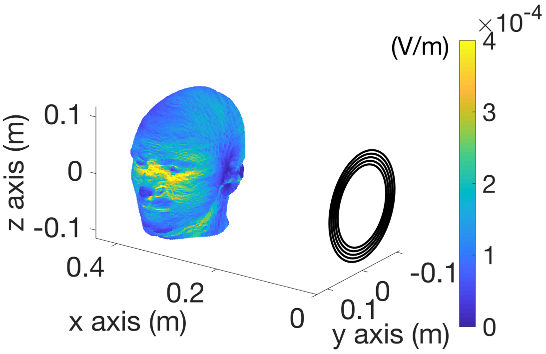

Figure 4.4: Reference solution $\mathbf{E}_0$ for the induced electric field.

away from a square box. The side of the box is 300 mm. Each wire carries 1 A and the operating frequency is 1 kHz. The center of the coil corresponds to the origin of the reference system and the axis of the coil is the x-axis. The head of the Duke model, belonging to the Virtual Family [22] with voxel size $2 \times 2 \times 2$ mm^3, is centered in the square box and the coronal plane is the xz plane.

The exposure scenario is simple enough for simulations and also for laboratory measurements as shown in Fig. 4.3b. Measurements are performed with a NARDA commercial meter and the data are freely available at [59]. Reference solution is provided with direct calculation of the source magnetic flux density $\mathbf{B}$ and the magnetic vector potential $\mathbf{A}$, and with the simulation of the induced electric field $\mathbf{E}_0$, shown in Fig. 4.4. Fig. 4.5 shows the measured $\mathbf{B}$ magnitude at 64 and 343 points on three cut planes and the corresponding representations of the $\mathbf{B}$ vector.

Methods 1 and 2 are used to test their performance by considering: 1) $\mathbf{B}$ coming from a simulation software, 2) $\mathbf{B}$ coming from measurements. In the latter case several

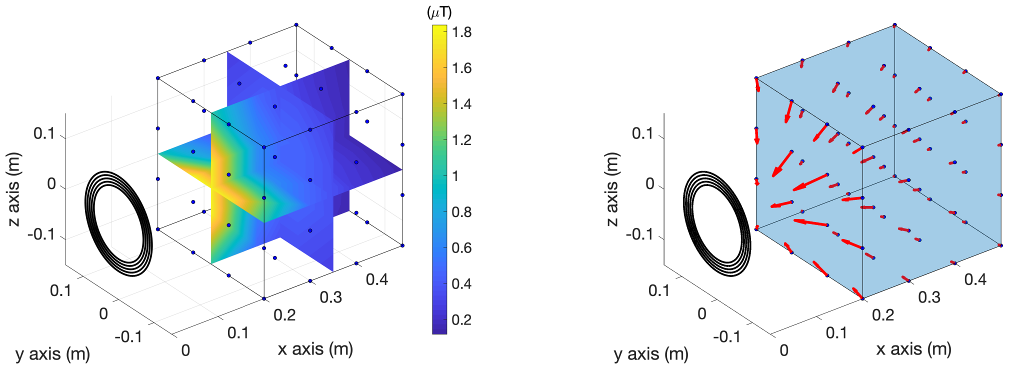

(a) Magnitude of **B** at 64 points on three cut-planes.

(b) Representation of the **B** vector at 64 points.

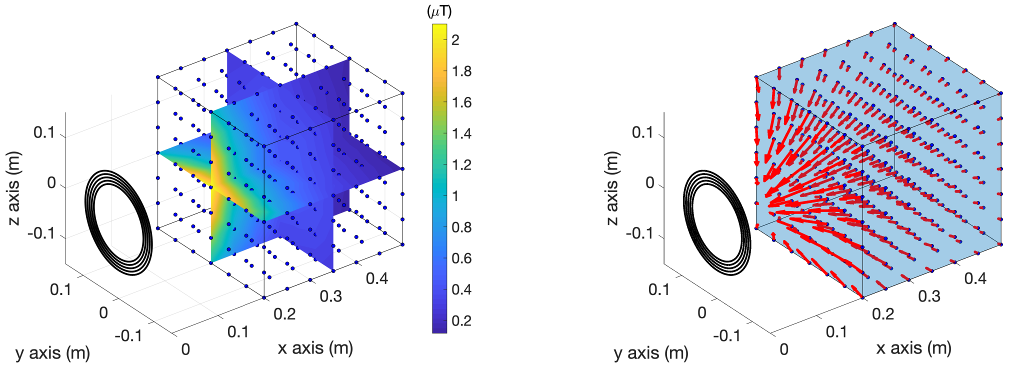

(c) Magnitude of **B** at 343 points on three cut-planes.

(d) Representation of the **B** vector at 343 points.

Figure 4.5: Measurement at discrete points with equal grid spacing along each directions.

virtual measurements are generated to estimate the uncertainty propagation and true measurements are carried out to validate the two approaches. In all cases, the quality of the obtained results is taken into account using a relative error Δ defined as

$$\Delta = \sqrt{\sum_k \|\mathbf{F}_k - \mathbf{F}_{k,0}\|^2 / \sum_k \|\mathbf{F}_{k,0}\|^2} \tag{4.5}$$

where $\mathbf{F}_k$ is the magnetic or electric field at the kth voxel, whereas $\mathbf{F}_{k,0}$ is the corresponding reference value.

4.3 Numerical analyses

In this paragraph it is considered that the input for both methods is a **B** coming from simulations. In the first subsection we consider the case when the magnetic field

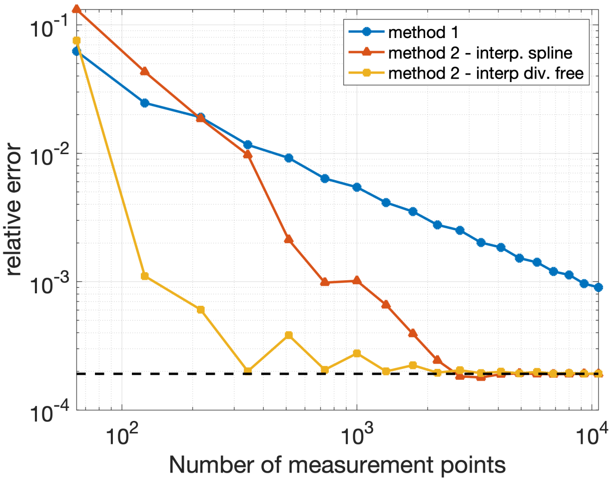

Figure 4.6: Relative error of the induced electric field computed starting from the exact magnetic flux density.

source is simulated with a specific software that is unable to perform the dosimetry step. Therefore, **B** is exported and used with methods 1 and 2. In the second subsection we create virtual measurements to analyze the effect of a random noise superposed to **B**. In both subsections a large number of virtual measurements is considered in order to study the effects of the grid size. The measurements are generated on a regular grid with a regular grid size along each axis. The number of measurements varies from 64 to 10648 points.

4.3.1 Magnetic flux density coming from a simulation software

In a simple source configuration, **B** can be computed exactly up to the machine tolerance. Both methods are adopted to invert the exact **B** discretized at a number of points from 64 to 10648. Since method 2 requires the interpolation of **B**, two procedures are tested: an interpolation with cubical splines and the divergence-free interpolator proposed in [49]. The results are shown in Fig. 4.6. All methods are used to compute the induced electric field in the head and then the relative error is quantified. Looking at Fig. 4.6, it can be seen that the relative error always decreases with the increase of the number of measurement points. Method 2 makes it possible to obtain the lowest relative error by means of the divergence-free interpolator even with little information about the **B**. A relative error of about 10^{-3} is obtained with only 125 points. Furthermore, since method 2 is defined directly on the computational domain, the **B** could be exported directly at each center of the voxel faces. The black dashed line in Fig. 4.6 represents the relative error for this case (independent of the number of points). This is the best result that can be obtained with method 2 because it does not include the interpolation error. The same value cannot be quantified for method 1 because it must work first on a regular

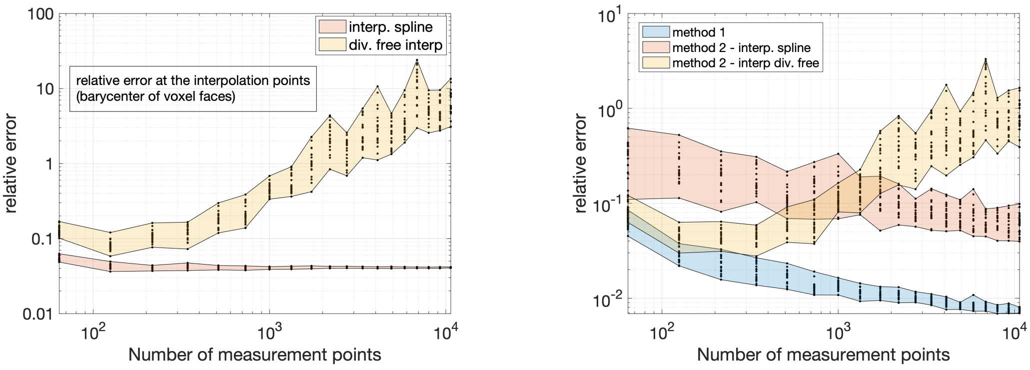

(a) (b)

Figure 4.7: Relative error for magnetic field interpolation performed for the use of method 2 (a). Relative error for the induced electric field (b).

grid and then it interpolates the magnetic vector potential on the computational domain.

For more than about 500 points, method 2 coupled with the divergence-free interpolation converges to the dashed line. This also means that more than 500 points are not necessary to get a very good accuracy. It is worth observing that above 500 points fluctuations of the relative error appear because the interpolation procedure is not yet preconditioned [60]. Finally, method 2 coupled with the spline interpolator should be avoided because it causes always a higher relative error.

4.3.2 Effect of the noise on the magnetic flux density

Now we want to see what happens when a random noise in the range 0 – 5 % is superposed to the exact computed magnetic flux density. The maximum value of 5 % is chosen in agreement with [55]. For each different number of points used to discretize the inspection volume: a) 20 magnetic field distributions with noise are generated, b) for method 2 only the relative error of the magnetic field interpolation is evaluated, c) the induced electric field is evaluated and the relative error is computed for both methods 1 and 2.

Fig. 4.7a shows the magnetic field interpolation error for method 2. It is immediately clear that the divergence-free interpolator is very sensitive to the random noise. In fact, the relative error dramatically increases with the number of measurement points (10, i.e. 1000 %, with 10648 points). The same sensitivity is not found for the spline interpolator that keeps the relative error in the same order of the random noise (i.e. 5%).

Fig. 4.7b shows the relative error on the electric field obtained using the magnetic field distributions previously described. SPFD method needs the circulation of the magnetic vector potential as right hand side of (3.16). This step involves an integral of the magnetic vector potential that has a smoothing effect of the error on **B**. In fact, the relative errors of the electric field are always lower than the related magnetic field (in Fig. 4.7a). Method 1,

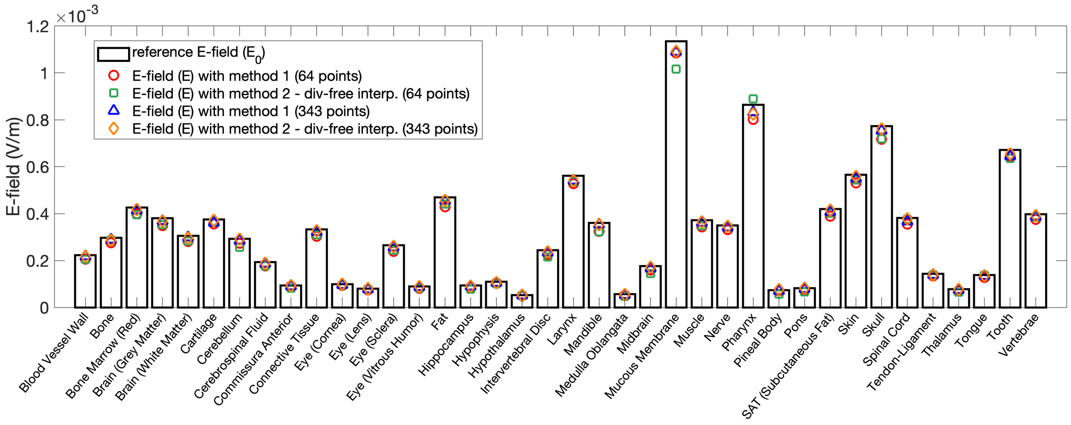

Figure 4.8: Maximum value of the electric field at each tissue. Method 1 and method 2 are used starting from real measurements at 64 and 343 points. Results are compared with the reference case.

whose curl inversion is based on an integration (see (4.3)), has a further smoothing effect that makes it not sensitive to the noise. For method 1 the error is always decreasing as the number of measurement points increases. The same trend is found for method 2 with the spline interpolator, however, the error is significantly higher than the one obtained with method 1. Therefore, the spline interpolator should be definitely avoided.

Regarding method 2 coupled with the divergence free interpolator, the relative error is acceptable in the first part of the plot but then increases again. This is due to the fact that the divergence-free interpolator is based on Gaussian radial basis functions, which constrain the interpolated magnetic field to be solenoidal. Gaussian radial basis functions work locally and, for higher number of points, the original magnetic field (that is not solenoidal due to the noise) is modified into a different solenoidal magnetic field distribution. This is the reason why the relative error is higher (for both **B** and **E**) when more measurement points are used. To sum up, method 2 coupled with the divergence free interpolator provides acceptable results (comparable with method 1) when the measurement grid for the magnetic field is not too dense, that is when the ratio between the grid spacing of the measurement grid and the side of the voxel is larger than 25 (i.e. low number of measurement points).

Bearing all this in mind, and considering that the measurement task is very time consuming especially for complex sources [49], it is interesting the fact that an acceptable relative error can be obtained with few points (e.g. lower than 500).

4.4 Experimental analyses

The two methods under comparison have been tested carrying out real measurements with the laboratory setup described in paragraph 4.2, Fig. 4.3b. Exploiting the results

Table 4.1: Relative error and deviation of the electric field

Number of points	**Approach**	Δ	$\mathbf{E}/\mathbf{E}_0$
64	method 1	0.08672	0.95607
	method 2 (div-free interp.)	0.10063	0.89511
343	method 1	0.03127	0.96102
	method 2 (div-free interp.)	0.03226	0.96190

obtained in previous sections, in this analysis method 2 coupled with spline interpolation is not included and the magnetic field has been measured only at few points, 64 and 343. The electric field is computed with the SPFD method and possible numerical artifacts coming from the voxelized model are avoided by filtering the raw numerical solution with the 99.9th percentile approach [36]. Fig. 4.8 shows the results and it is apparent that both methods provide a good estimation of the electric field in all tissues. Tab. 4.1 summarizes the relative error of the numerical solution and the deviation at the tissue with maximum exposure (mucous membrane). The largest deviation, evaluated as $\mathbf{E}/\mathbf{E}_0$, is ~ 0.9 (i.e., underestimation of 10 %).

4.5 Discussion

Two methods for calculating the magnetic vector potential starting from the knowledge of the magnetic flux density at discrete points have been analyzed. It is found that when the magnetic field comes from a simulation tool, method 2 coupled with a divergence free interpolator provides the most accurate results.

When the magnetic field is obtained through real measurements, method 1 is the preferred solution because it provides very stable results in any test condition. On the contrary, the use of method 2 requires more attention because a large number of measurement points could lead to higher errors.

Method 2 coupled with the spline interpolation, instead, must be always avoided because it provides higher errors then the other two methods in every situations.

This study also shows that a huge number of measurement points is not necessary. It is found that if the ratio between the grid spacing of the measurement grid and the side of the voxel is higher than 25 the quality of the results is acceptable. In fact, when a cube with side of 300 mm is discretized with 64 or 343 points, very similar results are obtained. A maximum deviation of 10 % is observed in the case of 64 points. Deviations in this order of magnitude are more than acceptable for a dosimetric assessment since other uncertainties (e.g. anatomical details, tissue properties,...) have the same order of magnitude.

Chapter 5

The use of tetrahedral meshes in low-frequency numerical dosimetry to remove stair-casing errors

In this chapter the use of human models discretized with tetrahedral meshes to remove stair-casing approximation errors resulting from the use of voxel-based one is proposed. Suitable and realistic exposure scenarios are created and a comparison between the computational errors that affect the induced electric field strengths in voxelized and tetrahedral models is done. We will see that tetrahedral meshes make it possible to remove completely stair-casing errors in numerical dosimetry, however, in real exposure scenarios, other sources of artifacts are still present and must be filtered out with suitable techniques.

5.1 Tetrahedral meshes in low-frequency numerical dosimetry

In the past few years, geometric modelling software started to develop thanks to the large diffusion of computer science technologies. Computer geometric modelling finds use in numerous sector like industrial engineering, automotive engineering, robotics, medical imaging, etc. These programs reproduce the objects shape using NURBS (Non Uniform Rational Basis-Splines) or other primitives that best approximate their surfaces. Subsequently, in order to be able to use these objects for numerical studies, their domain is discretized with hexahedral or tetrahedral elements. In particular, the use of tetrahedral meshes is recommended for the discretization of curved boundaries to avoid stair-casing effects thanks to the tetrahedra shape.

As we have seen in paragraph 2.3, most of realistic whole-body human models used in numerical dosimetry are built starting from DICOM (Digital Imaging and Communications in Medicine) images and, for this reason, are discretized with a voxel-based meshes.

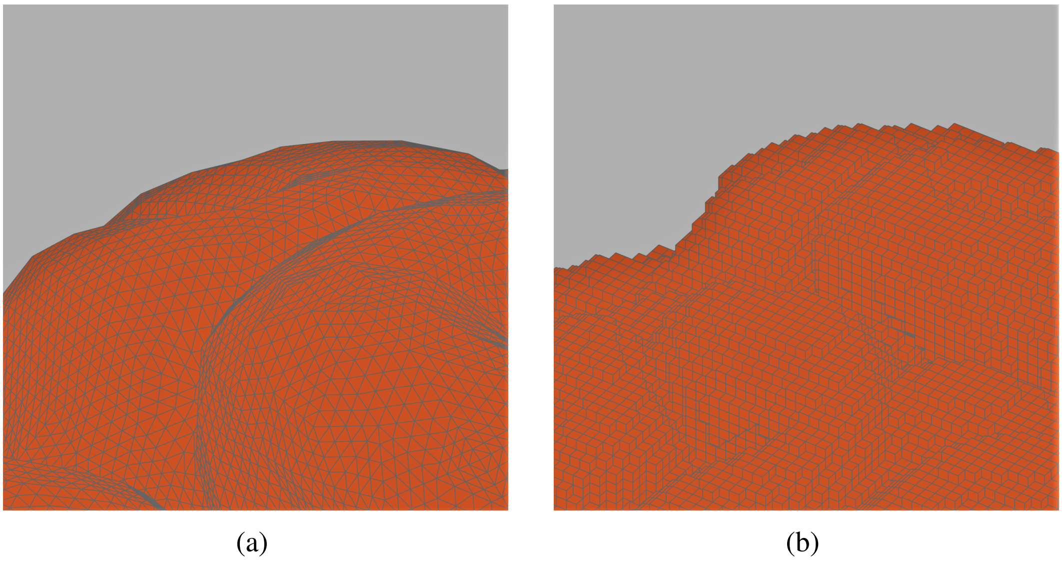

Figure 5.1: No stair-casing effect on curved boundaries thanks to tetrahedral discretization (a). Stair-casing effect on curved boundaries due to the use of a voxel-based mesh (b).

Stair-casing approximation errors occur using these human models in the evaluation of human exposure to low-frequency electromagnetic fields, especially when large contrasts in tissue conductivity between neighbouring voxels are present. Due to their shape, in fact, voxels are not suitable for reproducing curved boundaries, as Fig. 5.1 shows. For this reason, the post-processing techniques described in paragraph 2.4.1 are needed to suppress those numerical artifacts.

Over the last decades, thanks to the use of geometric modelling software, the organs and tissues of human models derived from DICOM images have been reconstructed using three-dimensional objects (like NURBS, etc.), giving the chance to discretize their domain with tetrahedral meshes and to better reproduce the boundaries of curved surfaces. Human models discretized with tetrahedral meshes started to be used both in low-frequency numerical dosimetry and high-frequency numerical dosimetry, such as in [61] where a procedure to optimize the specific absorption rate deposed in a patient during oncology hyperthermia treatment is presented.

In [62] and [63] an anatomical model of the human body made of tetrahedral elements and obtained from CT scans is used to validate new methodologies based on three-dimensional finite elements and A-φ formulation to compute the induced currents into the human body due to LF magnetic fields generated respectively by realistic devices and a completely unknown power system. In [64] two dual finite elements formulations to perform numerical dosimetry are presented. Two human models discretized with tetrahedral elements are used in the analysis of the numerical errors related to the proposed methodology: the ZOL phantom built using the software AMIRA starting from the segmented data of the Visible Human Project® (VHP), and the Ella phantom based on the Virtual Family, whose tetrahedral mesh was generated from the 1 mm voxel model by means of a free toolbox.

It is interesting to note that in these papers the authors' attention is focused on the validation of the new proposed formulations and not on the possible numerical artifacts caused by the use of tetrahedral models.

The comparison between tetrahedral and voxel-based meshes is the main topic of this chapter. A first indirect comparison has been made in [65] where the authors validated their proposed method on the tetrahedral human model ZOL and the numerical results are compared with some existing data evaluated on voxelized human models. The comparison showed some inconsistencies between the data obtained on the tetrahedral models and on the voxel-based ones. The authors underlined the difficulties in comparing different models and methods due to the fact that discretization and post-processing techniques play a not negligible role. However, they only made assumptions about this topic and they did not perform a detailed analysis on the nature of the numerical artifacts present in tetrahedral and voxel-based meshes.

In [35], instead, authors compared the use of tetrahedral and voxel-based meshes with the idea of eliminating the stair-casing effect thanks to tetrahedral meshes. They found out that although tetrahedral meshes improved the modelling of tissue boundaries, numerical artifacts were registered and filtering approaches were still necessary. However, they did not provide any reason for the apparent failure of tetrahedral meshes.

We worked on this topic at the same time as these authors. We have analyzed the problem from another point of view, but we have arrived to their same conclusions. In this chapter, compared to [35], a rigorous experimental methodology to identify the source of numerical artifacts produced by tetrahedral meshes is used and additional details on the role of tetrahedral meshes in low-frequency dosimetry are given. Simplified and realistic 3D human models are used in numerical simulations. In particular, 3D human models that can be studied with a 2D equivalent simulation maintaining all the features of the original human models are considered. The 2D simulations allow to use a software to compute the 2D solutions to take as reference solutions to better understand the causes of numerical artifacts and to define an exposure scenario in which the unique source of numerical artifacts is the discretization of the models.

The scalar potential finite difference (SPFD) method using the electric scalar potential as nodal unknowns, described in chapter 3, is used for both tetrahedral and voxelized discretization to solve the low-frequency numerical dosimetry problems analyzed in this chapter.

5.2 Construction of comparable tetrahedral and voxel-based meshes

Having tetrahedral and voxel-based meshes comparable to each other from a geometric point of view is a fundamental prerequisite for making a fair comparison between the

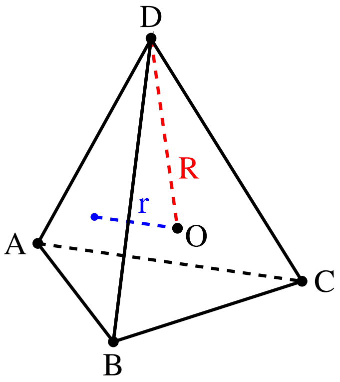

Figure 5.2: Tetrahedron with center O: the inradius r and the circumradius R are respectively drawn in blue and red.

results obtained with the two different type of discretizations.

In the numerical simulations, that will be analyzed in this chapter, the tetrahedral meshes are created by using a commercial software setting a uniform mesh size. The regular cubic discretizations with the desired resolution (1 mm or 0.5 mm) have always been generated from these tetrahedral meshes. In order to do this, a box which contains the tetrahedral elements is created starting from the coordinates of the minimum point and maximum one of the tetrahedral mesh. Subsequently the nodes of the voxel-based mesh are identified by dividing each edge of the box *n times* according to the desired size of the cubic elements. Each voxel of the uniform grid is assigned the same tissue type of the tetrahedron in which the barycenter of the voxel is contained. In this way the tetrahedral and voxel-based meshes are as similar as possible. Finally, the voxels of the box that do not contain tetrahedral elements are eliminated.

5.2.1 Tetrahedral mesh quality

A good mesh quality is an important prerequisite to ensure numerical results in agreement with the reference solution. The best quality mesh is achieved when it is uniformly composed of perfect elements with equal length edge size, i.e. regular polygons in two-dimensional space and regular polyhedra in three-dimensional space.

The mesh quality issue does not arise when voxelized-human models are used in numerical dosimetry because the meshes are discretized with uniform cubic elements with the same size along each edges. On the other hand, the purpose of tetrahedral meshes is to reproduce the object shape in the best possible way. Because of the presence of small edges, curved geometry, thin features and sharp corners, tetrahedra with much longer edges than others can be found in the same mesh discretization. If from a geometric point of view this guarantees a better reproduction of the object shape, from a computational point of view this greatly affects the numerical accuracy.

The shape of tetrahedra is usually assessed via aspect ratios, which consist of fractions determined by dividing length of edges, altitudes, etc. In our studies, the quality q of tetrahedral meshes is evaluated by using the Normalized Shape Ratio (NSR), as described in [66], given by the formula

$$q = 3\frac{r}{R}, \tag{5.1}$$

where r is the inradius of a tetrahedron, i.e. the distance from the center of the tetrahedron to the center of a face, while R is the circumradius of a tetrahedron, i.e. the distance from the center of the tetrahedron to a vertex (see Fig. 5.2). (5.1) can be obtained by considering the fact that in a regular tetrahedral element the two radii are related to each other by

$$\mathrm{R = 3r.}$$

If the aspect ratio between r and R is considered, we obtain

$$\frac{r}{R} = \frac{r}{3r} = \frac{1}{3}. \tag{5.2}$$

The Normalized Shape Ratio formula (5.1) is obtained by normalizing (5.2), that is

$$1 = \frac{\frac{r}{R}}{\frac{1}{3}} = \frac{r}{R} \cdot 3 = q. \tag{5.3}$$

From (5.3), it can be deduced that the NSR of a perfect tetrahedron is equal to 1. This means that a mesh composed of tetrahedra with Normalized Shape Ratio very close to 1 can be considered a good quality mesh.

5.3 Multilayered sphere

In order to see if the use of tetrahedral meshes in numerical dosimetry could make sense, an analytical reference solution to which compare the numerical results obtained by

Table 5.1: Multilayered sphere structure.

Layer	Tissue	Radius (mm)	Conductivity (S/m)
1	Skin	80	0.0002
2	Fat	76	0.043
3	Muscle	74	0.34
4	Skull	72	0.02
5	Muscle	68	0.34
6	Cerebrospinal fluid	66	2.0
7	Brain	64	0.11
8	Cerebrospinal fluid	42	2.0
9	Brain	38	0.11

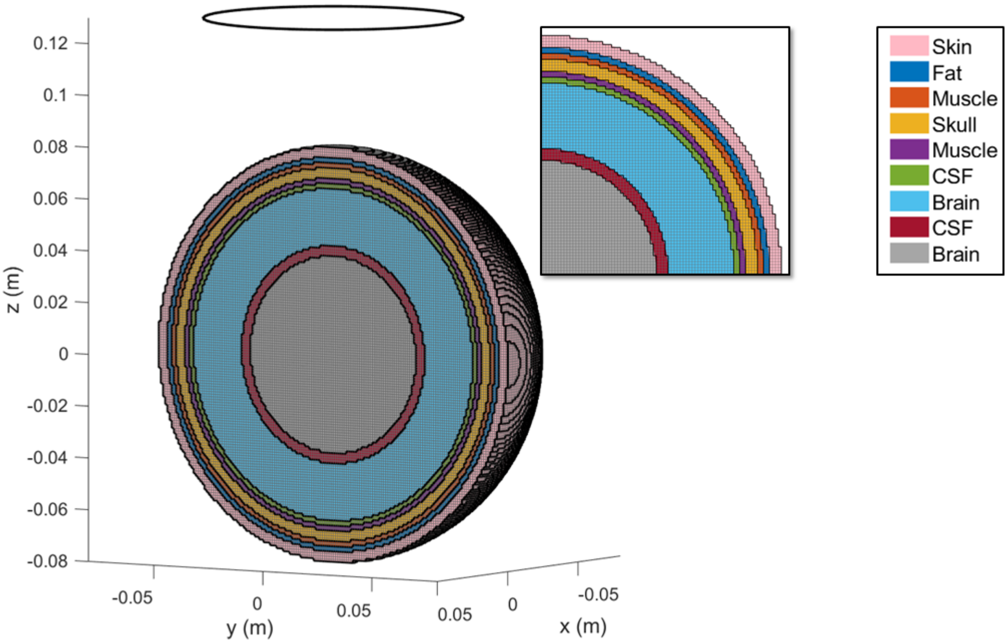

Figure 5.3: Exposure scenario of the multilayered sphere. The various layers are highlighted by different colors. In the insert the stair-casing effect due to the voxel-discretization is showed.

using tetrahedral and voxel-based models was necessary. For this reason, a multilayered sphere, which represents a simplified head, exposed to a quasi-static magnetic field was considered as benchmark case and the analytical reference solution [67] was computed by using Maxwell's equations described in chapter 3.

5.3.1 Exposure scenario

A coil with radius of 5 cm is located 13 cm above the center of the multilayered sphere, as shown in Fig. 5.3. The axis of the coil is the z-axis and the origin of the reference system corresponds to the center of the sphere. The operating frequency is 50 Hz and the current flowing through the coil is 1 kA. The multilayered sphere structure is taken from [36] and it consists of nine layers whose geometry and tissue properties are described in Tab. 5.1. No considerations on the conductivity of the skin are made since the sphere is used as the first investigation of the proposed approach and it can be considered as a simplified human head, but it is not a realistic one.

In the tetrahedral mesh the number of nodes is about 323600 and of tetrahedra is 1883300. The corresponding voxel-based mesh is generated with a resolution of 1 mm and in the voxelized model there are 2205000 nodes and 2144100 voxels.

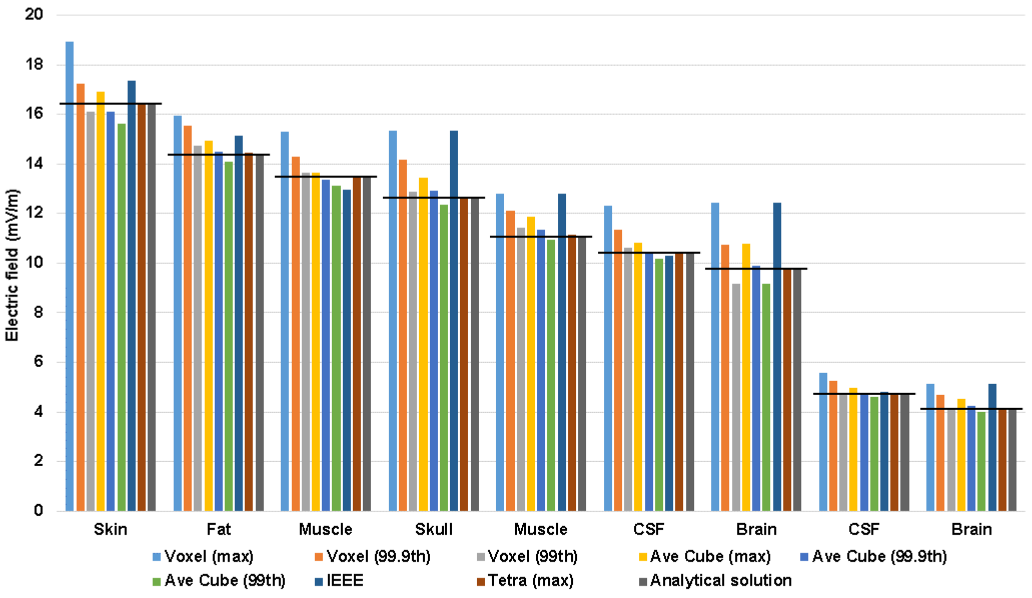

Figure 5.4: Comparison for each tissue between the electric field values of the analytical solution with the maximum values obtained in the tetrahedral mesh and the values obtained in the voxelized discretizations with and without post-processing techniques. "Ave Cube" refers to the electric field averaged over a $2 \times 2 \times 2$ mm^3 cube.

Table 5.2: Deviation between analytical and computed induced electric field on tetrahedral and voxel-based mesh.

Tissue	**Analytical solution (mV/m)**	**Voxel**							**Tetra**
		raw data 1 mm^3			**averaging over $2 \times 2 \times 2$ mm^3 cube**				
		max	**99.9th**	**99th**	**max**	**99.9th**	**99th**	**IEEE**	**max**
Skin	16.38	1.1563	1.0534	0.9844	1.0333	0.9837	0.9541	1.0609	1.0051
Fat	14.37	1.1104	1.0804	1.0265	1.0383	1.0075	0.9812	1.0544	1.0050
Muscle	13.47	1.1344	1.0618	1.0114	1.0143	0.9921	0.9733	0.9631	1.0034
Skull	12.63	1.2132	1.1223	1.0192	1.0657	1.0217	0.9784	1.2132	1.0026
Muscle	11.11	1.1524	1.0910	1.0294	1.0682	1.0200	0.9833	1.1524	1.0041
CSF	10.40	1.1836	1.0916	1.0187	1.0414	1.0021	0.9775	0.9879	1.0051
Brain	9.78	1.2699	1.0971	0.9373	1.1026	1.0112	0.9364	1.2699	1.0022
CSF	4.76	1.1721	1.1001	1.0016	1.0410	1.0017	0.9659	1.0051	0.9988
Brain	4.12	1.2389	1.1284	0.9878	1.0926	1.0291	0.9629	1.2389	1.0015

5.3.2 Numerical results

The induced electric field is computed using the numerical method described in chapter 3 for both tetrahedral and voxel-based mesh.

The only source of numerical artifacts, which occurs in this exposure scenario, is the stair-casing approximation error (for the voxel mesh). In fact, thanks to the symmetry of the exposure scenario, the induced currents are forced to circulate within a single tissue. Hot spots due to field singularity and/or high contrast between conductivities of contiguous tissues are avoided.

Fig. 5.4 compares for each tissue the maximum electric field values of the analytical solution with the ones evaluated on both meshes with the different approaches. In particular, post-processing techniques, described in paragraph 2.4.1, are applied in the voxelized model in order to suppress numerical artifacts, while in the tetrahedral mesh the maximum values are considered without any filtering metrics.

In Tab. 5.2 the deviation from the analytical solution, computed by dividing each value obtained in the numerical simulations by the related analytical reference one, is reported for each tissue. Due to the coil position, the maximum exposure is in the outermost layer (skin). In this tissue, in the voxel-based mesh the maximum value of the electric field evaluated without post-processing techniques overestimates the exposure by 15%, the 99.9th percentile overestimates the exposure by 5% and the 99th percentile underestimates the exposure by 2%. In the tetrahedral mesh, instead, the deviation is ~ 1.005, which means an overestimation of 0.5%, which is a very good approximation for a low-frequency numerical dosimetry problems. Looking at the results also in the other tissues, we can see that the values obtained over the tetrahedral mesh are one order of magnitude lower than the others. This means that in this exposure scenario the maximum induced electric field values computed on the tetrahedral mesh provide results very close to the analytical solution for each tissue without the need to apply any filtering techniques.

The other results in Fig. 5.4 and Tab. 5.2 refer to the voxel-based mesh: the 99th and the 99.9th percentiles along with the maximum values obtained by averaging the induced electric field over a $2 \times 2 \times 2$ mm^3 cube are reported together with the ones obtained with the IEEE approach. We can see that the 99.9th percentile values applied to the electric field averaged over a $2 \times 2 \times 2$ mm^3 cube are in better agreement with the analytical values than the ones obtained following the ICNIRP guidelines (which, as we have mentioned earlier, suggest to take the 99th percentile value of the averaged electric field over a $2 \times 2 \times 2$ mm^3 cube). On the other hand, the IEEE approach does not provide good results. Furthermore, it can be seen that the solution obtained with the tetrahedra better approximates the exact solution even with respect to the results obtained with the filtering techniques in the voxelized meshes.

Since the purpose of this study is not to compare the various post-processing techniques in the voxelized models, but to identify the source of numerical artifacts produced by tetrahedral meshes in realistic exposure scenarios, hereinafter only the 99th percentile and the 99.9th percentile along with the maximum values of the induced electric field

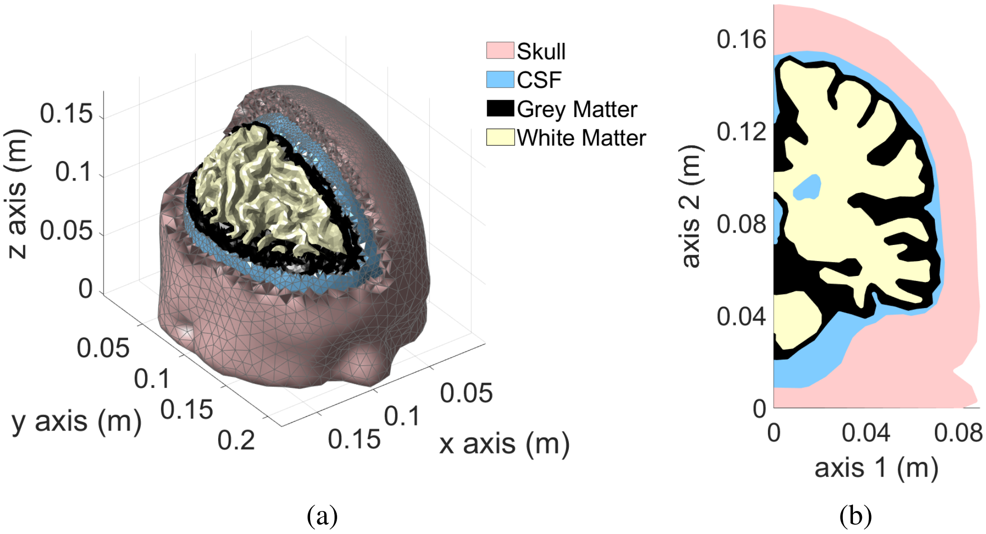

(a) (b)

Figure 5.5: Colin27 Average Brain: 3D model (a) and 2D cut-plane (b).

strengths (raw data) are computed and analyzed for both meshes.

5.4 Human head model: Colin27 Average Brain

In order to compare the results of tetrahedral and voxel discretization against a more challenging model, the realistic human adult head *Colin27 Average Brain* (also known as Average Colin) is considered. It is an adult brain atlas [68], that consists of four tissues: skull, cerebrospinal fluid (CSF), grey matter (GM) and white matter (WM). This atlas was obtained by scanning Colin J. Holmes brain 27 times (hence the name Colin27), in the course of few months. The images were combined to create an average brain with high structure definition. In this model the tetrahedral mesh was created by Qianqian Fang (more information can be found in [69]) and it is freely available for download [70]. The model is shown in Fig. 5.5a.

The tissue conductivities are assigned to each tissue in this wat: skull 0.02 S/m, cerebrospinal fluid 2 S/m, grey matter 0.02 S/m and white matter 0.02 S/m. The operating frequency is 50 Hz.

5.4.1 Exposure scenarios

Colin27 head model exposure is analyzed in two scenarios: 1) a homogeneous magnetic flux density with a single component in the z-direction of 200 μT, that corresponds to the reference level for public exposure, according to the [5], and 2) a localized exposure generated by a coil with radius of 20 cm. The coil is located 30 cm in front of the 3D

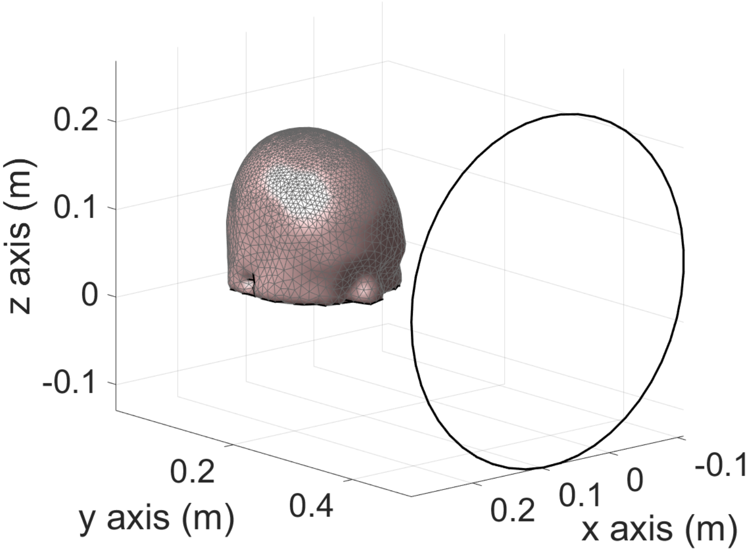

Figure 5.6: Localized exposure scenario of Colin27 3D model.

model and its center is aligned with head center (see Fig. 5.6). The current flowing through the coil is 1 kA.

The tetrahedral mesh quality is computed by using (5.1) and it is shown in Fig. 5.7. It is possible to notice a large number of tetrahedral elements with Normalized Shape Ratio (NSR) index close to 1, which means tetrahedra with a good quality shape (very close to a regular tetrahedron). However, elements with a low quality index exist. The voxel-based meshes with resolution of 1 mm e 0.5 mm are generated from the tetrahedral one, as described in paragraph 5.2. In the tetrahedral mesh the number of nodes is about 70200 and of tetrahedra is 423400; in the voxel-based one, instead, there are about 4140000 nodes and 4045000 elements when the resolution is 1 mm, and about 32753000 nodes and 32374000 elements when the resolution is 0.5 mm.

5.4.2 Numerical results

Fig. 5.8 shows the distribution of the electric field for all meshes and for all four tissues in the case of localized exposure. The maps of the electric field are in good agreement to each other and it is evident that the maximum exposure is in the front of the head, where the coil is located.

The 99th percentile and the 99.9th percentile along with the maximum values of the induced electric field strengths are computed and analyzed for voxels and tetrahedra in both exposure scenarios. Fig. 5.9 shows the results obtained on tetrahedral mesh and voxelized models with different resolutions in the uniform (Fig. 5.9a) and localized exposure (Fig. 5.9b) for each tissue. In general, a good agreement between the different meshes in the computed values is observed up to the 99.9th percentile, after which they

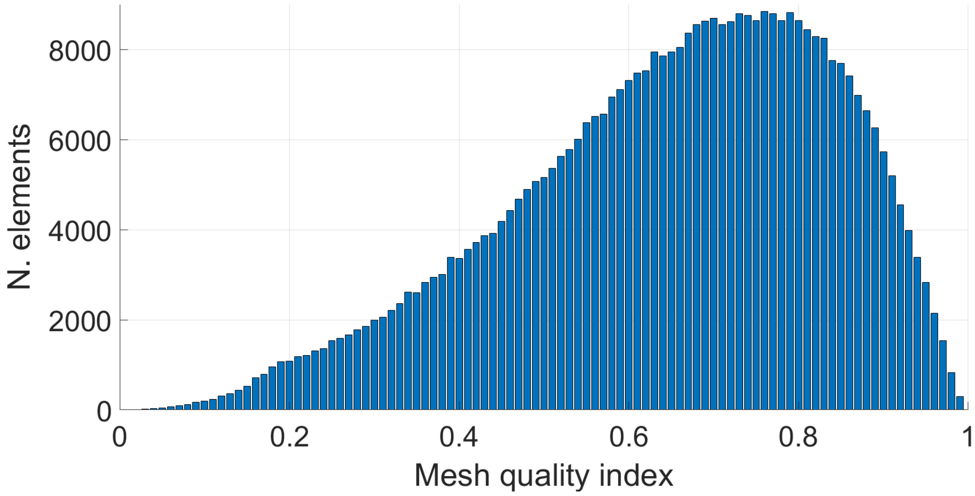

Figure 5.7: Tetrahedral mesh quality of Colin27 3D model. The Normalized Shape Ratio (NSR) indices are on the x-axis, while the number of tetrahedral elements corresponding to the respective mesh quality index is shown on the y-axis.

diverge with a rapid increase in the electric field strength until reaching the maximum value. This trend is observed in all tissue and in all meshes.

The induced electric field exhibits higher values in the skull and grey matter in both exposure scenarios. In particular, we can observe that the maximum electric field values evaluated in the finest voxel-based mesh are higher than those computed in the coarsest one for almost all tissue. This is caused by the stair-casing approximation errors that make the maximum electric field value unreliable especially at the boundaries with high electrical conductivity contrast.

In the case of homogeneous exposure, in Fig. 5.9a it is possible to observe that the maximum value obtained with the tetrahedral mesh is always lower than the one obtained with the voxels. However, in the more realistic localized exposure this result is not confirmed for all tissues. In the cerebrospinal fluid (CSF) and in the white matter (WM) the maximum values obtained in the tetrahedral mesh exceed those of the voxelized models. In particular, in the white matter of the tetrahedral model there is a rapid increase in the electric field strength after the 99.9th percentile.

Through a local and deep analysis of these electric field peaks, we have found out that the Normalized Shape Ratio index related to the tetrahedron with the maximum electric field value is equal to 0.9 in the cerebrospinal fluid (see Fig. 5.10a), while it is equal to 0.11 in the white matter (see Fig. 5.10b). This means that, while in the white matter the numerical artifact is caused by the irregular shape of the tetrahedron, the same cannot be said to happen in the CSF. Here, in fact, the tetrahedron has a regular shape, but it is located on the boundaries of a tissue with high electrical conductivity contrast (2 S/m in the CSF, 0.2 S/m in the other tissues). In this case, the induced currents cross tissue

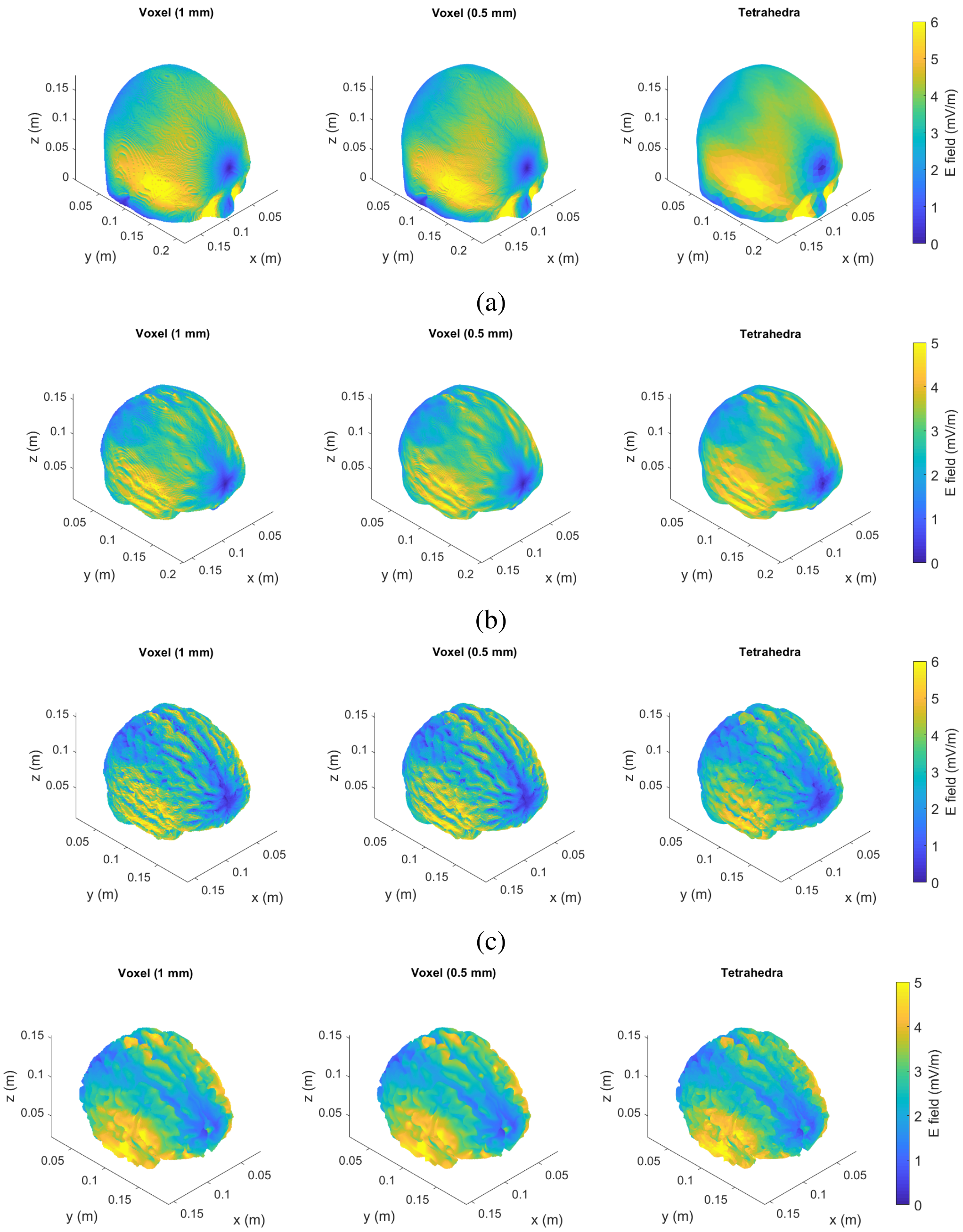

(a)

(b)

(c)

(d)

Figure 5.8: Localized exposure (coil in front of the head model). The induced electric field in Colin27 Average Brain is shown for tetrahedral mesh and voxel-based meshes with resolution of 1 mm e 0.5 mm in each tissue: skull (a), CSF (b), grey matter (c) and white matter (d).

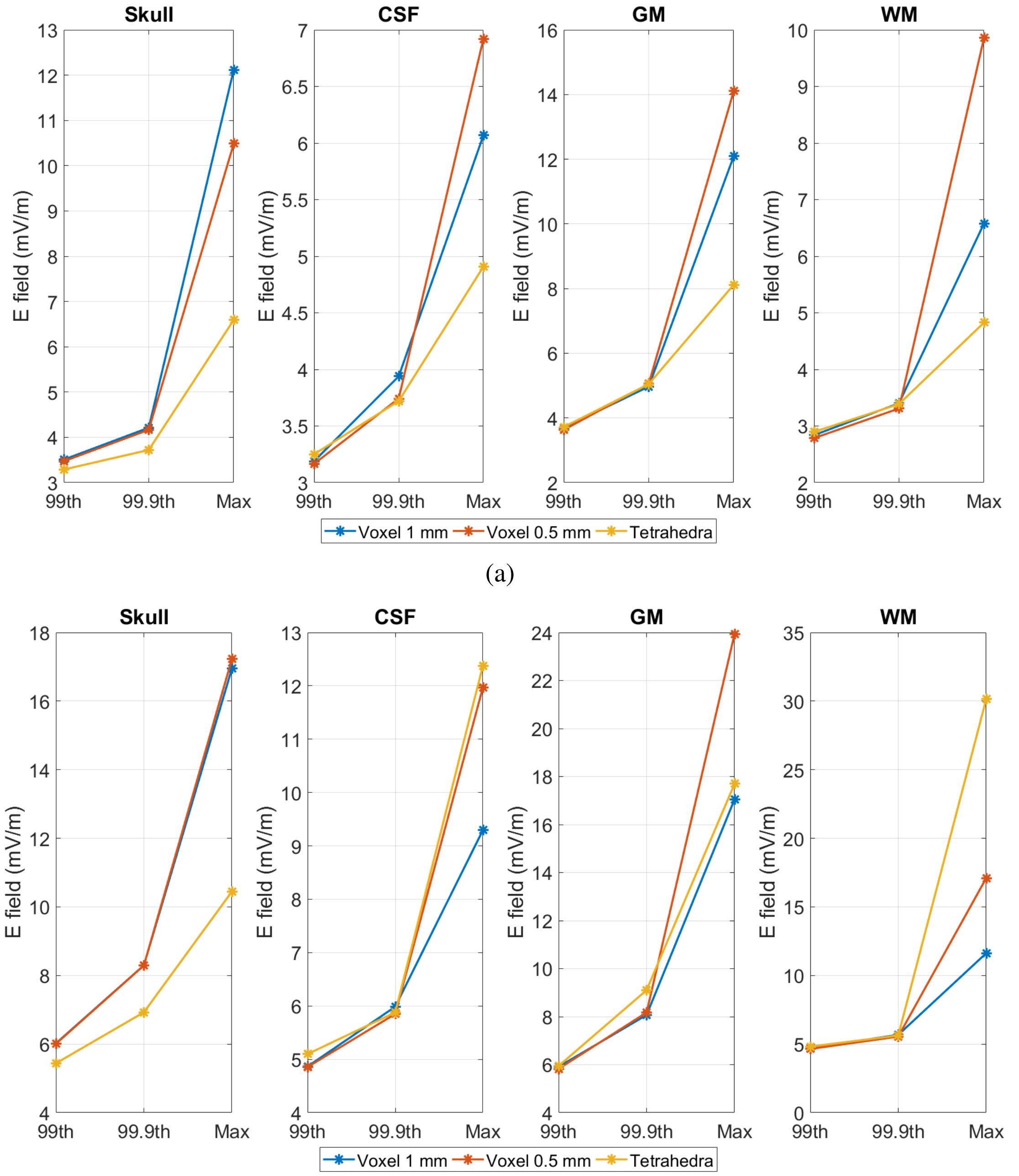

(a)

(b)

Figure 5.9: The 99th percentile, the 99.9th percentile and the maximum electric field values for each tissues of tetrahedral and voxel-based meshes with different resolutions. Uniform exposure along z-axis to 200 μT magnetic flux density at 50 Hz (a). Localized exposure due to a coil located 30 cm in front of Colin27 head center (b).

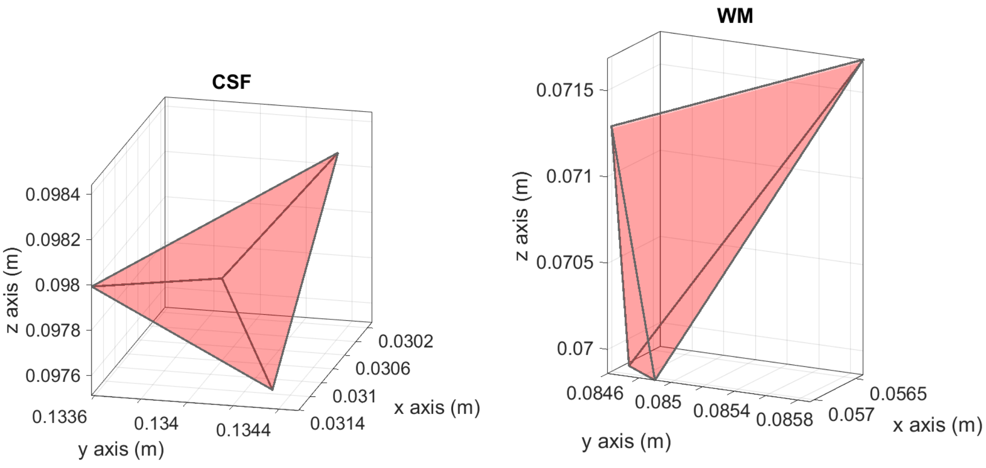

(a) (b)

Figure 5.10: Shape of the tetrahedron with the maximum electric field value in CSF (a) and white matter (b).

boundaries and cause numerical artifacts due to the difference in conductivities between adjacent tissues (tissue contrast).

This means that, when stair-casing approximation errors are not the only source of numerical artifacts, also tetrahedral meshes are subject to numerical artifacts that require to be filtered out. By eliminating the tetrahedra in which there is the maximum exposure and considering the 99.9th percentile, we obtain electric field values in agreement with the corresponding values evaluated on the voxelized models. Overall, by applying the 99.9th percentile and the 99th percentile to all meshes, the results are in good agreement, i.e the deviation is fully within the uncertainty related to the tissue properties.

5.5 Planar and axisymmetric models of Colin27 Average Brain

To better understand the source of numerical artifacts to which a tetrahedral mesh can be subject, we created two simplified 3D models starting from a cut-plane of Colin27 brain model, that is shown in Fig. 5.5b. The cut-plane is used to define a planar and an axisymmetric model. The planar 3D model is obtained by mirroring the cut-plane with respect to the axis 2 and by extruding the result by a thickness of 2 mm along z-axis. The axisymmetric 3D model is obtained by rotating the cut-plane along the longitudinal axis (axis 2 of the figure) by 360°. The two simplified 3D models are shown in Fig. 5.11.

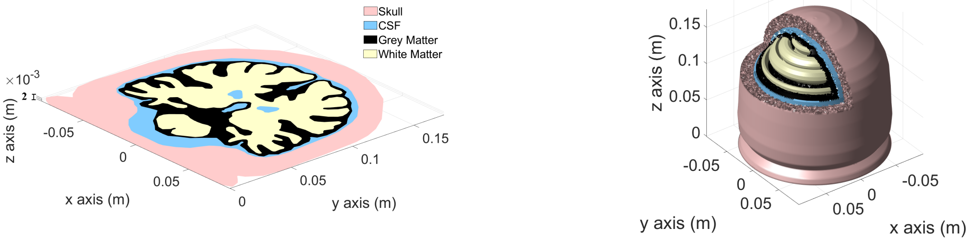

(a) (b)

Figure 5.11: Planar model (a). Axisymmetric model (b).

5.5.1 Exposure scenarios

Both models are exposed to a homogeneous magnetic flux density of 200 μT with only z-component. This means that in the planar 3D model the external field is orthogonal to the xy plane and parallel to the extrusion direction, while in the axisymmetric 3D model the field is parallel to the axis 2 and it is a uniform vertical field.

These simplified models have the advantage that they can be simulated as a 2D planar and 2D axisymmetric problem. The 2D solutions obtained with a very fine mesh are used as reference solutions for the 3D simulations, making it possible to understand the causes of the numerical artifacts.

The tetrahedral and voxel-based meshes of both 2D models are created as described in paragraph 5.2. In particular, the tetrahedral meshes of the planar and axisymmetric 2D models were all manually checked before starting the tests and local edits were made where needed in order to ensure a good quality mesh. In addition, in the planar case the tissue boundaries were smoothed to try to avoid numerical artifacts due to the presence of singularities, as Fig. 5.12 shows.

Subsequently, the 3D models corresponding to the planar and axisymmetric case were created with both voxel (1 mm and 0.5 mm side) and tetrahedral elements to perform 3D simulations.

5.5.2 Numerical results

For all tissues the maximum value (raw data), the 99.9th percentile and the 99th percentile are presented for voxelized 3D models, while only the maximum electric field value is considered for tetrahedral meshes. All values are normalized with respect to the corresponding values obtained with the 2D models (reference solution).

Tab. 5.3 and Tab. 5.4 show that the induced electric field computed on the tetrahedral meshes without the need to apply any filtering techniques provides results very close to the reference solution in the axisymmetric and planar case respectively. It is apparent from Tab. 5.3 that the tetrahedral mesh is able to remove the stair-casing approximation

(a) (b)

Figure 5.12: Manual control of the tetrahedral mesh: the boundaries were smoothed to avoid singularities. Tissue boundaries before local smooth edits (a). Tissue boundaries after local smooth edits (b).

errors: the largest deviation with respect to the reference solution, in fact, is ~ 1.003, that means an overestimation of 0.3%, which represents an excellent result in numerical dosimetry. It is worth noting that in the axisymmetric case the tetrahedral model is not subject to other source of numerical artifacts. This is due to the manual local edits made in the tetrahedral mesh to ensure a good quality and to the fact that in the axisymmetric case the induced currents do not cross tissue boundaries thanks to the symmetry of the problem (as in the case of the multilayered sphere). This means that the main cause of numerical artifacts in both voxelized models is due to the stair-casing approximation errors.

On the contrary, in the planar case the induced currents cross tissue interfaces, hence numerical artifacts are not only due to stair-casing approximation errors, but they are also caused by the contrast of conductivities between contiguous tissues (effect known as tissue contrast). Tab. 5.4 shows that in the planar case the maximum exposure is in the grey matter. In this tissue the use of tetrahedral elements causes an underestimation of about 7% (more than acceptable in numerical dosimetry), while the underestimation caused by the use of voxel elements is even higher, up to 50% when the 99th percentile is applied.

5.6 Human head model: VHP-Female Phantom

In previous paragraphs it has been pointed out that, even though tetrahedral meshes are not affected by stair-casing approximation errors, they are subject to other sources of numerical artifacts. These numerical artifacts can be due to a mesh with low quality elements and/or to the effect known as tissue contrast effect.

Table 5.3: Deviation of the electric field in the axisymmetric case.

Tissue	**reference 2D (mV/m)**	**Voxel 1 mm**			**Voxel 0.5 mm**			**Tetra**
		max	**99.9th**	**99th**	**max**	**99.9th**	**99th**	**max**
Skull	2.79	1.372	1.149	1.018	1.263	1.111	0.994	1.002
CSF	2.31	1.484	1.208	1.100	1.283	1.152	1.062	1.003
Grey Matter	2.26	1.509	1.279	1.110	1.438	1.225	1.050	1.001
White Matter	2.12	1.025	1.002	0.975	1.010	0.998	0.975	1.003

Table 5.4: Deviation of the electric field in the planar case.

Tissue	**reference 2D (mV/m)**	**Voxel 1 mm**			**Voxel 0.5 mm**			**Tetra**
		max	**99.9th**	**99th**	**max**	**99.9th**	**99th**	**max**
Skull	6.88	1.086	0.854	0.596	1.053	0.738	0.564	1.092
CSF	6.19	1.004	0.986	0.623	1.039	0.866	0.671	1.098
Grey Matter	11.06	0.805	0.694	0.500	0.769	0.610	0.452	0.934
White Matter	4.68	1.045	0.978	0.894	1.018	0.925	0.843	1.006

Starting from these considerations, further studies were made by using the VHP-Female Computational Phantom v2.1 (or VHP Female College v2.1 [71]). It is a platform-independent full-body human phantom constructed by NEVA Electromagnetics LLC and supported by the ECE Department at Worcester Polytechnic Institute. The woman's body was donated by her husband after her death at the age of about 60. The phantom tissues are all extracted from the Visible Human Project® (VHP)-Female open-source image dataset of the U.S. National Library of Medicine and the data are freely available for download [72].

In our analysis, we do not have considered the whole body, but only the head by cutting it obliquely at the neck. Its section is shown in Fig. 5.13 and, for sake of simplicity, we call it VHP-Female head model. The tissue conductivities are assigned to each tissue according to the IT'IS Foundation database [14]. Values are calculated at the reference frequency of 50 Hz.

5.6.1 Exposure scenario

The VHP-Female head model is exposed to a uniform magnetic exposure at the general public reference level of 200 μT ([5]).

The tetrahedral meshes are created by using a commercial software setting a uniform mesh size and the voxelized models with resolution of 1 mm is created as described in paragraph 5.2, in order to have meshes as similar as possible. In the tetrahedral mesh the number of nodes is about 500000 and of tetrahedra is 3000000, while in the voxel-based one, instead, there are about 4650000 nodes and 4546000 elements.

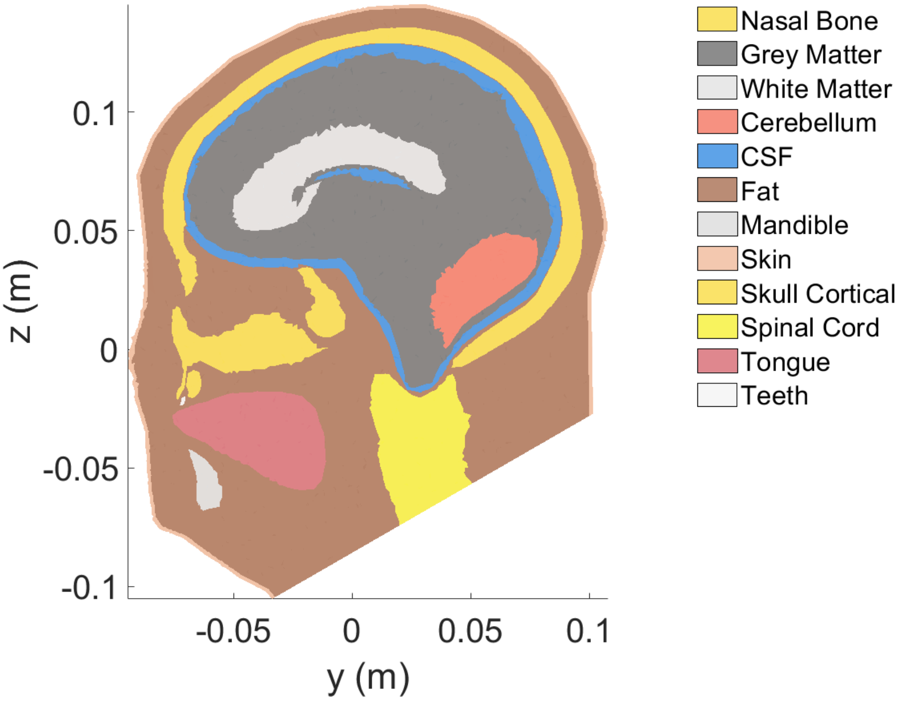

Figure 5.13: Section of VHP-Female Computational Phantom.

The tetrahedral mesh quality is computed by using (5.1) and it is shown in Fig. 5.14. It is possible to notice that most of the tetrahedral elements have a Normalized Shape Ratio (NSR) index close to 1, which means tetrahedra with a good quality shape (very close to a regular tetrahedron). However, there is a limited number of tetrahedra with a very low mesh quality index (between about 0.2 and 0.3). In order to see how this could affect the numerical results, no local edits are made to the tetrahedral mesh.

5.6.2 Numerical results

In Fig. 5.15 the induced electric field distributions evaluated on the tetrahedral and voxelized models are reported. From an overall point of view, the two distributions are completely comparable to each other. However, if we analyze the maximum values of the induced electric field in each tissue, the numerical artifacts make these values unreliable and filtering techniques are necessary (see Fig. 5.16).

The maximum exposure is registered in the grey matter (GM), in the fat and in the skin. In particular, in the grey matter and in the fat the maximum value of the induced electric field evaluated in the tetrahedral model exceeds the corresponding one in the voxel-based meshes, as it happens in the tongue. A rapid increase in the electrical field strength is observed in these tissues after the 99.9th percentile in the tetrahedral mesh. These peaks are caused by low quality tetrahedra. Fig. 5.17 shows that the tetrahedron with the maximum electric field value has an irregular shape for each of these tissues. This fact is confirmed by computing the Normalized Shape Ratio index: in fact, it is equal to 0.001 in the grey matter, to 0.0002 in the fat and to 0.09 in the tongue.

For this reason, since it is always impossible to evaluate an analytical solution in a real exposure scenario, it is really important determining a reference solution, to which the results can be compared. According to paragraph 2.4.1, the induced electric field of the voxelized model was averaged over a contiguous tissue volume of $2 \times 2 \times 2$ mm^3. Then, based on the ICNIRP guidelines [5], the 99th percentile is considered. Nevertheless, since in some cases the 99th percentile tends to underestimate the maximum electric field strength, the 99.9th percentile of the averaged electric field is taken as reference solution.

Fig. 5.16 compares to each other the 99th percentile, the 99.9th percentile and the maximum electric field values of the most significant head tissues for tetrahedral and voxelized models (with and without the averaging over a $2 \times 2 \times 2$ mm^3 cube). As expected, the averaged electric field tends to mitigate for all the tissues the computational errors in the voxel-based mesh. It is worth noting that the tetrahedral values up to the 99.9th percentile are in good agreement with the reference ones, while after this percentile they suffer from numerical artifacts. As said previously, the peaks of the induced electric field of the tetrahedral mesh are caused in some tissues by low quality tetrahedra, while in the others by a strong tissue contrast due to the induced currents that cross tissue interfaces with high electrical conductivity contrast. However, if filtering techniques are applied, we can say that the induced electric field evaluated over a tetrahedral mesh is comparable with the reference solution.

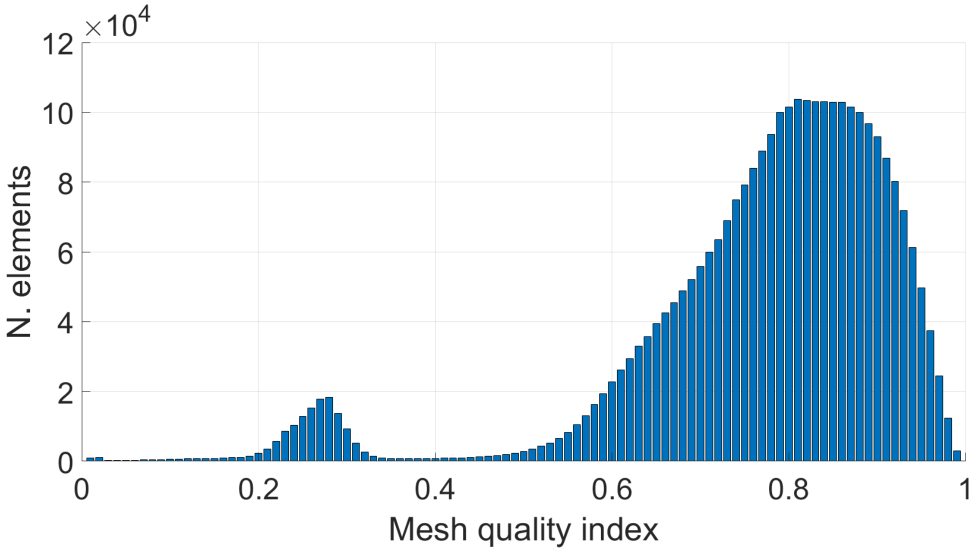

Figure 5.14: Tetrahedral mesh quality of VHP-Female head model. The Normalized Shape Ratio (NSR) indices are on the x-axis, while the number of tetrahedral elements corresponding to the respective mesh quality index is shown on the y-axis.

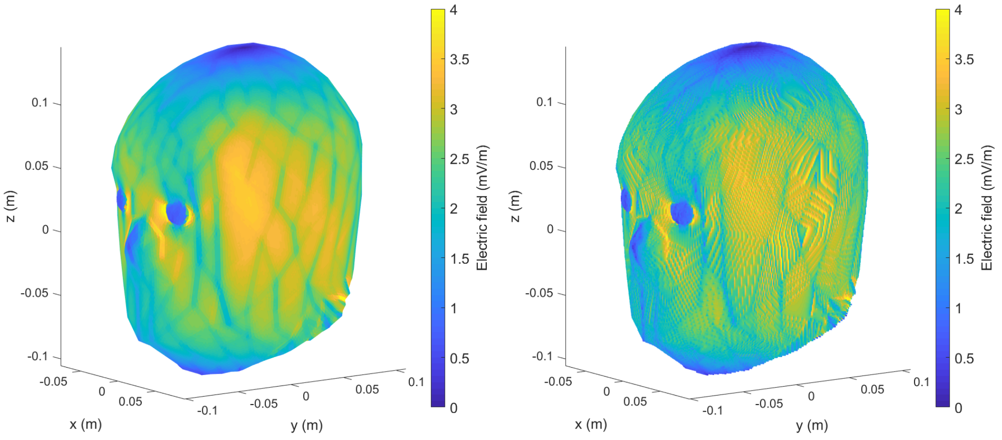

(a) (b)

Figure 5.15: Induced electric field distribution evaluated on the tetrahedral mesh (a) and on the voxelized model (b).

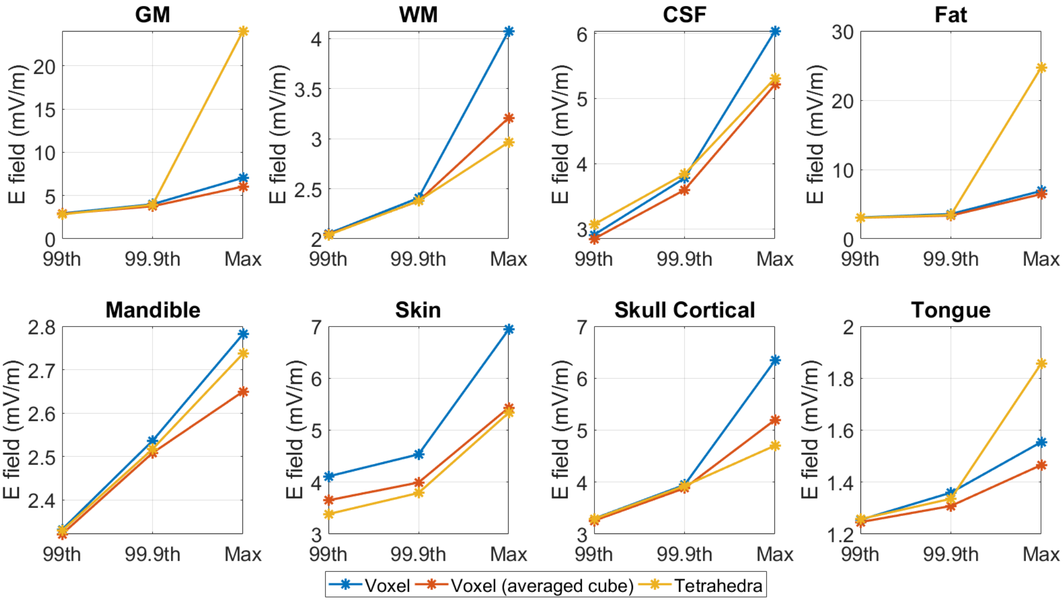

Figure 5.16: The 99th percentile, the 99.9th percentile and the maximum electric field values for each tissues of tetrahedral and voxel-based meshes. "Voxel (averaged cube)" refers to the values obtained by averaging the induced electric field over a $2 \times 2 \times 2\ \mathrm{mm}^3$.

5.7 Discussion

Several exposure scenarios have been analyzed in order to study if tetrahedral meshes are able to suppress numerical errors caused by the stair-casing approximation errors

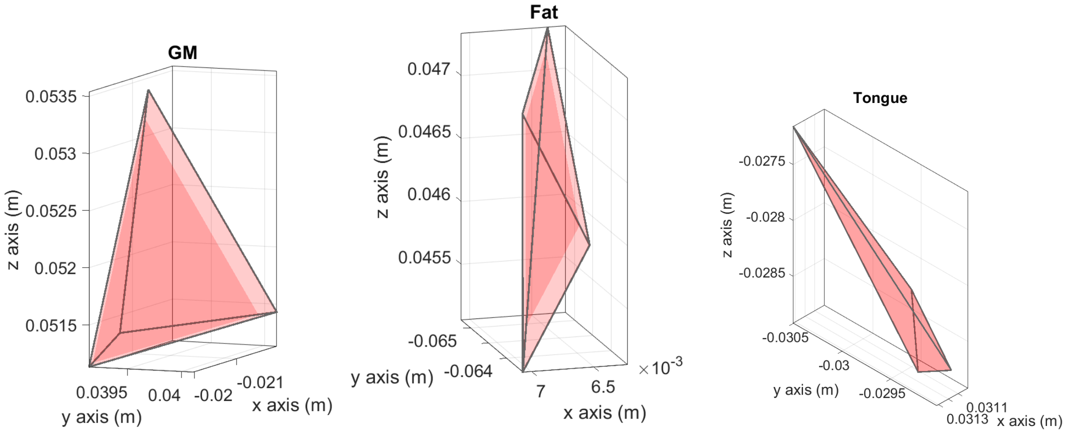

(a) (b) (c)

Figure 5.17: Shape of the tetrahedron with the maximum electric field value in grey matter (a), fat (b) and tongue (c).

in voxelized models when curved boundaries are approximated with voxels. From the analysis we found out that both voxelized and tetrahedral head models suffered from artifacts in the evaluation of the high electric field values. Tetrahedral meshes, in fact, are able to remove completely the source of computational artifacts related to the geometrical modelling of the computational domain, however, in a real exposure scenario, other sources of numerical artifacts are still present. These numerical artifacts are related to two fundamental factors: the tetrahedral mesh quality and the tissue contrast effect. If working on the quality of the mesh is possible, even if generating meshes totally consisting for equilateral elements is a challenging task (or even impossible for most geometries), it is almost impossible to avoid that in a real exposure scenario the induced currents do not cross the tissue interfaces. For this reason, the use of filtering techniques cannot be completely avoided also in human models discretized with tetrahedral meshes.

This conclusion is in agreement with the studies reported in [35]. In this paper, the authors performed computation using five 3D head models, whose tetrahedral and voxel-based meshes are generated from magnetic resonance images (MRI) with different resolutions. The reference solution was the one obtained with the smallest voxels (edge length of 0.25 mm), i.e. highest resolution. The quality of tetrahedral meshes were assessed by determining three metrics, which enable to evaluate whether an element is close to be a regular tetrahedron. Homogeneous and localized exposures were considered and they found out that both models were affected by computational errors in the evaluation of the highest electric fields.

As in our study, even the authors in [35] said that tetrahedral meshes are able to eliminate the numerical artifacts due to the stair-casing approximation errors typical in the voxelized models, but other source of artifacts are present and filtering techniques are still required. However, unlike what we have done through this chapter, they did not provide a rigorous method to identify the source of these numerical artifacts and the situations in which they occur. They focused their attention on the tetrahedral mesh quality, stating that poorly-shape elements produce artifacts that make the maximum electric field unreliable and concluding that the numerical artifacts in tetrahedral models are mainly caused by low quality tetrahedra.

Chapter 6

Modeling of low-frequency electromagnetic fields exposure in arbitrary posture

As we have seen so far, numerical dosimetry is fundamental for the evaluation of human exposure to low-frequency electromagnetic fields. The accurate modeling of the electromagnetic field source and the exact posture of the human body play a fundamental role for the assessment of human exposure.

The problem of performing numerical dosimetry starting from data coming from general purpose software or real measurements, i.e. when no information is available about the source, was described in chapter 4 and a comparison between two methods that allow to evaluate the magnetic vector potential starting from the knowledge of the magnetic flux density has been done. In this chapter the focus shifts on the posture of the human model.

In the classical approach, in fact, all dosimetric computations are performed with a human phantom postured in the exact position to ensure a correct assessment of human exposure. However, there are situations (e.g. in the workplace) in which the position of the human body is known only approximately and the source of the electromagnetic field must be characterized in realistic conditions. For this reason, a new approach based on the evaluation of the human exposure to electromagnetic fields by using a non-postured human model through a source term transformation is proposed. Some results have been published in [73], while further studies conducted on a whole-body female human model will be analyzed in the following for the first time. Furthermore, this project has been funded by the Programme National de Recherche Environnement-Santé-Travail (PNREST) Anses, 2018/1/242.

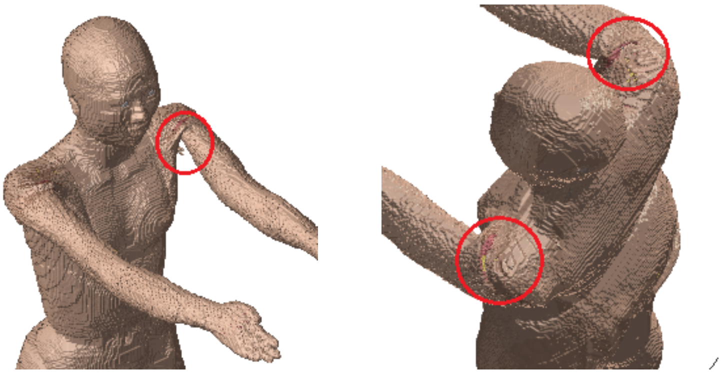

Figure 6.1: Example of artifacts obtained with the software NICTPoseTool. In the red circles an abnormal protuberance of the skin (a) and a discontinuity in the junction of the rotated shoulders (b) are highlighted.

6.1 The limits of postured human models

Although in these years several realistic and detailed anatomical whole-body models of different types of human beings (e.g., male, female, children, pregnant woman, and so on) have been developed (as discussed in paragraph 2.3) [21], [22], [23], [24] most of them are only available in the standing position with their arms along the sides. This fact limited the number of possible case studies because realistic exposure situations could not be reproduced. For this reason, postured human phantoms started to be used [25], [30] and software for posturing have been developed. Posture transformations are based on maintaining internal tissues and organ continuity. However, the operation of posturing a numerical human phantom is a time-consuming [74], [75], it introduces in any case a certain degree of approximation and it does not guarantee the respect of anatomical constraints (e.g. deformed bones and other artifacts), as shown in Fig. 6.1.

The proposed approach eliminates completely this step: a non-postured phantom is used in the numerical simulations and an equivalent deformation of the source term is done by maintaining the same level of approximation of the postured model.

6.2 Methods

The new method is based on carrying out all the numerical dosimetric simulations on a non-postured model in order to eliminate the problems related to the posture and to all the possible numerical artifacts deriving from the use of software for posturing.

This method is able to take into account the posture without deforming the human model. The idea of the new approach is based on performing a change of coordinates to apply not to the human model (as the existing methods and software do), but to the source term in order to avoid the posturing step and to create an equivalent source field that causes the same induced currents in the non-postured body. This change of variables is defined by the function $f : \mathbb{R}^3 \mapsto \mathbb{R}^3$ which maps the non-postured body Ω to the postured one Ω_p. Hereafter, the subscript p indicates quantities which depend explicitly on the posture of the body. It is possible to define the inverse function $f^{-1} : \mathbb{R}^3 \mapsto \mathbb{R}^3$ which takes back the postured phantom to the non-postured one. By applying this mapping to the Maxwell's equations that govern the low-frequency numerical dosimetry problems, only the materials properties used in these equations change, as described in [76].

Therefore, keeping all this in mind, the field transformation requires the use of a new tissue conductivity matrix and a new source term. This means that the algebraic formulation of the scalar potential finite difference (SPFD) method using the electric scalar potential as nodal unknowns, described in chapter 3, to solve the low-frequency numerical dosimetry problems can be rewritten as

$$\mathbf{G}^{\mathrm{T}}\mathbf{M}_{\sigma_{\mathrm{p}}}\mathbf{G}\varphi = -\mathrm{j}\omega\mathbf{G}^{\mathrm{T}}\mathbf{M}_{\sigma_{\mathrm{p}}}\mathbf{a}_{\mathrm{p}} \tag{6.1}$$

Computations performed by using (6.1) refer directly to the non-postured body, eliminating the posturing step. On the other hand, elements dependent on the effect of posture, i.e. tissue conductivity tensor $\mathbf{M}_{\sigma_{\mathrm{p}}}$ and the source term $\mathbf{a}_{\mathrm{p}}$, must be determined [77]. Considering the fact that the Jacobian matrix is linked to the applied transformation (more information can be found in appendix A), both quantities depend on the Jacobian matrix $\mathbf{J}_p$ of the map f

$$\mathbf{M}^{\mathrm{loc}}_{\sigma_{\mathrm{p}}} = \mathbf{J}_p^{-1}\mathbf{M}^{\mathrm{loc}}_{\sigma}\mathbf{J}_p^{-\mathrm{T}} \cdot \left|\mathbf{J}_p\right|; \qquad \mathbf{a}_p = \mathbf{J}_p^{\mathrm{T}}\mathbf{a}, \tag{6.2}$$

where $\mathbf{J}_p^{-\mathrm{T}}$ is the inverse of the transpose of the Jacobian matrix and $\left|\mathbf{J}_p\right|$ refers to the Jacobian determinant (or simply the Jacobian). In appendix B the reasoning that allows to obtain these quantities is reported. It is important to underline that $\mathbf{M}^{\mathrm{loc}}_{\sigma_{\mathrm{p}}}$ is locally computed and then the domain-based matrix $\mathbf{M}_{\sigma_{\mathrm{p}}}$ is assembled in a classical fem-like fashion, as described in chapter 3.

Because $\mathbf{a}_p$ depends on the Jacobian matrix of the transformation, it is important to pay attention when more than one transformation is applied to the human body in the numerical simulation. In this case, in fact, each transformation must be locally applied to portion of the body affected by the transformation, and in case of multiple transformations applied to the same part of the body, the Jacobian matrices of each transformation must be combined by a matrix multiplication because the postured human model is obtained from the composition of the transformations. It is worth underlying that the composition of transformations applied to the same part of the body does not enjoy the commutative properties.

6.3 Human body transformations

Generally speaking, geometric transformations are well known in computational electromagnetics [75], [77]. Movements that human body can perform are manifold: flexion, extension, rotation, abduction, adduction and circumduction. They have to be reproduced using geometric transformations when the postured phantom is created. The main geometric transformations that better reproduce human movements are translation, rotation, stretch and compression.

Translation and rotation belong to the isometry group, i.e. they are distance-preserving transformations between metric spaces. In particular, the Jacobian matrix of translation is the identity matrix. This means that in (6.2) it does not make any contribution and, so, the tissue conductivity matrix can be rewritten as

$$\mathbf{M}_{\sigma_\mathrm{p}}^{\mathrm{loc}} = \mathbf{M}_{\sigma}^{\mathrm{loc}}.$$

Instead, since rotation is a linear transformation, the rotation matrix coincides with the Jacobian matrix of the transformation. In particular, because of the fact that it is a direct isometry, its Jacobian matrix is orthogonal, i.e. $\mathbf{J}_p^{\mathrm{T}} = \mathbf{J}_p^{-1}$, and $|\mathbf{J}_p| = 1$. In most practical cases the local conductivity is isotropic, so $\mathbf{M}_{\sigma}^{\mathrm{loc}} = \sigma\mathbf{I}$, where $\mathbf{I}$ is the identity matrix. For this reason, the tissue conductivity tensor described in (6.2) can be rewritten as

$$\begin{aligned} \mathbf{M}_{\sigma_\mathrm{p}}^{\mathrm{loc}} &= \mathbf{J}_p^{-1}\mathbf{M}_{\sigma}^{\mathrm{loc}}\mathbf{J}_p^{-\mathrm{T}} \cdot |\mathbf{J}_p| = \mathbf{J}_p^{\mathrm{T}}\sigma\mathbf{I}\mathbf{J}_p \cdot |\mathbf{J}_p| \\ &= \mathbf{J}_p^{\mathrm{T}}\sigma\mathbf{I}\mathbf{J}_p = \sigma\mathbf{J}_p^{\mathrm{T}}\mathbf{J}_p = \sigma\mathbf{I} = \mathbf{M}_{\sigma}^{\mathrm{loc}} \end{aligned}$$

Therefore, we can conclude that in the rotation case the tissue conductivity does not change and only the source term undergoes a transformation.

Stretch and compression are usually not considered in the posture phantom creation because much more importance is given to maintain the internal tissues, organs continuity and mass rather than to introduce physiological concepts, such as muscle contraction. Moreover, in many cases, stretch and compression produce so small deformations that their transformation matrix is approximately equal to the identity one. In these cases the tissue conductivity matrix becomes

$$\mathbf{M}_{\sigma_\mathrm{p}}^{\mathrm{loc}} \simeq \mathbf{M}_{\sigma}^{\mathrm{loc}}.$$

In particular, it can be easily demonstrated that the error has the same order of the stretch or compression factor for small deformations when stretch or compression are along one direction.

In general, using (6.1) and (6.2) instead of (3.16) simplifies computations to a large extent. The key point is that in practice the transformation f can be approximated as a piecewise rigid motion and applied to the source field instead of the computational domain. In fact, when posturing human body, strong deformations are localized in articulations (elbows, knees, etc.): internal organs are only slightly deformed and brain is not deformed at all.

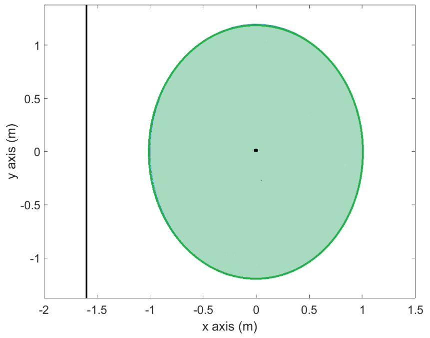

Figure 6.2: The ellipse exposure scenario in the 2D domain.

6.4 Dosimetric models

Three different dosimetric models are taken into account to test the new approach described in paragraph 6.2: one on a 2D domain and two on a 3D domain.

6.4.1 2D domain

The first study is carried out on a 2D domain Ω which consists of an ellipse with center in the origin of the reference system. The minor semi-axis is on the x-axis with length 1 m, while the major semi-axis is on the y-axis and it is 1.2 m long. The tests are performed by considering an infinite vertical wire along y as source field placed at a distance of 1.6 m from the center of the ellipse on the left-hand side. Fig. 6.2 shows the 2D exposure scenario. The operating frequency is 50 Hz and the current flowing through the wire is 1 kA.

6.4.2 3D homogeneous simplified phantom

In the 3D domain, for the sake of simplicity, a simplified phantom exposed to a quasi-static magnetic field is initially considered in order to compare the *in situ* electric field obtained by using the classical approach and the new one. It is composed of three regions (Fig. 6.3a): the torso, the arm, and the junction zone, which connects the arm to the torso. The torso is a parallelepiped with dimension $20 \times 10 \times 30\ \mathrm{cm}^3$, the junction is a cylinder with a 4 cm radius and 1 cm length, and the arm is formed by a cylinder equal to the junction connected to another cylinder with the same radius and 34 cm high. A uniform conductivity σ of 0.2 S/m is used.

A one-loop coil with radius of 15 cm is located 35 cm from the torso and it is centered in the center of the shoulder. The axis of the coil is the y-axis. The operating frequency is 50 Hz and the current flowing through the coil is 1 kA.

The tetrahedral mesh in the simplified phantom is created by using a commercial software and it consists of about 33000 nodes and 178000 tetrahedra (divided into about

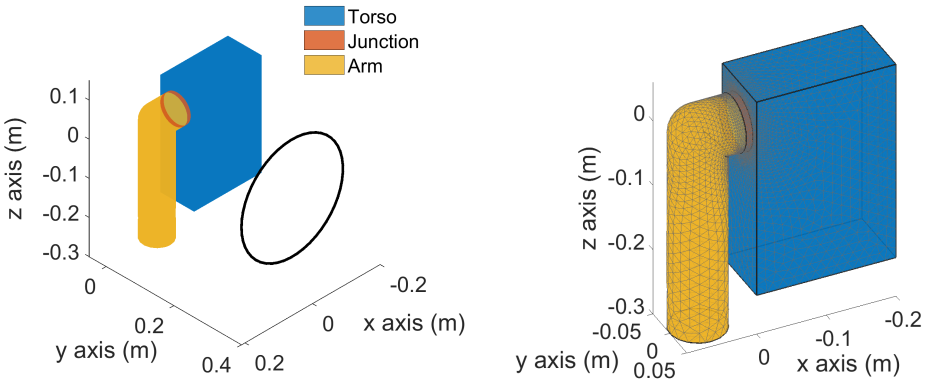

(a) (b)

Figure 6.3: The simplified phantom exposure scenario in the 3D domain: the three regions (torso, junction zone and arm) are highlighted by different colours (a). Different mesh size in the junction zone (b).

67000 in the torso, 64000 in the junction zone, and 47000 in the arm). Moreover, the mesh size is 1 mm in the junction zone and 15 mm in the torso and arm, as shown in Fig. 6.3b.

6.4.3 3D non homogeneous realistic human model

Finally, we applied the new method also to a numerical dosimetry problem considering a realistic human body: the Japanese whole-body female human model Hanako, developed by the National Institute of Information and Communications Technology (NICT) [78]. The model is based on voxels with 2 mm spatial resolution, derived by the accumulated MRI images of adult Japanese volunteers of average build (height and weight).

A one-loop coil with a radius of 40 cm is located 60 cm from the torso and it is centered between the two shoulders, as shown in Fig. 6.4. The position of the coil ensures that the exposure is localized where the rotation of the arms takes place. The axis of the coil is the y-axis. The operating frequency is 50 Hz and the coil current is 100 A. Tissue conductivities are taken from the IT'IS Foundation database [14], however the value for skin conductivity is modified to 0.1 S/m according to [79].

The voxel-based mesh in the non-postured human model consists of about 6580000 nodes and 6315000 elements.

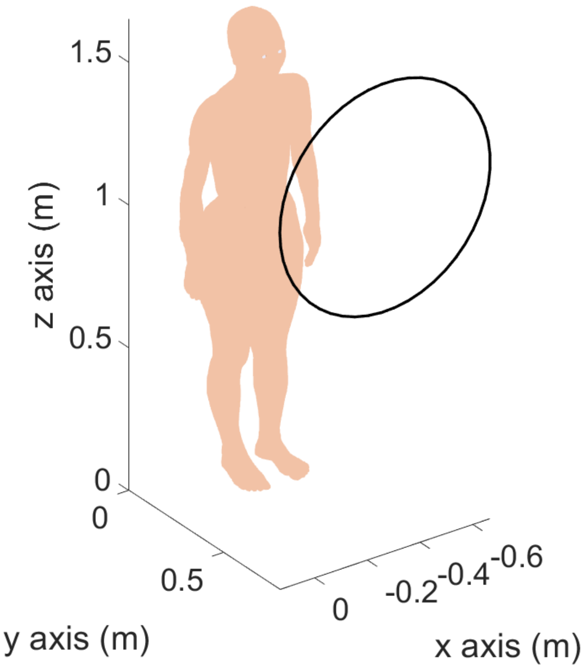

Figure 6.4: Exposure scenario of the female human model Hanako in the 3D domain.

6.5 Exposure scenarios in the 2D and 3D domain and the corresponding rotation matrices

The geometric transformation used in the test cases here analyzed is the rotation. More information about the structure and the properties of this transformation can be found in appendix A.

In the 2D domain, the ellipse is rotated clockwise by 90° by applying a rotation about the origin of the reference system in the center of the ellipse. According to formulas in appendix A, the rotation matrix of 90° amplitude is

$$\mathbf{R} = \begin{bmatrix} 0 & -1 \\ 1 & 0 \end{bmatrix}$$

In the 3D simplified phantom, the origin of the reference system is located between the torso and the junction, and it exactly coincides with the center of rotation. The geometric transformation used in this numerical simulation is determined by the rotation angle θ of the rotation matrix. Also in this case, the rotation is about the origin of the reference system and its matrix is given by

$$\mathbf{R}(\theta) = \begin{bmatrix} \cos\theta & -\sin\theta \\ \sin\theta & \cos\theta \end{bmatrix}.$$

The θ angle is: 1) equal to zero in the torso (no rotation); 2) equal to $\theta_{\max} = 120°$ in the arm; 3) linearly increasing in the junction zone, $\theta = \theta_{\max} \cdot (x/x_{\max})$ with $x_{\max} = 1$ cm. This linear variation approximates the real movement of the arm.

In the realistic human model, two different exposure scenarios are taken into account: 1) a rotation of 120° about the x-axis located in the center of the right shoulder; 2) two rotations of 90° about the x-axis, one located in the center of the right shoulder and the other located in the center of the left shoulder. In order to have reference solutions to which compare the numerical results obtained with the new approach, the respective postured human models with the rotated arms are created by using the software NICTPoseTool, which allows to posture Hanako by moving her joints.

Considering the non-postured phantom, it is worth noting that in these exposure scenarios the rotation center does not coincide with the origin of the reference system and, therefore, it is necessary to translate the rotation center before performing each rotation. For this reason, the transformation matrix has to be generalized in the following form

$$\mathbf{T} = \begin{bmatrix} \mathbf{R}(\theta) & \mathbf{t} \\ \mathbf{0} & \mathbf{1} \end{bmatrix}$$

where $\mathbf{R}(\theta)$ is the 3×3 rotation matrix of θ amplitude about the x-axis centered in the origin of the reference system, $\mathbf{t}$ is the 3×1 column vector referred to translation, $\mathbf{0}$ is the 1×3 zero matrix and $\mathbf{1}$ is the 1×1 identity matrix. More information can be found in the appendix A.

Since the Jacobian matrix $\mathbf{J}$ coincides with the rotation matrix, let us focus our attention on $\mathbf{R}(\theta)$. $\mathbf{R}(\theta)$ about x-axis in a 3D domain is defined as

$$\mathbf{R}(\theta) = \begin{bmatrix} 1 & 0 & 0 \\ 0 & \cos\theta & -\sin\theta \\ 0 & \sin\theta & \cos\theta \end{bmatrix}$$

It is worth noting that when θ is equal to zero, $\mathbf{R}(\theta)$ is the identity matrix.

In the exposure scenario in which both arms are rotated, even if the rotations occur in two different centers, they are independent to each other because they refer to two distinct objects (right arm and left arm). This means that rotating the right arm first and then the left one, or vice versa, is completely indifferent. Fig. 6.5 shows the order in which the two rotations were carried out in our numerical simulations: first the right arm was rotated of 90° about the x-axis while keeping all the other points fixed; subsequently the left arm was rotated of 90° about the x-axis by applying the rotation to the previously rotated points. Finally the two matrices have to be assembled together in order to obtain the final matrix.

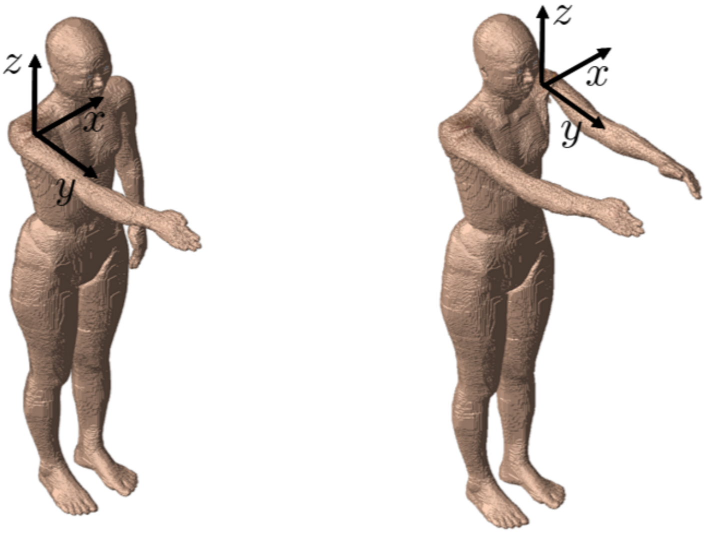

Figure 6.5: Two rotations of 90° about the x-axis applied to Hanako model, one located in the center of the right shoulder and the other located in the center of the left shoulder.

Let us see this from a mathematical point of view. Let $\mathbf{R}(\theta_r)$ be the rotation in the right arm and $\mathbf{R}(\theta_l)$ be the rotation in the left one. When $\mathbf{R}(\theta_r)$ is performed, only the right arm points rotate of γ_r angle, while the others remain unaffected by θ_r; vice versa, when $\mathbf{R}(\theta_l)$ is performed, only the left arm points rotate of γ_l angle. This means that: 1) the θ_r angle is equal to γ_r in the right arm, while is equal to zero in the other points; 2) the θ_l angle is equal to γ_l in the left arm, while is equal to zero in the other points.

In order to perform computations, the resulting rotation matrix must take into account what happens in each point during both rotations. A matrix multiplication is therefore necessary.

Let us, for example, analyze what happens in a point $P_1(x_1, y_1, z_1)$ located in the right arm during the transformations. As previously stated, the rotation matrices associated to this point are

$$\mathbf{R}_1(\theta_r) = \begin{bmatrix} 1 & 0 & 0 \\ 0 & \cos\theta_r & -\sin\theta_r \\ 0 & \sin\theta_r & \cos\theta_r \end{bmatrix}; \quad \mathbf{R}_1(\theta_l) = \begin{bmatrix} 1 & 0 & 0 \\ 0 & 1 & 0 \\ 0 & 0 & 1 \end{bmatrix}$$

The resulting matrix in P_1 can be obtained as follow

$$\mathbf{R}_1(\theta) = \mathbf{R}_1(\theta_r) \cdot \mathbf{R}_1(\theta_l) = \mathbf{R}_1(\theta_l) \cdot \mathbf{R}_1(\theta_r) = \mathbf{R}_1(\theta_r)$$

Therefore, by generalizing the concept to all the points of the domain, the rotation matrix used in this test case can be computed as

$$\mathbf{R}(\theta) = \mathbf{R}(\theta_r) \cdot \mathbf{R}(\theta_l) = \mathbf{R}(\theta_l) \cdot \mathbf{R}(\theta_r).$$

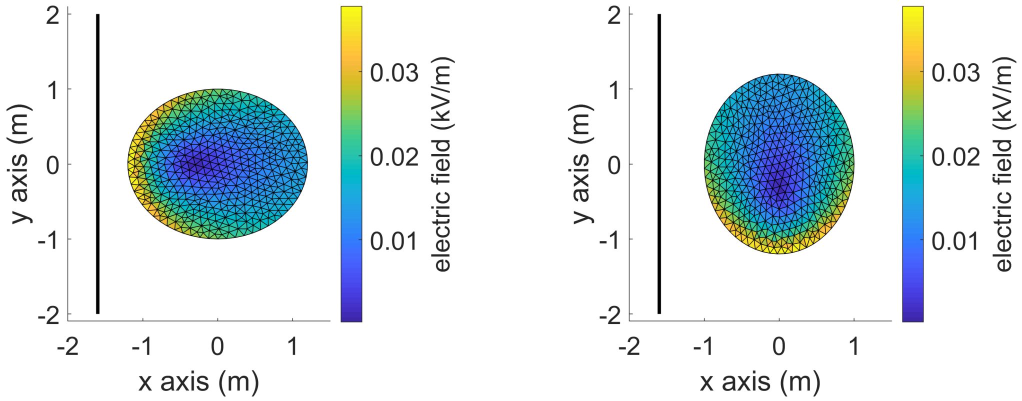

(a) electric field distribution on Ω_p

(b) electric field distribution on Ω

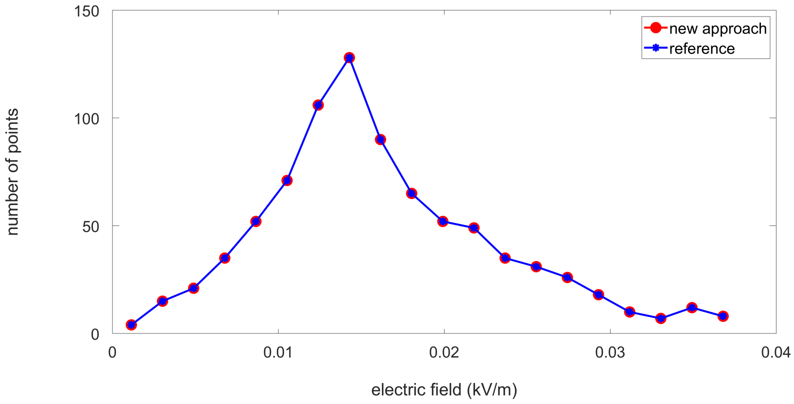

(c) Comparison of induced electric field between the reference case and the proposed method

Figure 6.6: Reference solution for the induced electric field (a). Solution obtained with the proposed method (b). Electric field frequency diagram for both solutions (c).

6.6 Numerical results

The numerical results obtained in the 2D and 3D domain described in paragraph 6.4 are here analyzed. In the next paragraphs the numerical results obtained with the postured models are taken as reference solutions to which compare the corresponding results obtained with the non-postured models in order to validate the new approach.

6.6.1 2D domain

In Fig. 6.6a (reference case), the ellipse is 90° rotated and it is evident that the maximum exposure is on the left side, the closest one to the source. In Fig. 6.6b, instead,

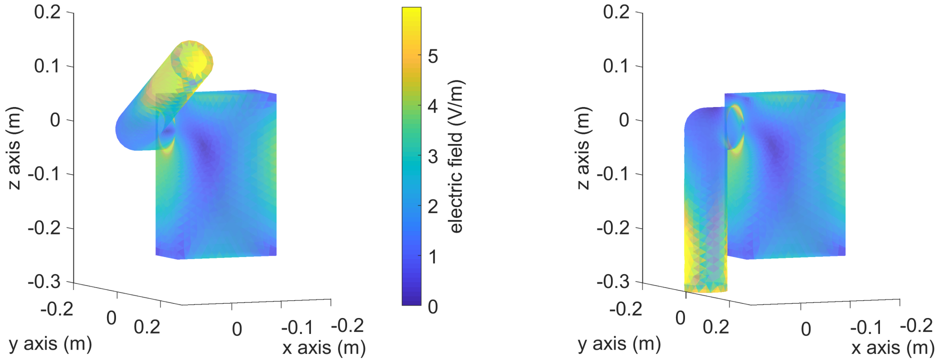

(a)

(b)

Figure 6.7: Induced electric field distribution evaluated with the classical approach on the postured phantom (a) and the proposed method on the non-postured phantom (b).

the induced electric field distribution obtained with the proposed method is shown. Since in the new approach the domain does not have to be transformed, the ellipse is not 90° rotated. Looking at Fig. 6.6b, we can see that, although the vertical wire is kept in the same position, the ellipse maximum exposure is on the lower side. This is possible thanks to the transformation of the source term (from $\mathbf{a}$ to $\mathbf{a}_\mathrm{p}$) provided in equation (6.2).

Fig. 6.6c shows the electric field frequency diagram for both methods. It underlines that the results obtained with the proposed method (red curve) are exactly the same as those obtained with the classical approach (blue curve).

6.6.2 3D homogeneous simplified phantom

In the simplified model, since the axis of the coil passes through the center of the shoulder, the phantom maximum exposure is at the end of the rotated arm, as the reference case (postured model) in Fig. 6.7a shows. Looking at Fig. 6.7b, we can say that the method works as expected: in fact, if the classic approach were used, the maximum exposure should be in the centre of the shoulder due to the alignment with the coil axis. However, Fig. 6.7b shows that the highest induced electric field concentration is in the arm extremity, exactly as in the reference case (Fig. 6.7a).

These results are also confirmed in Fig. 6.8, where a comparison of the values between the 90th and the 100th percentile (maximum exposure) values of the induced electric fields is done. Fig. 6.8 shows that the results are completely comparable in the torso and in the arm, and there is a little deviation in the junction. The reason is that a complete rotation occurs in the arm, whereas in the junction there is a piecewise rigid motion due to the linear variation of the Jacobian matrix angle. However, the largest deviation in the junction zone, evaluated as the ratio between the induced electric field value computed with the proposed method and the one computed with the classical approach, is ∼ 1.11. It means that there is an overestimation of 11%, more than acceptable in numerical

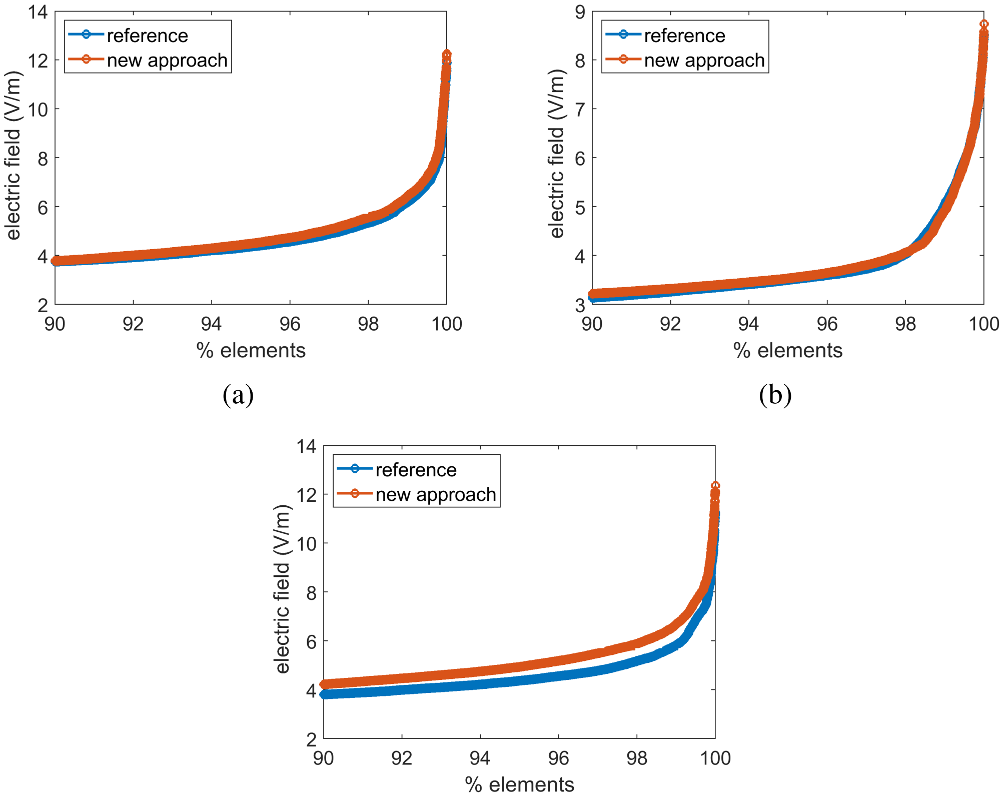

(a)

(b)

(c)

Figure 6.8: Comparison of the induced electric field values between the two different methods in each components: torso (a), arm (b), and junction (c). Focus between the 90th and the 100th percentile values of the induced electric field.

dosimetry.

6.6.3 3D non homogeneous realistic human model

After all, simulations by using the human model Hanako are performed.

Fig. 6.9 shows the induced electric field distribution evaluated with the classical and new approach in both the exposure scenarios. The maps of the electric field are in good agreement. The maximum exposure in both postured and non-postured models, in fact, is located in the torso and the hands due to the position of the coil. As we have explained in the previous paragraphs, we can say that the new method works as we expected because it gives the same results as the classical one.

In both scenarios the maximum exposure evaluated on the non-postured model with the new approach is in the skin, as Fig. 6.10 shows. Comparing this value with the one obtained on the postured model with the classical approach, the skin maximum value on the non-postured model is much higher than the one on the postured model. This is due to the effect of the rotation angle in the junction between the torso and the arms. In fact, in order to be able to completely compare the two different methods even in the junctions where the rotation occurs, it is fundamental knowing precisely the function used by the software (in this case NICTPoseTool) to posture the model. In this way, the new method would be able to modify the source term according to the function, making the two models comparable also in the junction. Unfortunately this information is not accessible by most of the posturing software. Hence the source term is not only approximated, but it is discontinuous at the junction where the rotation occurs.

However, Hanako is a human body discretized with voxels with 2 mm resolution. In chapter 5 we have widely analyzed the stair-casing approximation errors due to voxel-based meshes and the need of post-processing techniques to filter the numerical results. According to the literature, the use of the 99th and the 99.9th percentile values ensures to mitigate stair-casing approximation errors (and other source of numerical artifacts) and, for this reason, the comparison between the two methods is more interesting and reliable.

By observing Fig. 6.11 (case with the right arm rotated of 120° along x-axis) and Fig. 6.12 (case with both arms rotated of 90° along x-axis), it is possible to see that the 99th and the 99.9th percentile values evaluated with the two different approaches are completely comparable in all tissues. In particular, in Fig. 6.11 the 99.9th percentile is sufficient to mitigate the numerical artifacts previously described. In Fig. 6.12a, the only induced electric field value computed with the new method that differs from the one evaluated with the classic approach is still the skin value. Despite the observations previously made on the discontinuity present in the junctions where the rotation occurs, in general the skin is a tissue that must be treated with caution in numerical dosimetry because it can be the source of numerous numerical artifacts. Several studies have been conducted on this tissue. In [32], for example, it is pointed out that the $2 \times 2 \times 2$ mm^3 models does not correctly model the skin: the skin thickness, in fact, is much finer than the voxel resolution and this can cause numerical artifacts.

However, if the skin tissue that is the source of all the numerical artifacts previously described is excluded from our analysis, we can conclude that the new approach provides results more than acceptable and comparable with respect to the classical method.

6.7 Discussion

At the end of our analysis, we can conclude that the new approach to perform a dosimetry analysis without a postured body model returns reliable results, completely comparable with those obtained with the classical one. Unlike the classic approach in which all dosimetric computations are performed with a postured phantom, the new method is based on the evaluation of human exposure to electromagnetic fields by using a non-postured domain through a source term transformation.

This becomes very useful when workers exposure has to be evaluated in the workplace.

While in numerical dosimetry problems related to the public, the posture of the human body is in most cases fixed (e.g in MRI systems), in a workplace the worker is on the move and its posture changes many times. This means that, with the classical approach, it is necessary to posture the human model n times in order to have the exact posture to use in every simulations. Then, to solve a single exposure problem, n simulations are required, each for every different posture. This will become a very cumbersome task.

Using the new methodology, it is no longer necessary to use postured human phantoms to solve numerical dosimetry problems. Under certain realistic hypotheses, it is possible to prove that only the source term is affected by the posture, opening the possibility of using an approximate evaluation coming directly from measurements.

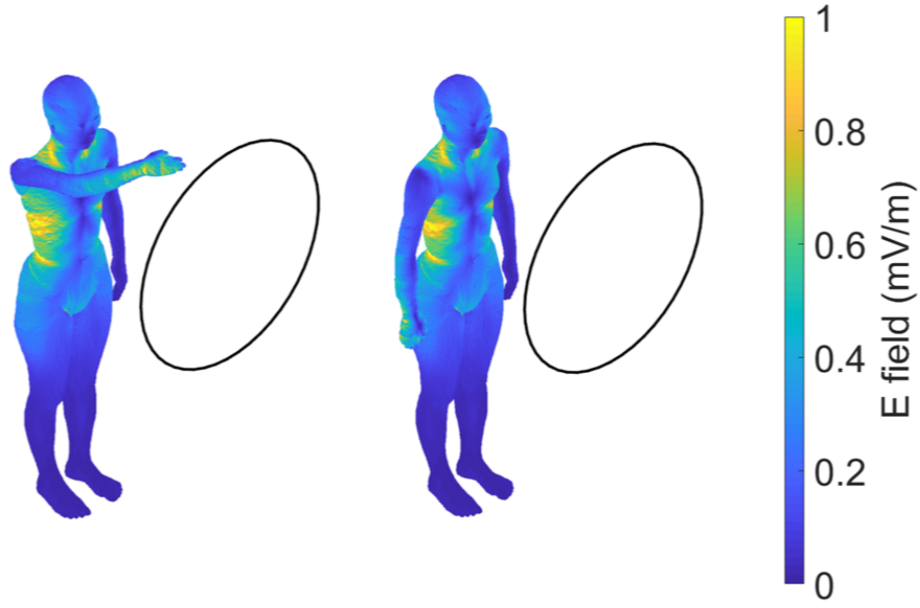

(a) Rotation of the right arm of 120° along x-axis.

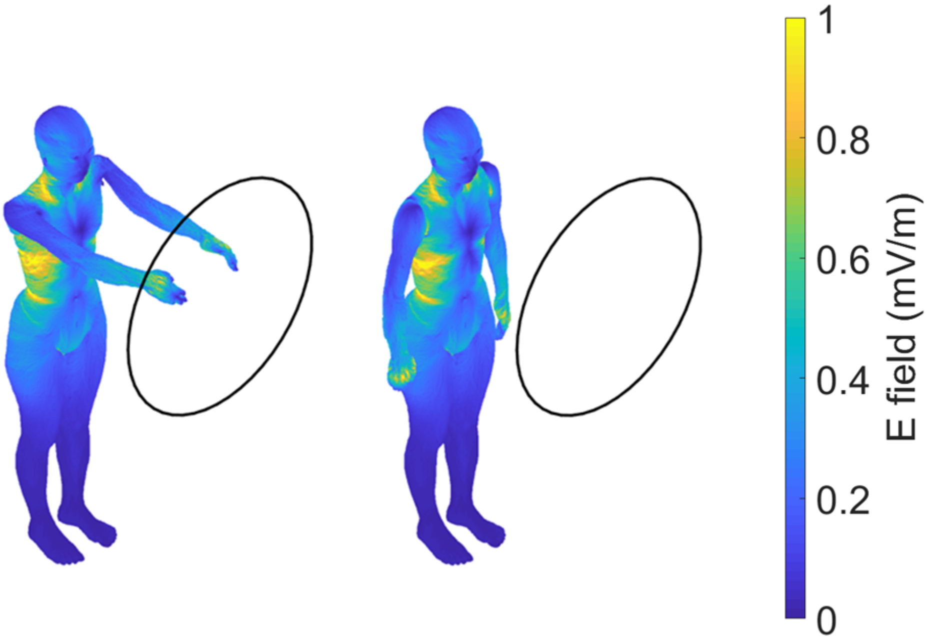

(b) Rotation of both arms of 90° along x-axis.

Figure 6.9: Induced electric field distribution evaluated with the classical approach on the postured model (on the left) and the proposed method on the non-postured model (on the right).

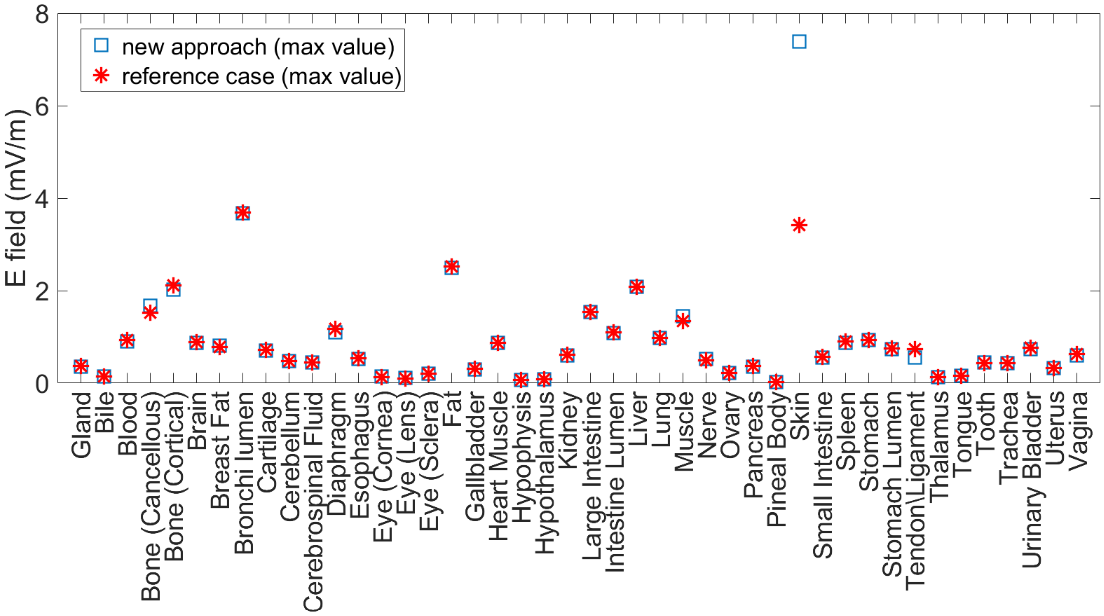

(a) Rotation of the right arm of 120° along *x*-axis.

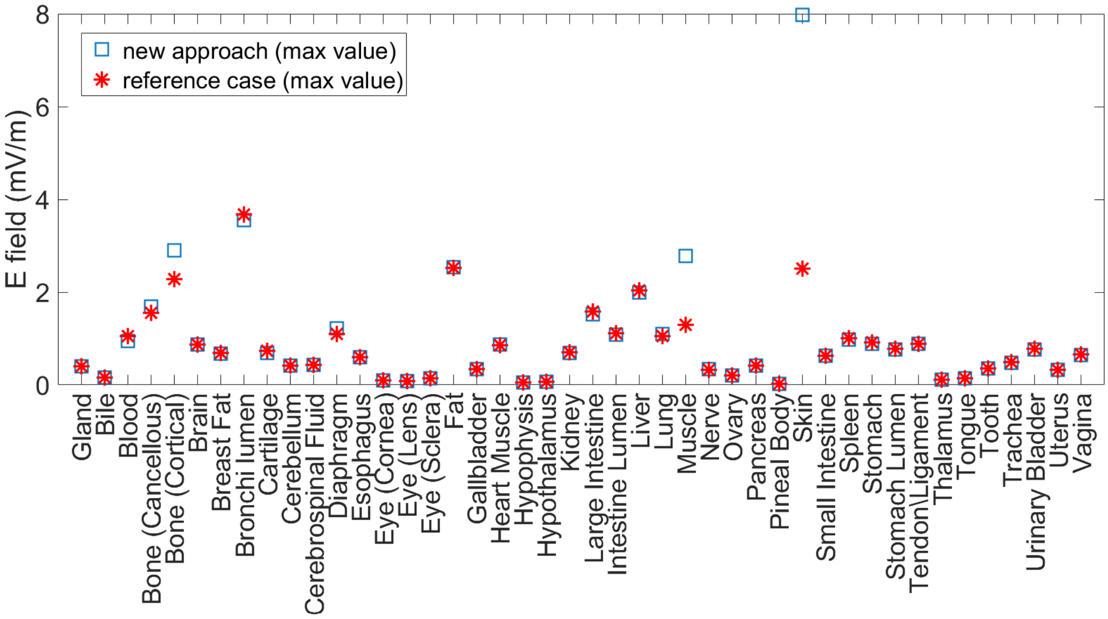

(b) Rotation of both arms of 90° along *x*-axis.

Figure 6.10: Comparison of the maximum induced electric field values in each tissue between the two different methods in both 3D realistic exposure scenarios.

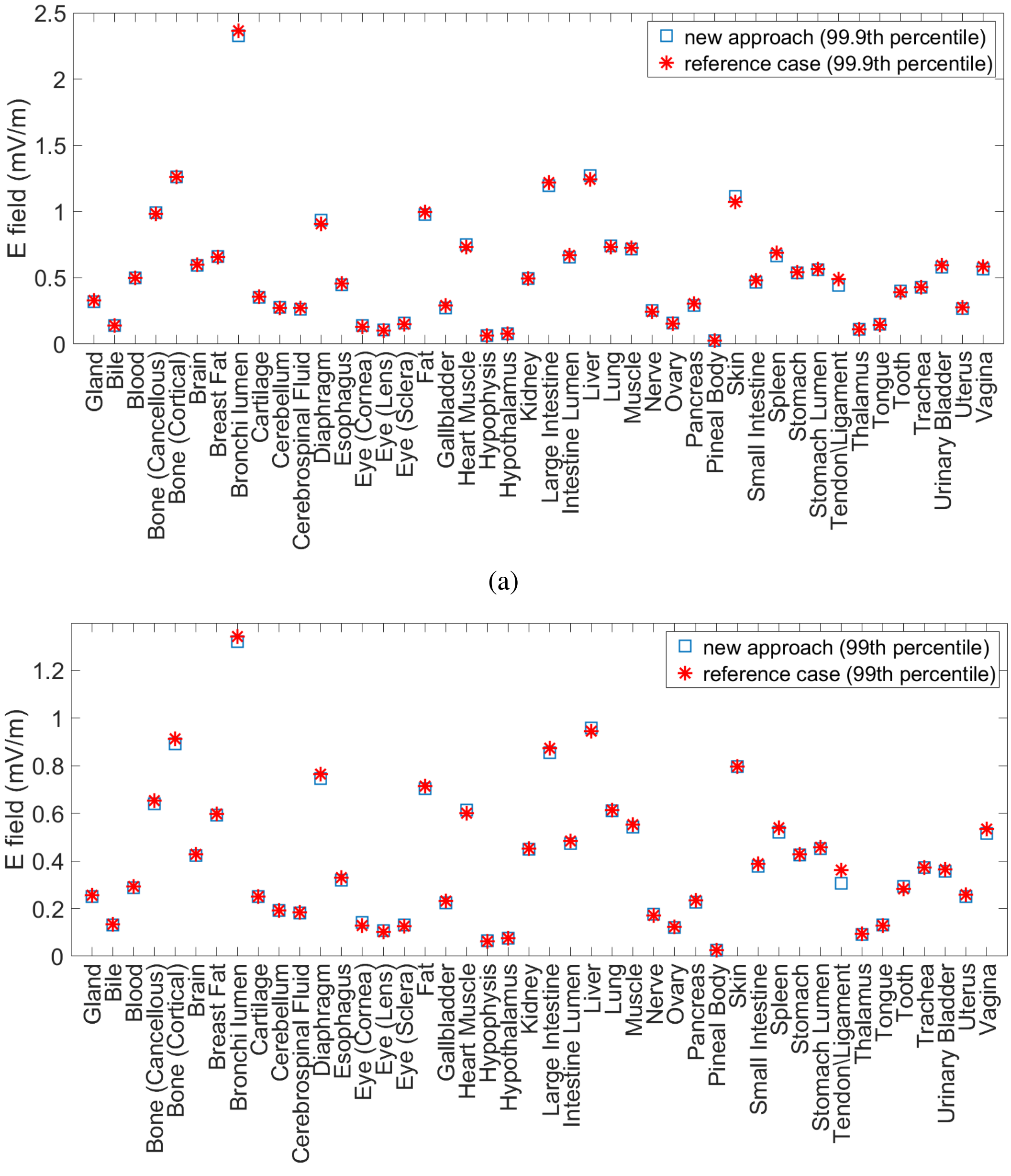

(a)

(b)

Figure 6.11: Comparison of the 99.9th percentile (a) and the 99th percentile values (b) of the induced electric field between the two different methods in each tissue (case: rotation of the right arm of 120° along x-axis).

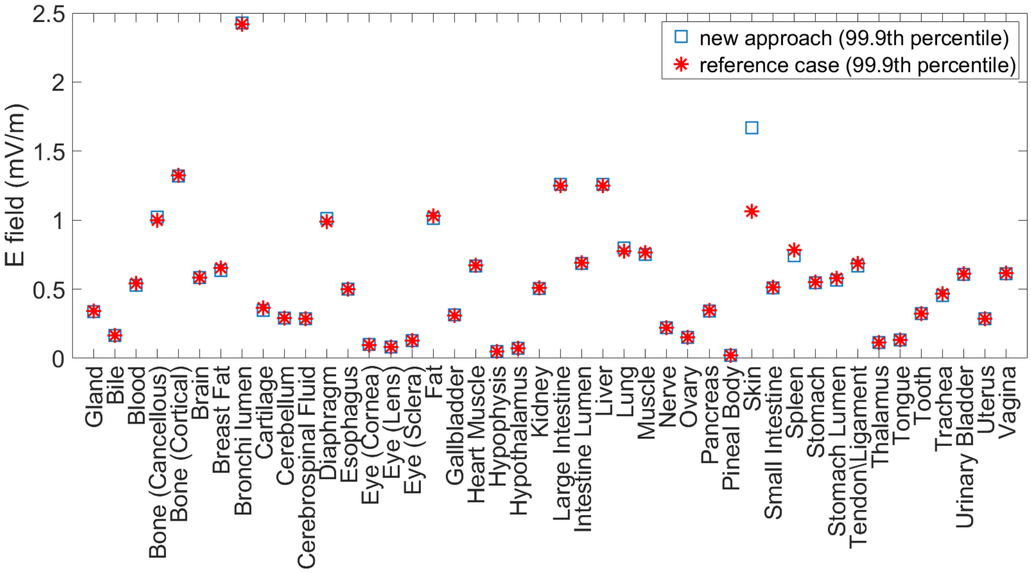

(a)

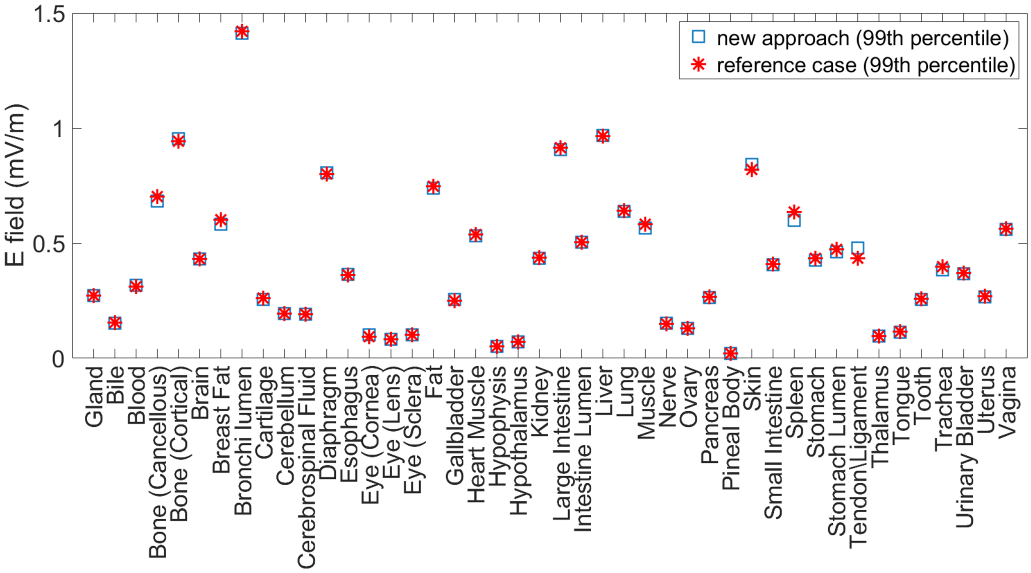

(b)

Figure 6.12: Comparison of the 99.9th percentile (a) and the 99th percentile values (b) of the induced electric field between the two different methods in each tissue (case: rotation of both arms of 90° along x-axis).

Chapter 7

Conclusions

The present work has addressed some problems related to low-frequency numerical dosimetry and new solutions have been provided through the use of different approaches.

Low-frequency numerical dosimetry plays a fundamental role to evaluate the influence of electromagnetic fields on the human body. A correct exposure assessment is essential to evaluate the actual risks deriving from the interaction of the electromagnetic fields with the tissues of the human body. During these years, in fact, guidelines and standards ([6], [5], [16]) that establish the limits to be respected to ensure a safe human exposure have been defined by international organizations.

Performing numerical simulations which gives reliable results is extremely important. In order to do that it is required an accurate modelling of the electromagnetic field source and the exact posture of the human body. As we have seen in the previous chapters, these two requirements are not always available, mostly in many realistic exposure scenarios. In this thesis alternative methods to be able to perform numerical dosimetry simulations without these two information have been proposed.

The first problem faced regards the increasingly widespread interest in performing numerical dosimetry starting from data coming from general purpose software or measurements. In this case the accurate modelling of the electromagnetic field source is impossible. Two available methods [54], [49] that make dosimetry starting from the knowledge of the magnetic flux density are compared by using real and virtual measurements, and the results are analyzed in order to highlight when one method should be preferred over the other. It is found that when the magnetic flux density comes from a simulation tool, method described in [49] coupled with the divergence free interpolator provides the most accurate results. Otherwise, when the magnetic flux density is obtained through real measurements, the use of this method requires more attention because a large number of measurements points could lead to higher errors. For this reason, in this case, method described in [54] is the preferred solution because it provides very stable results in any test condition. Furthermore, as described in [56] where these studies are published, it is also pointed out that a huge number of measurement points is not necessary to obtain acceptable results.

The second topic studied in the present work regards the importance to exactly know the posture of the human body while a numerical dosimetry simulation is performed. Two types of problems can arise: 1) the exact posture of the human body is known, but human models in the required posture are not available or the software used to posture the human phantom introduces numerical artifacts; 2) the exposure scenario allows to know the posture of the human body only approximately. In this thesis a new approach to assess human exposure to electromagnetic fields without the need of exactly knowing the human body posture is presented and analyzed. It is base on performing numerical simulations by using a non-postured human model and to modify the source term through suitable geometric transformations. The test cases studied showed that the new approach provides results comparable to the ones obtained with the classical method, paving the way for possible future applications. The fact of using non-postured models is a strength of the new method because it guarantees that the phantom is anatomically correct.

Further investigation about this topic are expected in the next months. The accuracy of the new method has to be tested on more complex sources and posture (e.g. two rotations in the same arm). The main problem consists in discovering the exact map used by the posturing software to model the postured human models, in order to be able to reproduce it on the source term. In this way the new and classic approach would be completely comparable. To overcome this problem, we are thinking of using the methods which allow to estimate the source term directly from the measurements, by assuming only a partial knowledge of the real posture of the phantom (or no knowledge at all).

The last important topic studied in this thesis concerns the discretization of anatomical realistic human models with tetrahedral mesh. As we have seen, human models used in numerical dosimetry are discretized with voxel-based meshes because they are built starting from DICOM (Digital Imaging and Communications in Medicine) imagines. Low-frequency numerical dosimetry simulations performed by using voxelized human models are subject to stair-casing approximation errors when curved boundaries are approximate with voxels and the use of filtering techniques is necessary to eliminate these numerical artifacts. Recently, to better reproduce the curved boundaries of organs and tissues, tetrahedral meshes started to be used. In this thesis the possibility that the use of tetrahedral meshes to discretize human models could eliminate stair-casing approximation errors in numerical dosimetry simulations has been studied. It is found out that tetrahedral meshes make it possible, but in real exposure scenarios other sources of numerical artifacts are still present and must be filtered out with suitable techniques. These numerical artifacts are related to two fundamental factors: the tetrahedral mesh quality and the tissue contrast effect.

Appendix A

The Jacobian matrix and rotation matrix

In this appendix, the Jacobian matrix and the rotation matrix are described and the relations between them are analyzed [80]. Afterwards, a further study on the Jacobian matrix used in chapter 6 in the study of the whole realistic human body is carried out.

A.1 The Jacobian matrix

Definition Let $\mathbf{f} : \mathbb{R}^n \rightarrow \mathbb{R}^m$ be a vector-valued function that associates to $\mathbf{x} = (x_1, x_2, ..., x_n) \in \mathbb{R}^n$ the value $\mathbf{f}(\mathbf{x}) = (f_1(\mathbf{x}), f_2(\mathbf{x}), ..., f_m(\mathbf{x})) \in \mathbb{R}^m$. The *Jacobian matrix* $\mathbf{J}$ of $\mathbf{f}$ is the $m \times n$ matrix whose elements are its first-order partial derivatives. It is defined as

$$\mathbf{J}(\mathbf{x}) = \begin{bmatrix} \frac{\partial f_1(\mathbf{x})}{\partial x_1} & \frac{\partial f_1(\mathbf{x})}{\partial x_2} & \cdots & \frac{\partial f_1(\mathbf{x})}{\partial x_n} \\ \frac{\partial f_2(\mathbf{x})}{\partial x_1} & \frac{\partial f_2(\mathbf{x})}{\partial x_2} & \cdots & \frac{\partial f_2(\mathbf{x})}{\partial x_n} \\ \vdots & \vdots & \ddots & \vdots \\ \frac{\partial f_m(\mathbf{x})}{\partial x_1} & \frac{\partial f_m(\mathbf{x})}{\partial x_2} & \cdots & \frac{\partial f_m(\mathbf{x})}{\partial x_n} \end{bmatrix}$$

where the ith row corresponds to the gradient of the ith component f_i of function $\mathbf{f}$, with $i = 1, ..., m$.

In general, the Jacobian matrix can be written as

$$\mathbf{J}(\mathbf{x}) = \frac{\mathrm{d}\mathbf{f}(\mathbf{x})}{\mathrm{d}\mathbf{x}} = \begin{bmatrix} \frac{\partial \mathbf{f}(\mathbf{x})}{\partial x_1} & \cdots & \frac{\partial \mathbf{f}(\mathbf{x})}{\partial x_n} \end{bmatrix} = \begin{bmatrix} \nabla f_1(\mathbf{x}) \\ \nabla f_2(\mathbf{x}) \\ \vdots \\ \nabla f_m(\mathbf{x}) \end{bmatrix}. \tag{A.1}$$

When $m = n$, $\mathbf{f} : \mathbb{R}^n \rightarrow \mathbb{R}^n$ is a vector-valued function from $\mathbb{R}^n$ to itself. According to (A.1), the Jacobian matrix becomes a square matrix and its determinant, known as *the Jacobian determinant* which is indicated throughout the manuscript as $|\mathbf{J}|$ (or simply *the Jacobian*), can be computed.

A.1.1 The Jacobian matrix of a linear transformations

Definition A *linear transformation* (or *linear map*) is a function $\mathbf{t} : \mathbb{R}^n \rightarrow \mathbb{R}^m$ that satisfies the following properties:

1. $\mathbf{t}(\mathbf{x} + \mathbf{y}) = \mathbf{t}(\mathbf{x}) + \mathbf{t}(\mathbf{y})$
2. $\mathbf{t}(a\mathbf{x}) = a\mathbf{t}(\mathbf{x})$

for any vectors $\mathbf{x}, \mathbf{y} \in \mathbb{R}^n$ and any scalar $a \in \mathbb{R}$.

A matrix $\mathbf{T}$, called *transformation matrix*, is associated with every linear transformation, and viceversa; there exists, in fact, a one-to-one correspondence between matrices and linear transformations, based on matrix vector multiplication.

Let $\mathbf{x} = (x_1, x_2, ..., x_n) \in \mathbb{R}^{n\times 1}$ and $\mathbf{y} = (y_1, y_2, ..., y_n) \in \mathbb{R}^{n\times 1}$ vectors of real scalar variables, functionally independent, i.e no element in $\mathbf{x}$ is a function of the other elements in $\mathbf{x}$ and similarly no element in $\mathbf{y}$ is a function of the other elements in $\mathbf{y}$. Let $\mathbf{T} = (t_{ij}) \in \mathbb{R}^{n\times n}$, with $i = 1, ..., n$ and $j = 1, ..., n$, be a linear transformation matrix with $|\mathbf{T}| \neq 0$ such as

$$\mathbf{y} = \mathbf{T}\mathbf{x}. \tag{A.2}$$

(A.2) can be written as

$$\begin{bmatrix} y_1 \\ y_2 \\ \vdots \\ y_n \end{bmatrix} = \begin{bmatrix} t_{11} & t_{12} & \cdots & t_{1n} \\ t_{21} & t_{22} & \cdots & t_{2n} \\ \vdots & \vdots & \ddots & \vdots \\ t_{n1} & t_{n2} & \cdots & t_{nn} \end{bmatrix} \begin{bmatrix} x_1 \\ x_2 \\ \vdots \\ x_n \end{bmatrix} \Longrightarrow \begin{cases} y_1 = t_{11}x_1 + t_{12}x_2 + \ldots + t_{1n}x_n \\ y_2 = t_{21}x_1 + t_{22}x_2 + \ldots + t_{2n}x_n \\ \vdots \\ y_n = t_{n1}x_1 + t_{n2}x_2 + \ldots + t_{nn}x_n \end{cases}$$

According to (A.1), the Jacobian matrix associated with (A.2) is

$$\mathbf{J}(\mathbf{x}) = \begin{bmatrix} \frac{\partial y_1(\mathbf{x})}{\partial x_1} & \frac{\partial y_1(\mathbf{x})}{\partial x_2} & \cdots & \frac{\partial y_1(\mathbf{x})}{\partial x_n} \\ \frac{\partial y_2(\mathbf{x})}{\partial x_1} & \frac{\partial y_2(\mathbf{x})}{\partial x_2} & \cdots & \frac{\partial y_2(\mathbf{x})}{\partial x_n} \\ \vdots & \vdots & \ddots & \vdots \\ \frac{\partial y_n(\mathbf{x})}{\partial x_1} & \frac{\partial y_n(\mathbf{x})}{\partial x_2} & \cdots & \frac{\partial y_n(\mathbf{x})}{\partial x_n} \end{bmatrix} = \begin{bmatrix} t_{11} & t_{12} & \cdots & t_{1n} \\ t_{21} & t_{22} & \cdots & t_{2n} \\ \vdots & \vdots & \ddots & \vdots \\ t_{n1} & t_{n2} & \cdots & t_{nn} \end{bmatrix} = \mathbf{T}. \tag{A.3}$$

Therefore, the transformation matrix $\mathbf{T}$ of a linear transformation coincides with the Jacobian matrix $\mathbf{J}(\mathbf{x})$ associated with that transformation.

A.1.2 Rotation matrix

Definition A *rotation* is an isometric transformation of the Euclidean plane and space which moves objects in a rigid motion, preserving their distances, and which leaves at least a fixed point, in the case of the 2D domain, or a fixed straight line, in the case of 3D domain. Fixed a rotation center or a rotation axis, the rotation is counterclockwise if the rotation angle is positive and clockwise if it is negative.

Since rotation is a linear transformation, it can be associated with a transformation matrix, called *rotation matrix*.

Definition In linear algebra, a *rotation matrix* **R** is a matrix that is used to perform a rotation in Euclidean place and space.

Rotation matrices are always square, with real entries. Algebraically, a rotation matrix is an orthogonal matrix whose determinant is 1:

$$\mathbf{R}^{\mathrm{T}} = \mathbf{R}^{-1}, |\mathbf{R}| = 1$$

A.1.3 Rotation matrix in two dimensions

Let xOy be the Cartesian plane and let $P(x, y)$ and $P'(x', y')$ be two points of xOy. Let us suppose to move the point P to the point P' through a counterclockwise rotation with angle α about the origin O. The new coordinates (x', y') can be computed as following

$$\begin{cases} x' = x\cos\alpha - y\sin\alpha \\ y' = x\sin\alpha + y\cos\alpha \end{cases} \tag{A.4}$$

which, written in matrix terms, becomes

$$\begin{bmatrix} x' \\ y' \end{bmatrix} = \begin{bmatrix} \cos\alpha & -\sin\alpha \\ \sin\alpha & \cos\alpha \end{bmatrix} \begin{bmatrix} x \\ y \end{bmatrix} \Longrightarrow \mathbf{P}' = \mathbf{R}(\alpha)\mathbf{P}$$

where $\mathbf{R}(\alpha)$ is the 2×2 rotation matrix associated with the rotation about the origin O. According to (A.3), $\mathbf{R}(\alpha)$ coincides with the Jacobian matrix of the transformation.

Let now $P(x, y)$, $P'(x', y')$ and $C(x_C, y_C)$ be three points of xOy. Let us suppose to move the point P to the point P' through a counterclockwise rotation of α amplitude about the point $C(x_C, y_C)$, other than the origin of the reference system. Looking at Fig. A.1 and keeping in mind that in any transformation the apex refers to the transformed point, to rotate about any point we need to:

1. translate the origin of the reference system in C through a vector $\mathbf{v} = (x_C, y_C)$ by using the translation transformation, and evaluate P coordinates in the new reference system

$$\begin{cases} x' = x + x_C \\ y' = y + y_C \end{cases} \longrightarrow \begin{cases} x = x' - x_C \\ y = y' - y_C \end{cases}$$

2. apply the rotation of α amplitude about the point C (origin of the reference system $x'Cy'$). The rotation transformation is

$$\begin{cases} x' = (x - x_C)\cos\alpha - (y - y_C)\sin\alpha \\ y' = (x - x_C)\sin\alpha + (y - y_C)\cos\alpha \end{cases}$$

3. undo the translation by translating the origin back to O through

$$\begin{cases} x' = (x - x_C)\cos\alpha - (y - y_C)\sin\alpha + x_C \\ y' = (x - x_C)\sin\alpha + (y - y_C)\cos\alpha + y_C \end{cases}$$

   and, by solving the computations, it becomes

$$\begin{cases} x' = x\cos\alpha - y\sin\alpha + x_C - x_C\cos\alpha + y_C\sin\alpha \\ y' = x\sin\alpha + y\cos\alpha + y_C - x_C\sin\alpha - y_C\cos\alpha \end{cases} \tag{A.5}$$

which are the equations of the rotation of α amplitude about any point $C(x_C, y_C)$ other than the origin of xOy.

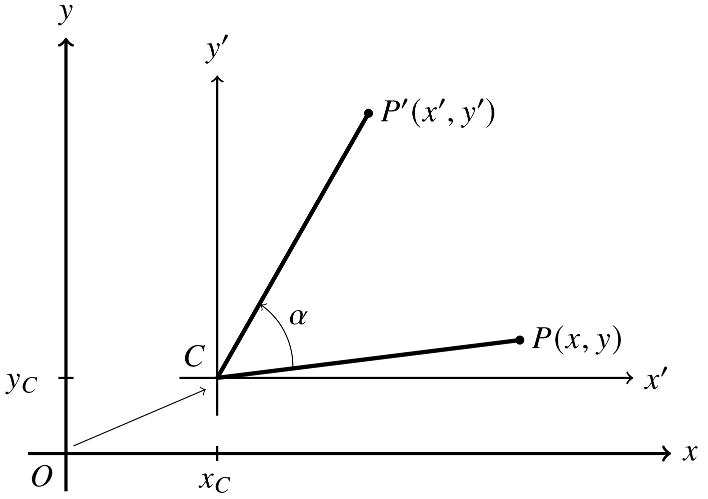

Figure A.1: Counterclockwise rotation of α amplitude about the point $C(x_C, y_C)$, other than the origin of the reference system.

In matrix terms, (A.5) becomes

$$\begin{bmatrix} x' \\ y' \end{bmatrix} = \begin{bmatrix} \cos\alpha & -\sin\alpha \\ \sin\alpha & \cos\alpha \end{bmatrix} \begin{bmatrix} x \\ y \end{bmatrix} + \begin{bmatrix} x_C - x_C\cos\alpha + y_C\sin\alpha \\ y_C - x_C\sin\alpha - y_C\cos\alpha \end{bmatrix} \Longrightarrow \mathbf{P}' = \mathbf{R}(\alpha)\mathbf{P} + \mathbf{t} \tag{A.6}$$

where $\mathbf{t}$ is the 2×1 column vector referred to translation. According to (A.3) and considering (A.5), $\mathbf{R}(\alpha)$ coincides with the Jacobian matrix of the transformation.

In general, the matrix transformation **T** associated with a rotation of α amplitude about a point $C(x_C, y_C)$ other than the origin of the reference system is a 3×3 matrix and it can be written as

$$\mathbf{T} = \begin{bmatrix} \cos\alpha & -\sin\alpha & x_C - x_C\cos\alpha + y_C\sin\alpha \\ \sin\alpha & \cos\alpha & y_C - x_C\sin\alpha - y_C\cos\alpha \\ 0 & 0 & 1 \end{bmatrix} = \begin{bmatrix} \mathbf{R}(\alpha) & \mathbf{t} \\ \mathbf{0} & \mathbf{1} \end{bmatrix}$$

where $\mathbf{R}(\alpha)$ is the 2×2 rotation matrix associated with the rotation about the origin O, $\mathbf{t}$ is the 2×1 column vector referred to translation, $\mathbf{0}$ is the 1×2 zero matrix and $\mathbf{1}$ is the 1×1 identity matrix. By performing computations with **T**, (A.6) becomes

$$\begin{bmatrix} x' \\ y' \\ 1 \end{bmatrix} = \begin{bmatrix} \cos\alpha & -\sin\alpha & x_C - x_C\cos\alpha + y_C\sin\alpha \\ \sin\alpha & \cos\alpha & y_C - x_C\sin\alpha - y_C\cos\alpha \\ 0 & 0 & 1 \end{bmatrix} \begin{bmatrix} x \\ y \\ 1 \end{bmatrix}$$

A.1.4 Rotation matrix in three dimensions

The following three 3×3 rotation matrices of α amplitude rotate vectors about the x-, y- or z-axis in the three dimensional space by centering the rotation in the origin of the reference system:

$$\mathbf{R}_x(\alpha) = \begin{bmatrix} 1 & 0 & 0 \\ 0 & \cos\alpha & -\sin\alpha \\ 0 & \sin\alpha & \cos\alpha \end{bmatrix}$$

$$\mathbf{R}_y(\alpha) = \begin{bmatrix} \cos\alpha & 0 & \sin\alpha \\ 0 & 1 & 0 \\ -\sin\alpha & 0 & \cos\alpha \end{bmatrix}$$

$$\mathbf{R}_z(\alpha) = \begin{bmatrix} \cos\alpha & -\sin\alpha & 0 \\ \sin\alpha & \cos\alpha & 0 \\ 0 & 0 & 1 \end{bmatrix}$$

It is worth noting that when, for example, a vector is rotated about the x-axis, its x coordinates remain fixed, while the others change. Similarly, this happens for the rotations about the y- and z-axis. According to (A.3), the rotation matrices coincide with the Jacobian matrix of the transformation.

As previously done in the two-dimensional case, they can be generalized using the transformation matrix **T** associated with any rotation of α amplitude about the x-, y- or z-axis by centering the rotation in any point $C(x_C, y_C)$ other than the origin of the reference system. We obtain

$$\mathbf{T}_x = \begin{bmatrix} 1 & 0 & 0 & 0 \\ 0 & \cos\alpha & -\sin\alpha & y_C - y_C\cos\alpha + z_C\sin\alpha \\ 0 & \sin\alpha & \cos\alpha & z_C - y_C\sin\alpha - z_C\cos\alpha \\ 0 & 0 & 0 & 1 \end{bmatrix} = \begin{bmatrix} \mathbf{R}_x(\alpha) & \mathbf{t}_x \\ \mathbf{0} & \mathbf{1} \end{bmatrix}$$

$$\mathbf{T}_y = \begin{bmatrix} \cos\alpha & 0 & \sin\alpha & x_C - x_C\cos\alpha - z_C\sin\alpha \\ 0 & 1 & 0 & 0 \\ -\sin\alpha & 0 & \cos\alpha & z_C + x_C\sin\alpha - z_C\cos\alpha \\ 0 & 0 & 0 & 1 \end{bmatrix} = \begin{bmatrix} \mathbf{R}_y(\alpha) & \mathbf{t}_y \\ \mathbf{0} & \mathbf{1} \end{bmatrix}$$

$$\mathbf{T}_z = \begin{bmatrix} \cos\alpha & -\sin\alpha & 0 & x_C - x_C\cos\alpha + y_C\sin\alpha \\ \sin\alpha & \cos\alpha & 0 & y_C - x_C\sin\alpha - y_C\cos\alpha \\ 0 & 0 & 1 & 0 \\ 0 & 0 & 0 & 1 \end{bmatrix} = \begin{bmatrix} \mathbf{R}_z(\alpha) & \mathbf{t}_z \\ \mathbf{0} & \mathbf{1} \end{bmatrix}$$

By generalizing, the transformation matrix can be written as follow

$$\mathbf{T} = \begin{bmatrix} \mathbf{R}(\alpha) & \mathbf{t} \\ \mathbf{0} & \mathbf{1} \end{bmatrix}$$

where $\mathbf{R}(\alpha)$ is the 3×3 rotation matrix of α amplitude about the x-, y- or z-axis centered in the origin of the reference system, $\mathbf{t}$ is the 3×1 column vector referred to translation, $\mathbf{0}$ is the 1×3 zero matrix and $\mathbf{1}$ is the 1×1 identity matrix.

Also in this case, according to (A.3), the rotation matrices $\mathbf{R}(\alpha)$ coincide with the Jacobian matrix of the transformation $\mathbf{T}$.

Appendix B

Coordinate transformation

Transformation methods are a very powerful tool in electromagnetism since an adequate mapping is able to transform the problem into an easier one [76].

In chapter 6 the concept of coordinate transformation has been introduced to describe a new approach which allows to make numerical dosimetry directly on a non-postured human model by eliminating the posturing step. Starting from the algebraic formulation of the SPFD method described in chapter 3, in which the human body has to be postured in the exact position in order to obtain realistic results, a new formulation is found out by applying appropriate changes of coordinates to the tissue conductivity matrix $\mathbf{M}_\sigma$ and the source term $\mathbf{a}_\mathrm{s}$. In this new formulation the scalar electric potential φ is evaluated by using the non-postured human body.

In this appendix the idea that has lead to obtain the new quantities $\mathbf{M}_{\sigma_\mathrm{p}}$ and $\mathbf{a}_p$ is summarized.

B.1 General idea

Let some coordinate transformation $\mathbf{x} \mapsto \mathbf{x}'$, which lead quantities defined on the domain Ω to equivalent quantities defined on the domain Ω', be considered. Hereafter, the superscript $'$ indicates quantities obtained through the applied transformation. Let $\mathbf{J}$ be the Jacobian matrix associated to the transformation and let J_{ij} be the element of the Jacobian matrix defined as

$$J_{ij} = \frac{\partial x'_i}{\partial x_j}. \tag{B.1}$$

According to equations analyzed in chapter 3, it is possible to show that $\nabla \cdot (\sigma \mathbf{E}) = 0$ can be transformed into the equivalent form $\nabla' \cdot (\sigma' \mathbf{E}') = 0$ by replacing ∇ with ∇', if the following transformations are made [77]

$$\mathbf{E}' = \mathbf{J}^{-T}\mathbf{E}, \tag{B.2}$$

$$\sigma' = \frac{\mathbf{J}\sigma\mathbf{J}^T}{|\mathbf{J}|}. \tag{B.3}$$

From (B.2) and (B.3), the quantities $\mathbf{E}$ and σ can be derived

$$\mathbf{E} = \mathbf{J}^T\mathbf{E}', \tag{B.4}$$

$$\sigma = \mathbf{J}^{-1}\sigma'\mathbf{J}^{-T} \cdot |\mathbf{J}|\,. \tag{B.5}$$

Let's now define $\partial_a = \partial/\partial x_a$. Under the coordinate change $\mathbf{x} \mapsto \mathbf{x}'$, according to (B.1), we have $\partial_a = J_{ba}\partial'_b$. Finally let $E_a = J_{ba}E'_b$ thanks to (B.4) . Keeping all of this in mind, $\nabla \cdot (\sigma\mathbf{E}) = 0$ becomes

$$\begin{aligned}
0 &= \partial_a\sigma_{ab}E_b = J_{ia}\partial'_i\sigma_{ab}J_{jb}E'_j \\
&= J_{ia}\partial'_i \cdot |\mathbf{J}| \cdot J^{-1}_{ak}\sigma'_{kj}J^{-1}_{jb}J_{jb}E'_j \\
&= J_{ia}\partial'_i \cdot |\mathbf{J}| \cdot J^{-1}_{ak}\sigma'_{kj}E'_j \\
&= |\mathbf{J}| \cdot \partial'_i\sigma'_{ij}E'_j + (\partial_a J^{-1}_{ak} \cdot |\mathbf{J}|)\sigma'_{kj}E'_j \\
&= \partial'_i\sigma'_{ij}E'_j,
\end{aligned}$$

which gives $\nabla' \cdot (\sigma'\mathbf{E}') = 0$. The quantity $\partial_a J^{-1}_{ak} \cdot |\mathbf{J}| = 0$ according to [77].

B.2 Coordinate transformation applied to the algebraic formulation of SPFD method

Considering the coordinate transformation $\mathbf{x} \mapsto \mathbf{x}'$ above described, in the case of a low-frequency numerical dosimetry problem the domain Ω represents the non-postured human body, while the domain Ω' represents the postured human body.

Since the new formulation is defined by using a non-postured human body, from (B.5) it is easy to derive the quantity

$$\mathbf{M}^{\mathrm{loc}}_{\sigma_\mathrm{p}} = \mathbf{J}_p^{-1}\mathbf{M}^{\mathrm{loc}}_{\sigma}\mathbf{J}_p^{-\mathrm{T}} \cdot \left|\mathbf{J}_p\right|$$

analyzed in chapter 6.

Having shown that $\nabla \cdot (\sigma\mathbf{E}) = 0$ can be transformed into the equivalent form $\nabla' \cdot (\sigma'\mathbf{E}') = 0$ by applying (B.4) and (B.5) and remembering that $\mathbf{E}$ and $\mathbf{A}$ are related to each other by (3.7), shown below

$$\mathbf{E} = -\nabla\varphi - \frac{\partial\mathbf{A}}{\partial t},$$

it is straightforward to deduce that if $\mathbf{E} = \mathbf{J}^T\mathbf{E}'$, then $\mathbf{A} = \mathbf{J}^T\mathbf{A}'$, which coincides with the transformation used in chapter 6 to find the new quantities $\mathbf{a}_p$ in the algebraic form.

Bibliography

[1] *Electromagnetic fields [0 hz - 300 ghz] : Risk description*, `https://www.portaleagentifisici.it/fo_campi_elettromagnetici_index.php?lg=EN` (accessed May 8, 2022).

[2] J. Pandya, *The weaponization of the electromagnetic spectrum*, `https://www.forbes.com/sites/cognitiveworld/2019/04/12/the-weaponization-of-the-electromagnetic-spectrum/?sh=6359c2a0699e` (accessed May 8, 2022).

[3] M. Massaro, *Thesis for the Degree of Licentiate of Philosophy. Radio Spectrum Regulation in the European Union: A three-level context*. Feb. 2017.

[4] M. E. Van Valkenburg, *Reference Data for Engineers*. 2001.

[5] ICNIRP2010, "Guidelines for limiting exposure to time-varying electric and magnetic fields (1 Hz to 100 kHz)", *Health Phys.*, vol. 99, no. 6, pp. 818–836, 2010.

[6] ICNIRP1998, "Guidelines for limiting exposure to time-varying electric, magnetic, and electromagnetic fields (up to 300 GHz)", *Health Phys.*, vol. 74, no. 4, pp. 494–521, 1998.

[7] *Low frequency electromagnetic fields*, `https://www.icnirp.org/en/frequencies/low-frequency/index.html` (accessed May 8, 2022).

[8] *È vero che i campi elettromagnetici aumentano la probabilità che insorga il cancro?*, `https://www.airc.it/cancro/informazioni-tumori/corretta-informazione/vero-campi-elettromagnetici-aumentano-la-probabilita-insorgenza-del-cancro` (accessed May 8, 2022).

[9] *Rf emfs*, `https://www.icnirp.org/en/frequencies/radiofrequency/index.html` (accessed May 8, 2022).

[10] A. J. Swerdlow, M. Feychting, A. C. Green, L. Kheifets, and D. A. Savitz, "Mobile phones, brain tumors, and the interphone study: where are we now?", *Environmental health perspectives*, vol. 119, no. 11, pp. 1534–1538, 2011.

[11] D. Andreuccetti, *Introduzione alla dosimetria elettromagnetica: La valutazione delle grandezze dosimetriche nei soggetti esposti*, `https://www.webnir.eu/cem/doctechpdf/Introduzione_alla_dosimetria.pdf` (accessed May 8, 2022).

[12] *Directive 2004/40/ec of the european parliament and of the council of 29 april 2004 on the minimum health and safety requirements regarding the exposure of workers to the risks arising from physical agents (electromagnetic fields)*, European Parliament and Council of the European Union, 2004.

[13] *Directive 2013/35/EU of the European Parliament and of the Council of 26 June 2013 on the minimum health safety requirements regarding the exposure of workers to the risks arising from physical agents (electromagnetic fields)*, European Parliament and Council of the European Union, 2013.

[14] P. A. Hasgall, F. Di Gennaro, C. Baumgartner, *et al.*, "IT'IS database for thermal and electromagnetic parameters of biological tissues. Version 4.1.", Feb. 2022.

[15] L. Cataldo, "Dosimetria per campi elettrici a bassa frequenza", Thesis, Politecnico di Torino.

[16] *IEEE Standard for Safety Levels with Respect to Human Exposure to Electromagnetic Fields, 0 to 3 kHz,* Standard IEEE-C95.6, New York, NY, USA, 2002.

[17] *IEEE Standard for Safety Levels with Respect to Human Exposure to Electric, Magnetic and Electromagnetic Fields, 0 Hz to 300 GHz,* Standard IEEE-C95.1, New York, NY, USA, 2019.

[18] *Emf-portal*, `https://www.emf-portal.org/en` (accessed May 8, 2022).

[19] IEC62233, "Measurement methods for electromagnetic fields of household appliances and similar apparatus with regard to human exposure", *Int. Electrotech. Comm.*, vol. 3, 2008.

[20] *Esposizione di campi elettrici e magnetici nelle frequenze basse e intermedie*, CEI EN 62226-3-1, 2008.

[21] A. Christ, W. Kainz, E. G. Hahn, *et al.*, "The Virtual Family - development of surface-based anatomical models of two adults and two children for dosimetric simulations", *Phys. Med. Biol.*, vol. 55, no. 2, N23, 2009.

[22] M. Gosselin, E. Neufeld, H. Moser, *et al.*, "Development of a new generation of high-resolution anatomical models for medical device evaluation: the Virtual Population 3.0", *Phys. Med. Biol.*, vol. 59, pp. 5287–5303, 2014.

[23] M. J. Ackerman, "The Visible Human Project", *Proceedings of the IEEE*, no. 3, pp. 504–511,

[24] *The visible human project*, `https://www.nlm.nih.gov/research/visible/visible_human.html` (accessed May 8, 2022).

[25] T. Dawson, "Numerical evaluation of 60 MHz magnetic induction in the human body in complex occupational environments", *Phys. Med. Biol.*, vol. 44, pp. 1025–1040, 1999.

[26] S. J. Allen, E. R. Adair, K. S. Mylacraine, W. Hurt, and J. Ziriax, "Empirical and theoretical dosimetry in support of whole body resonant RF exposure (100 MHz) in human volunteers", *Bioelectromagnetics*, vol. 24, no. 7, pp. 502–509, 2003.

[27] ——, "Empirical and theoretical dosimetry in support of whole body radio frequency (RF) exposure in seated human volunteers at 220 MHz", *Bioelectromagnetics*, vol. 26, no. 6, pp. 440–447, 2003.

[28] R. P. Findlay and P. Dimbylow, "Effects of posture on FDTD calculations of specific absorption rate in a voxel model of the human body", *Phys. Med. Biol.*, vol. 50, no. 16, pp. 3825–3835, 2005.

[29] ——, "FDTD calculations of specific energy absorption rate in a seated voxel model of the human body from 10 MHz to 3 GHz", *Phys. Med. Biol.*, vol. 51, no. 9, pp. 2339–2352, 2006.

[30] T. Dawson, K. Caputa, and M. Stuchly, "Magnetic field exposures for UK live-line workers", *Phys. Med. Biol.*, vol. 47, pp. 995–1012, 2002.

[31] T. Nagaoka and S. Watanabe, "Postured voxel-based human models for electromagnetic dosimetry", *Phys. Med. Biol.*, vol. 53, no. 24, pp. 7047–7061, 2008.

[32] V. De Santis, X. L. Chen, I. Laakso, and A. Hirata, "An equivalent skin conductivity model for low-frequency magnetic field dosimetry", *Biomed. Phys. Eng. Express*, vol. 1, no. 1, 2015.

[33] Y. Diao, J. Gomez-Tames, E. A. Rashed, R. Kavet, and A. Hirata, "Spatial Averaging Schemes of In Situ Electric Field for Low-Frequency Magnetic Field Exposures", *IEEE Access*, vol. 7, pp. 184 320–184 331, 2019.

[34] E. A. Rashed, J. Gomez-Tames, and A. Hirata, "Human head skin thickness modeling for electromagnetic dosimetry", *IEEE Access*, vol. 7, pp. 46 176–46 186, 2019.

[35] M. Soldati and I. Laakso, "Computational errors of the induced electric field in voxelized and tetrahedral anatomical head models exposed to spatially uniform and localized magnetic fields", *Phys. Med. Biol.*, vol. 65, no. 1, p. 015 001, 2020.

[36] J. Gomez-Tames, I. Laakso, Y. Haba, A. Hirata, D. Poljak, and K. Yamazaki, "Computational Artifacts of the In Situ Electric Field in Anatomical Models Exposed to Low-Frequency Magnetic Field", *IEEE Trans. Electromagn. Compat.*, vol. 60, no. 3, pp. 589–597, 2018.

[37] A. Arduino, O. Bottauscio, M. Chiampi, *et al.*, "Accuracy Assessment of Numerical Dosimetry for the Evaluation of Human Exposure to Electric Vehicle Inductive Charging Systems", *IEEE Trans. Electromagn. Compat.*, vol. 62, no. 5, pp. 1939–1950, 2020.

[38] A. Hirata, Y. Takano, O. Fujiwara, T. Dovan, and R. Kavet, "An electric field induced in the retina and brain at threshold magnetic flux density causing magnetophosphenes", *Phys. Med. Biol.*, vol. 56, no. 13, pp. 4091–4101, 2011.

[39] X. L. Chen, S. Benkler, N. Chavannes, *et al.*, "Analysis of human brain exposure to low-frequency magnetic fields: A numerical assessment of spatially averaged electric fields and exposure limits.", *Bioelectromagnetics*, vol. 34, no. 5, pp. 375–384, 2013.

[40] A. Hirata, Y. Takano, Y. Kamimura, and O. Fujiwara, "Effect of the averaging volume and algorithm on the in situ electric field for uniform electric- and magnetic-field exposures.", *Phys. Med. Biol.*, vol. 55, no. 9, pp. 243–252, 2010.

[41] I. Laakso and A. Hirata, "Reducing the staircasing error in computational dosimetry of low-frequency electromagnetic fields", *Phys. Med. Biol.*, vol. 57, no. 4, pp. 25–34, 2012.

[42] E. Tonti, "The reasons for analogies between physical theories", *Applied Mathematical Modelling*, vol. 1, no. 1, pp. 37–50, 1976.

[43] P. Alotto, F. Freschi, M. Repetto, and C. Rosso, *The Cell Method for Electrical Engineering and Multiphysics Problems, an Introduction*. Berlin: Springer, 2013.

[44] E. Tonti, "Finite formulation of electromagnetic field", *IEEE Trans. Mag.*, vol. 38, no. 2, pp. 333–336, 2002.

[45] A. Bossavit, *Computational Electromagnetism*. New York: Academic, 1998.

[46] H. Whitney, *Geometric Integration Theory*. Princeton: Princeton University Press, 1957.

[47] M. Repetto and F. Trevisan, "Global formulation of 3d magnetostatics using flux and gauged potentials", *International Journal for Numerical Methods in Engineering*, vol. 60, pp. 755–772, May 2004.

[48] E. Tonti, *The Mathematical Structure of Classical and Relativistic Physics: A General Classification Diagram (Modeling and Simulation in Science, Engineering and Technology)*. Birkhäuser, 2013.

[49] F. Freschi, L. Giaccone, V. Cirimele, and A. Canova, "Numerical assessment of low-frequency dosimetry from sampled magnetic fields", *Phys. Med. Biol.*, vol. 63, no. 1, p. 015 029, 2018. [Online]. Available: `http://stacks.iop.org/0031-9155/63/i=1/a=015029`.

[50] T. Dawson, K. Caputa, and M. Stuchly, "Analytic validation of a three-dimensional scalar-potential finite-difference code for low-frequency magnetic induction", *Appl. Comput. Electrom.*, vol. 11, no. 3, pp. 72–81, 1996.

[51] X. L. Chen, A. E. Umenei, D. W. Baarman, *et al.*, "Human Exposure to Close-Range Resonant Wireless Power Transfer Systems as a Function of Design Parameters", *IEEE Trans. Electromagn. Compat.*, vol. 56, no. 5, pp. 1027–1034, 2014.

[52] T. Dawson and M. Stuchly, “High-resolution organ dosimetry for human exposure to low-frequency magnetic fields”, *IEEE Trans. Mag.*, vol. 34, no. 3, pp. 708–718, 1998.

[53] I. Laakso, S. Tsuchida, A. Hirata, and Y. Kamimura, “Evaluation of SAR in a human body model due to wireless power transmission in the 10 MHz band”, *Phys. Med. Biol.*, vol. 57, no. 15, pp. 4991–5002, 2012.

[54] I. Laakso, V. D. Santis, S. Cruciani, T. Campi, and M. Feliziani, “Modelling of induced electric fields based on incompletely known magnetic fields”, *Phys. Med. Biol.*, vol. 62, no. 16, p. 6567, 2017. [Online]. Available: `http://stacks.iop.org/0031-9155/62/i=16/a=6567`.

[55] A. Arduino, O. Bottauscio, M. Chiampi, I. Laakso, and L. Zilberti, “Computational low frequency electromagnetic dosimetry based on magnetic field measurements”, *IEEE J. Electromagn., RF, Microw. Med. Biol.*, vol. 2, no. 4, pp. 302–309, 2018. [Online]. Available: `https://ieeexplore.ieee.org/document/8456495`.

[56] A. Conchin Gubernati, F. Freschi, L. Giaccone, T. Campi, V. De Santis, and I. Laakso, “Comparison of Numerical Techniques for the Evaluation of Human Exposure From Measurement Data”, *IEEE Trans. Mag.*, vol. 55, no. 6, 2019.

[57] S. Sahoo, “Inverse vector operators”, Apr. 2008.

[58] R. Albanese and G. Rubinacci, “Finite element methods for the solution of 3d eddy current problems”, *Adv. Imag. Elect. Phys.*, vol. 102, pp. 1–86, 1997.

[59] L. Giaccone, *B-field measured*, `https://github.com/giaccone/Bfield_measured` (accessed May 8, 2022).

[60] G. Fasshauer and J. Zhang, “Preconditioning of radial basis function interpolation systems via accelerated iterated approximate moving least squares approximation”, *Progress on Meshless Method*, pp. 57–75, 2008.

[61] N. Siauve, L. Nicolas, C. Vollaire, A. Nicolas, and J. Vasconcelos, “Optimization of 3-D SAR distribution in local RF hyperthermia”, *IEEE Trans. Mag.*, vol. 40, no. 2, pp. 1264–1267, 2004.

[62] R. Scorretti, N. Burais, O. Fabregue, A. Nicolas, and L. Nicolas, “Computation of the Induced Current Density Into the Human Body Due to Relative LF Magnetic Field Generated by Realistic Devices”, *IEEE Trans. Mag.*, vol. 40, no. 2, pp. 643–646, 2004.

[63] R. Scorretti, N. Burais, L. Nicolas, and A. Nicolas, “Modeling of induced current into the human body by low-frequency magnetic field from experimental data”, *IEEE Trans. Mag.*, vol. 41, no. 5, pp. 1992–1995, 2005.

[64] R. Scorretti, R. V. Sabariego, L. Morel, C. Geuzaine, N. Burais, and L. Nicolas, “Computation of Induced Fields Into the Human Body by Dual Finite Element Formulations”, *IEEE Trans. Mag.*, vol. 48, no. 2, pp. 783–786, 2012.

[65] L. H. Hoang, R. Scorretti, N. Burais, and D. Voyer, “Numerical Dosimetry of Induced Phenomena in the Human Body by a Three-Phase Power Line”, *IEEE Trans. Mag.*, vol. 45, no. 3, pp. 1666–1669, 2009.

[66] D. A. Field, “Qualitative measures for initial meshes”, *Int. J. Numer. Methods Eng.*, vol. 47, no. 4, pp. 887–906, 2000.

[67] W. Smythe, *Static and Dynamic Electricity*. New York, N. Y.: McGraw-Hill Book Co. Inc., 1950.

[68] D. L. Collins, A. P. Zijdenbos, V. Kollokian, *et al.*, “Design and construction of a realistic digital brain phantom”, *IEEE Trans. Med. Imaging.*, vol. 17, no. 3, pp. 463–468, 1998.

[69] Q. Fang, “Mesh-based Monte Carlo method using fast ray-tracing in Plucker coordinates”, *Biomed. Opt. Express.*, vol. 1, no. 1, pp. 165–175, 2010.

[70] *Colin27 adult brain atlas fem mesh*, `http://mcx.space/wiki/index.cgi?MMC/Colin27AtlasMesh` (accessed May 8, 2022).

[71] S. N. Makarov, G. M. Noetscher, and A. Nazarian, *Low-Frequency Electromagnetic Modeling for Elecrical and Biological Systems Using MATLAB®*. New York: Wiley, 2015.

[72] *Low-frequency electromagnetic modeling*, `https://www.wiley.com/legacy/wileychi/makarov/` (accessed May 8, 2022).

[73] A. Conchin Gubernati, F. Freschi, L. Giaccone, R. Scorretti, L. Seppecher, and G. Vial, “Modeling of Exposure to Low-Frequency Electromagnetic Fields of Workers in Arbitrary Posture”, *IEEE Trans. Mag.*, vol. 56, no. 2, 2020.

[74] J. Gao, “Generation of Postured Voxel-based Human Models Used for Electromagnetic Applications”, *Ph.D. dissertation Technische Univ.*, 2012.

[75] A. Nicolet, F. Zolla, O. Agha, and S. Guenneau, “Geometrical transformations and equivalent materials in computational electromagnetism”, *Compel*, vol. 27, no. 4, pp. 806–819, 2008.

[76] F. Henrotte, B. Meys, H. Hedia, P. Dular, and W. Legros, “Finite element modelling with transformation techniques”, *IEEE Trans. Mag.*, vol. 35, no. 3, pp. 1434–1437, 1999.

[77] S. Johnson, *Coordinate transformation and invariance in electromagnetism*, `https://math.mit.edu/~stevenj/18.369/spring08/coordinate-transform.pdf` (accessed May 8, 2022).

[78] T. Nagaoka, S. Watanabe, K. Sakurai, *et al.*, “Development of realistic high-resolution whole-body voxel models of Japanese adult males and females of average height and weight, and application of models to radio-frequency electromagnetic-field dosimetry”, *Phys. Med. Biol.*, vol. 49, no. 1, 2003.

[79] P.-J. Dimbylow, “Development of the female voxel phantom, NAOMI, and its application to calculations of induced current densities and electric fields from applied low frequency magnetic and electric fields”, *Phys. Med. Biol.*, vol. 50, pp. 1047–1070, 2005.

[80] A. Mathai and H. Haubold, “Jacobians of matrix transformations.”, in *Special Functions for Applied Scientists*. Cambridge; New York: Springer, New York, NY, 2008, pp. 409–428.

This Ph.D. thesis has been typeset by means of the TeX-system facilities. The typesetting engine was pdfLaTeX. The document class was `toptesi`, by Claudio Beccari, with option `tipotesi =scudo`. This class is available in every up-to-date and complete TeX-system installation.